



**Politecnico  
di Torino**

**Politecnico di Torino**

Laurea Magistrale in Ingegneria Biomedica

A. A. 2021/2022

Sessione di Laurea marzo 2022

# Study of spinal cord poroelastic behavior under Chiari Malformation conditions:

A computational fluid dynamics study.

Promoter:

Prof. Umberto Morbiducci  
Prof. Patrick Segers (Ugent)

Candidate:

Pietro Matcovich

Supervisors:

Diego Gallo  
Sarah Vandembulcke (Ugent)  
Matthias Van Impe (Ugent)

A project in collaboration with Ghent University





## Declaration of Authorship

I, Pietro Matcovich, declare that this thesis titled “Study of spinal cord poroelastic behavior under Chiari Malformation conditions: A computational fluid dynamics study.”, and the work presented in it are my own. I confirm that:

- This work was done wholly or mainly while in candidature for a Master of Science degree at this University.
- Where any part of this thesis has previously been submitted for a degree or any other qualification at this University or any other institution, this has been clearly stated.
- Where I have consulted the published work of others, this is always clearly attributed.
- Where I have quoted from the work of others, the source is always given. With the exception of such quotations, this thesis is entirely my own work.
- I have acknowledged all main sources of help.
- Where the thesis is based on work done by myself jointly with others, I have made clear exactly what was done by others and what I have contributed myself.

The author gives permission to make this master dissertation available for consultation and to copy parts of this master dissertation for personal use. In all cases of other use, the copyright terms have to be respected, in particular with regard to the obligation to state explicitly the source when quoting results from this master dissertation.

Signed:   
\_\_\_\_\_

Date: 22/8/2021  
\_\_\_\_\_



## Acknowledgments

I want to thank my promoters Prof. Patrick Segers and Prof. Umberto Morbiducci for making this thesis possible. Many thanks to my supervisors Sarah Vandebulcke and Matthias Van Impe, whose help and guidance throughout the whole working period have been fundamental. I also would like to thank all the people in the BioMMeda group for their help in all the classes I've attended during my period at Ugent.

Thanks to my girlfriend Mariachiara, whose support was lifesaving even from thousands of kilometers of distance. To my father Corrado and my mother Cecilia for giving me the opportunity to study and experience this ERASMUS period in Gent. Thanks to my brother Lorenzo and my sister Benedetta: thank you! Thanks to all my family who always supported me throughout these years.

Thanks to all my friends, especially Luca and Francesco, for every funny and beautiful moment lived together. Thanks to all my fellow students, both at PoliTo, VUB, and Ugent for making these years so joyful and enjoyable even during covid times.

Finally, a big thanks to all the people I've forgotten to mention before I've been lucky to meet you all none excluded, and I'll never change my mind.



## Abstract

Chiari malformation (CM) is a rare neurological condition characterized by the herniation of cerebellar tonsils through the foramen magnum. Almost 40-75% of patients with CM develop a syrinx, a fluid-filled cavity inside the spinal cord. The characteristics of the pathology and clinical experience linked the development and resolution of the syrinx to the disrupted fluid dynamics. However, this mechanism has not been fully understood yet.

Poroelasticity is a powerful instrument to model porous tissues like the spinal cord. However, only a few studies using this physic to study the CM relate syringomyelia can be found in the literature. Therefore, the objective of this thesis was to investigate the poroelastic behavior of the spinal cord under CM conditions. Mainly with a focus on the fluid dynamics in the SAS and on the spinal cord response.

The first study focused on poroelasticity. It highlighted the effect of geometry, permeability, Young's modulus, and Poisson's ratio on the material swelling. It indicated the time needed to establish a flow through the material, allowing the optimization of numerical settings for the computational modeling.

Based on the results of the first study, an idealized 2D axisymmetric model of the spinal cord and spinal subarachnoid space was built to assess the influence of different parameters (inlet and permeability) on spinal cord behavior. Various physiological situations were simulated by applying different inlet conditions. The results highlighted the influence of the inlet pressure wave frequency (coming from the skull) on the poroelastic material's response. Higher frequencies, related to higher cardiac frequencies, coughing, sneezing or Valsalva's maneuvers, showed to increase the response's magnitude. Changes in material permeability presented a nonlinear relation between this property and the volumes oscillations of the syrinx. However, the mechanism behind this relationship is not yet clear and further investigations are needed.

In conclusion, the obtained results can give an overview of the poroelastic behavior of the spinal cord. The findings of the influence of material properties can be useful for the research prosecution and the presented model can be improved to investigate other elements.

Keywords: Chiari Malformation, Syringomyelia, Poroelasticity, Spinal cord.



# Study of spinal cord poroelastic behavior under Chiari Malformation conditions:

A computational fluid dynamics study.

Matcovich Pietro

Promoters: Patrick Segers, Umberto Morbiducci

Supervisors: Sarah Vandenbulcke, Matthias Van Impe, Diego Gallo

**Abstract:** The origin of syringomyelia in association with Chiari 1 malformation (CM) is still unclear. This thesis aims to study the poroelastic behavior of the spinal cord in the diseased condition. A first simple model aimed to study the poroelasticity itself. It highlighted the relationship between various material properties and the material swelling. A second model of the spinal cord and spinal Subarachnoid space (SAS) assessed the influence of permeability and inlet conditions on the spinal cord response.

**Keywords:** Chiari Malformation, Syringomyelia, Poroelasticity, Spinal cord.

## I. Background

Chiari malformation is a rare neurological condition characterized by the herniation of cerebellar tonsils the foramen magnum. The main effect is the disruption of the flow of cerebrospinal fluid from the skull to the spinal subarachnoid space. A big part of patients with CMI [1] (40-75%) develops a syrinx. A fluid filled cavity inside the spinal cord (syrinx). Given the nature of the condition the disruption of the cerebrospinal fluid (CSF) flow and the fluid dynamics in general may have an important role in the syrinx development. However, a complete understanding of this mechanism has not been reached yet.

Several different approaches to the problem can be found in literature, including the experimental approach of Martin et al. [2] and computational models (Bertram et al. [3]). However, few of them directly considers the CM related syrinx and even less focus on the poroelasticity itself used for biomedical applications.

## II. Objectives

The objective of this study was to investigate the poroelastic behavior of the spinal cord under Chiari Malformation conditions. Specifically, the focus was on the response of the spinal cord to the fluid dynamics in the spinal SAS, which is impacted by the flow through the foramen magnum. To do so two consecutive studies were set up. The first one, focusing directly on the poroelasticity, was meant to evaluate the influence of different material properties on the material behavior. The second study focused on the syrinx and

spinal cord volume changes and their relationship with geometry, inlet conditions and material permeability.

## III. Poroelastic material study

### A. Materials and methods

Poroelastic models are crucial because they allow the investigation of fluid flow and its migration between fluid and solid materials, which is a central element in the development and evolution of the syrinx. In this work a computational model built in COMSOL® was used. The same physical approach used by Silvera [4] was applied. The theory of poroelasticity (particularly the Brinkman's equations) was used to describe the behavior of fluids inside the spinal cord and pia mater while the flow in the SAS and syrinx was modeled according to the Navier-Stokes's equations.

The influence of different material parameters was investigated within a simple 2D model. The geometry was composed of three rectangles with the same dimensions (1 cm x 5 cm) posed one on top of the other, as depicted in Image 1.

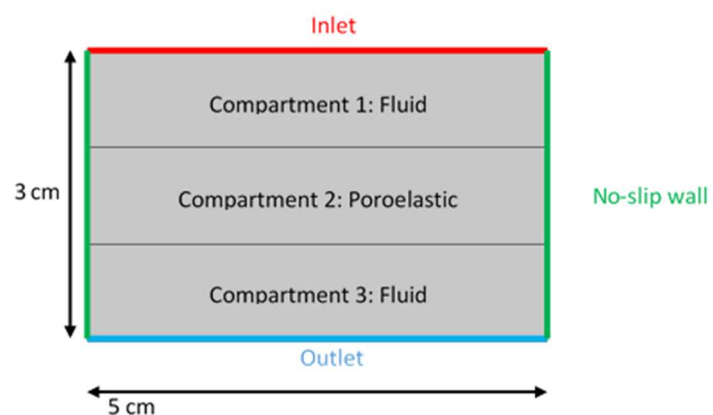


Image 1: Scheme of the model

## Extended Abstract

The fluid had the same properties of water at room temperature (20°C). While, the poroelastic material properties were based on the ones applied by Bertram et al. [3] and modified in the range of values presented in Table 1. Geometrical properties were also studied by varying the height-width ratio of all the domains.

Table 1: range of values investigated for each poroelastic material property.

Parameter	Range
Density [kg/m <sup>3</sup> ]	1000
Young's modulus [MPa]	0.004 – 1.25
Poisson's ratio	0.2 – 0.4
Dynamic viscosity [Pa s]	7E-4
Permeability [m <sup>2</sup> ]	8E-15 – 1E-13
Porosity	0.3

The effect of changes in material properties was investigated using steady simulations. An arbitrary inlet velocity condition of 6e-8 m/s and an outlet condition of 0 Pa were set.

Thereafter, time-dependent simulations were run to check the consistency of the results. The inlet condition was therefore modified using a ramp function (Image 2).

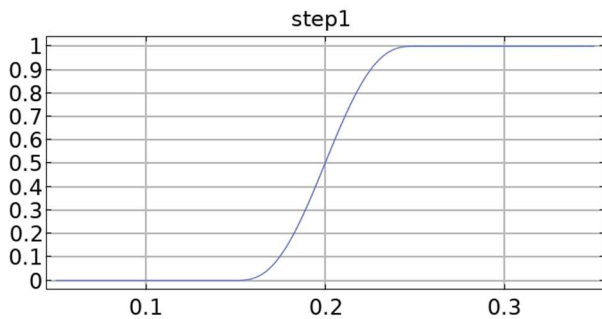


Image 2: Ramp function used to modify the inlet for time dependent simulations.

The influences of the different parameters were evaluated based on two criteria: the pressure difference between the fluid compartments 1 and 2 and the percentual swelling. The percentual swelling was calculated from the absolute area increase in Microsoft Excel® using the following formula:

$$S_{\%} = \frac{A_f - A_i}{A_i}$$

Where  $S_{\%}$  is the percentual swelling,  $A_i$  is the initial area, and  $A_f$  is the final area.

## B. Results

Permeability was the only parameter that influenced both the swelling of the material and the pressure difference between the two fluid compartments. These two both pressure and swelling were found to decrease with the increase in permeability as depicted in Image 3.

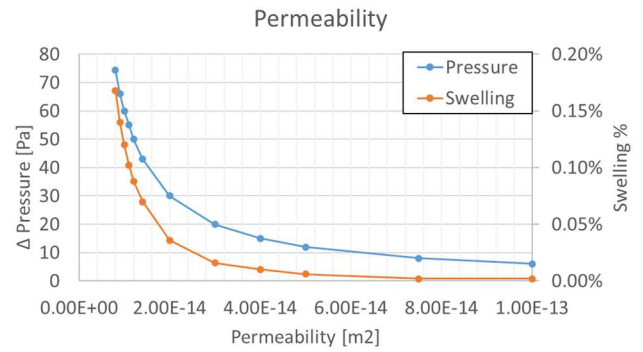


Image 3: Impact of different permeability values on percentual swelling and pressure difference

In contrast, the Young's modulus only had an influence on the swelling. The relationship between these two elements was exponentially decreasing, reaching values lower than 0.001% already at 0.0625 MPa, as depicted in Image 4.

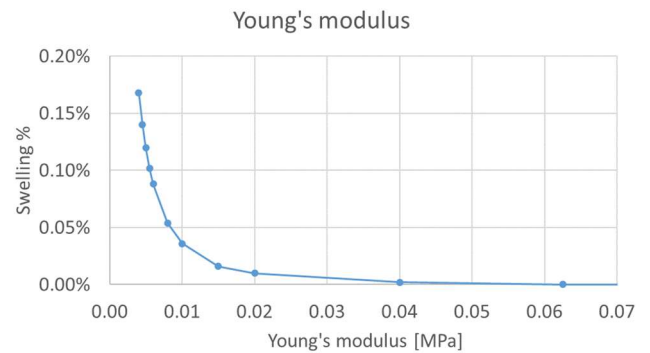


Image 4: Young's modulus relationship with percentual swelling

Furthermore, the geometry of the domain was observed to influence both the pressure difference between the fluid compartments and the percentual swelling: an increasing linear relation was found between the height-width ratio and the pressure difference, whereby the slope depends on the chosen width. Meanwhile, the percentual swelling decreases exponentially with an increasing height-width ratio. When this ratio value exceeds 0.3, the poroelastic material was compressed (a negative swelling was recorded).

The time-dependent simulations highlighted the presence of a transition period. During this time a

## Extended Abstract

proper fluid flux through the poroelastic medium was not present, only a recirculatory movement can be observed in the fluid domains. The duration of this transient showed to depend on the permeability value of the poroelastic material and last around 5 minutes for a value of  $1e-13 \text{ m}^2$ .

### C. Discussion

The results indicate that an increase in the material stiffness and rigidity (Young's modulus and Poisson's ratio) is associated with a decrease in the swelling. This can be related to the fact that these properties affect the way the material reacts to the external forces and increasing their value makes the material less likely to deform. The effect of the height-width ratio also falls under this mechanism. However, increasing the thickness (and therefore the distance that the fluid must travel through the poroelastic material) also cause an increase in the pressure difference is needed to force the fluid through the domain. The permeability impacts the degree of swelling because it either increases or decreases the resistance to the fluid passage by changing the ability of the material to hold part of the fluid. It also influences the pressure difference because having a higher resistance means needing a higher pressure drop to have the same flow. Therefore, a material with a higher permeability is less capable to hold back fluid but, at the same time, a lower force is needed to push the fluid through it.

Time-dependent simulations showed that some time is needed for the fluid flow to be established across the poroelastic material. The duration of this transient period depends on the permeability value and can reach values up to several minutes. The duration of this transient suggests that in the next model where the inlet condition will be sinusoidal, the continuous change of the pressure condition may not allow the establishment of a proper fluid flow across the poroelastic spinal cord. Some relevant computational issues that will need attention during the building phase of the next model were also highlighted during this first study.

### Spinal cord model

The findings from the previous study were used to build a poroelastic model of the spinal cord.

#### A. Materials and methods

Based on the geometry of Bertram et al. [3] a baseline 2D axisymmetric model was built. It included the spinal cord, the pia, the SAS, and the dura (Image 5). Inside

the spinal cord, a syringe was placed, with the same dimensions as the one used by Kumbhar [5], having a total length of 70mm, and an initial volume of 1.149ml. The Foramen Magnum is the only opening of the model, acting as both inlet and outlet. The cord, the pia, and the dura were constrained at the top and at the bottom edges of the geometry. The model is allowed to expand only in the external direction (the dura can move towards the outside). Triangular mesh elements were used, however, considering the experience gathered with the first model a boundary layer was always included at the interface between the fluid and the poroelastic materials. After a mesh sensitivity study a mesh having a total of 222733 elements was chosen. Three different setups were prepared to investigate different aspects. Based on this geometry 3 setups were prepared.

l) - In this setup five different values of permeability were given to the poroelastic materials, ranging from  $e-11$  to  $e-15$  as depicted in Table 2. The same inlet condition applied by Bertram et al. [3] was used. It consists of a sinusoidal pressure wave with an amplitude of 1000Pa and a frequency of 2.5Hz and an average value of 500 Pa.

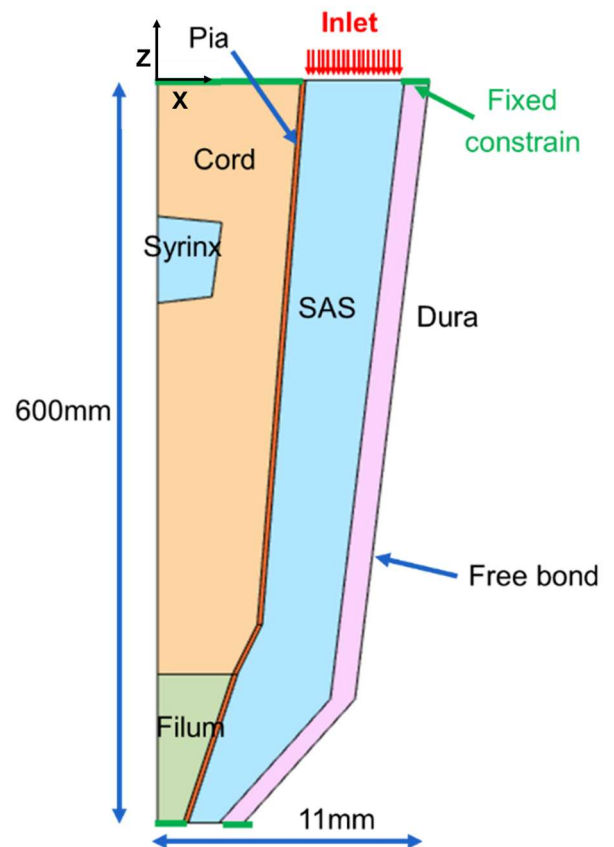


Image 5: Schematic of the spinal cord model.

Table 2: Material properties used in setup 1.

Material	Density [kg/m <sup>3</sup> ]	Young modulus [MPa]	Poisson ratio	Dynamic viscosity [Pa s]	Permeability [m <sup>2</sup> ]	Porosity
Cord	1000	0.005	0.35	7e-4	e-11 / e-15	0.3
Filum	1000	0.0625	0.35	7e-4	e-11 / e-15	0.3
Pia	1000	1.25	0.35	7e-4	e-11 / e-15	0.3
Dura	1000	1.25	0.49	NA	NA	NA
CSF	1000	NA	NA	0.001	NA	NA

II) - The second setup was used to evaluate the effect of different inlet conditions corresponding to different physiological behaviors. The same geometry of setup 1 was used but the permeability value was fixed at 1e-13 m<sup>2</sup>. Three different inlet conditions were used. The first condition (A) was a pressure inlet shaped with a sinusoidal wave of 1000Pa amplitude, 500Pa average, and frequency of 2.5Hz. The second inlet condition (B) was still a pressure inlet with 1000Pa amplitude and 500Pa average, but the frequency was dropped to 1.25Hz. The third inlet condition (C) was a mass flow inlet condition, defined to resemble the one used by Martin et al. [2]. The wave had an amplitude of 5ml/s with a 0ml/s average and a frequency of 1.25Hz.

III) - In the last setup the already described geometry was modified to resemble the one used By Martin et al. [4]. The syringe was extended, and to obtain a geometry representing a patient with the CM a block of 40mm length was introduced based on the one implemented by Martin et al. [2]

B. Results

I) - The first setup highlighted that the biggest part of the fluid incoming in the model is taken from the SAS. his quantity depends mainly on the chosen inlet function. The spinal cord volumes oscillations generally reflect the decrease in the permeability of the tissues. However, this relation is not linear. The difference in the response of the two models with the highest values (1e-10 and 1e-11 m<sup>2</sup>) is significantly smaller than the one between the two with mild values (1e-12 and 1e-14 m<sup>2</sup>). A lower value of permeability also induces a higher delay in the solid response (Image 6).

The syringe shows a particular behavior. The volumes changes are not dropping along with the decrease in permeability. When the permeability is lower than 1e-13 the syringe volume change is constant (Image 7). This suggests that with such low permeability values the effect of fluid entering or exiting the syringe is negligible. Therefore, the volume changes may not be related to fluid movements. Rather, it may be caused by the

effect of movement of the surrounding poroelastic solids.

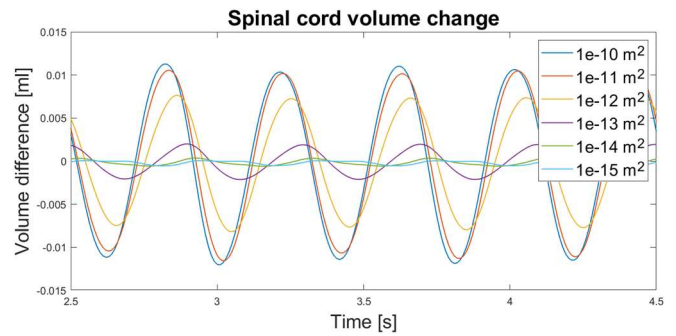


Image 7: Spinal cord volume change for different permeability values

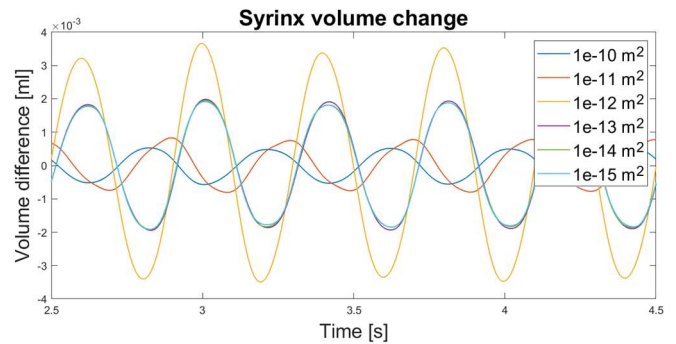


Image 8: Syrinx volume change for different permeability values.

The pressure difference between the syrinx and the corresponding SAS. Is interesting to notice that it is not constant along all the syrinx length. As can be observed in Image 8, while in part of the syrinx the pressure difference with the SAS is positive in the other part it is negative. This may induce a sort of recirculatory movement.

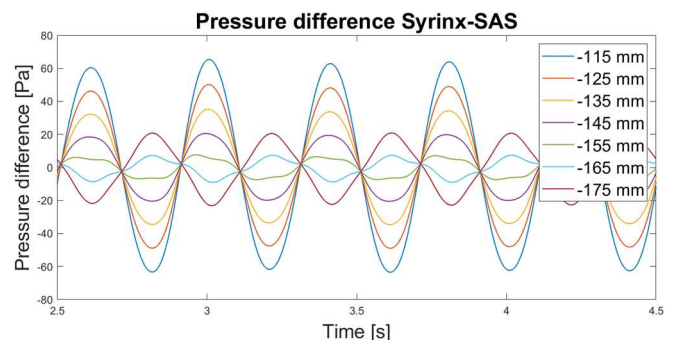


Image 6: Pressure difference syrinx-SAS at different z coordinates in mm. Notice that the syrinx extends from z=-110 (top) to z=-180mm (bottom). Model permeability 1e-13 m<sup>2</sup>.

## Extended Abstract

II) - The results of setup 2 showed the effect of inlet wave frequency on the poroelastic solids response, with a lower frequency corresponding to a lower response, as depicted in Image 9.

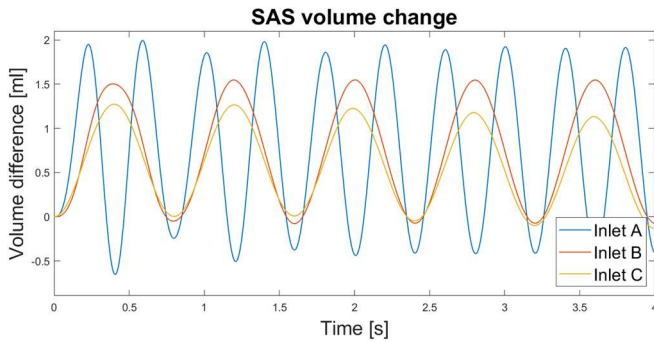


Image 9: SAS volume change for different inlet conditions.

III) - The two models of setup III presented a difference in the spinal cord volume oscillations. The model without the malformation presents a smaller amplitude of the response (Image 10). While the other one not only present a bigger amplitude but also a different average value highlighting a general reduction in the volume of the spinal cord.

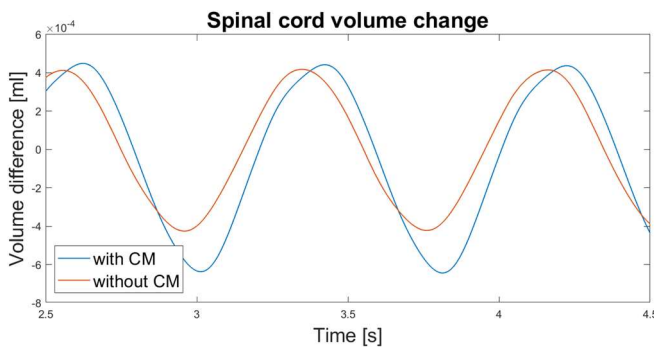


Image 10: Spinal cord volume changes in the models of setup III

This difference is probably due to the restriction of the SAS caused by the malformation. When the fluid is flowing inside the SAS, the section of the spinal cord near the narrowing is compressed by the fluid causing the increase in the negative peak of the wave in Image 10. These deformations are clearly not present in the model without the malformation.

The flow patterns inside the spinal cord and syringe are consistent between all the models. A sort of recirculatory fluid movement like the one described by Bertram et al. [3] is present. However, this cannot be clearly observed due to the low fluid velocity inside the spinal cord. The low velocity coupled with the cyclic changes in the flow pattern highlight the fact that there is not a proper fluid flow between the syringe and the SAS. Rather, at every cycle some fluid is exchanged between the SAS and the Spinal cord and vice-versa.

From the simulations these movements look to be balanced and seems not to cause any change in the average syringe volume. However, some imbalances may be present that are too small to be captured by the presented models.

## C. Discussion

Setup I show that the fluid mass forced in and out depends only on the applied boundary condition regardless of the properties of the poroelastic materials. The Spinal cord volume change decrease with smaller permeability values. This can be related to the fact that a smaller permeability decreases the amount of fluid entering the material. This is not the case for the syringe volume, in which the oscillations show a nonlinear relation with the permeability. For values smaller than  $1e-13 \text{ m}^2$  the volume changes became constant. This may lead to suppose that at this low permeabilities the influence of fluid moving across the spinal cord is negligible and the volume changes will mainly be due to the deformations imposed by the movement of the surrounding solid tissues. For permeability values greater than  $1e-13 \text{ m}^2$  the amplitude of volumes oscillations appears to increase for  $1e-12 \text{ m}^2$  and then decrease for  $1e-11$  and  $1e-10 \text{ m}^2$ . A clear reason for this behavior has not been found yet and further investigations are needed to clarify this point.

The models in setup II show that the frequency of the inlet wave has a relevant influence on the amount of fluid forced in and out of the model. Higher frequencies, corresponding to the effects of Valsalva's maneuvers or coughing [3], force a higher amount of mass inside the studied domain.

The last setup (III) showed a clear difference in the spinal cord volume oscillations. In the model with CM it is possible to observe an increase in the shrinkage and swelling of the top section of the spinal cord itself. Probably induced by the presence of the CM. This phenomenon leads also to a reduction in the average volume of the spinal cord when the CM is present. To my knowledge, this effect has never been previously highlighted in literature, however, it is probably related to the simplifications considered in this specific study.

In all the models is thought to observe a proper flow between the SAS and the syringe. This is the result of the combined effect of time needed for the flow to establish and the continuous change in pressure conditions. Similarly to Bertram et al. [3], only very

## Extended Abstract

limited fluid movements can be observed between these two compartments, with small amounts of mass simultaneously exchanged between spinal cord and syrinx. Small imbalances in this mass movements may play a role in the syrinx evolution. However, in the clinical cases the reduction or growth of a syrinx happens in months. Therefore, probably the time scale of the models used in this study is too small to capture this effect as stated by Bertram et al. [3] in a similar study.

Several simplifications influence the obtained results. The used axisymmetric geometry is highly idealized, and all the structures are modeled in isolation from the brain and the skull. The design adopted to model the CM cannot account for the movement of the herniated tonsils or the complete obstruction of the fluid passage. The structures present in the SAS (trabeculae, ligaments, and nerve roots) are completely neglected. The outer diameter of the spinal cord was kept constant also when introducing a syrinx. All the materials are modeled as isotropic for all their properties. Although this is not the case [6]. Also, all the poroelastic materials are considered to have the same permeability. Finally, the periodic CSF impulsion from the cranial subarachnoid space is simplified with a sinusoidal wave with nonzero average.

## Conclusions

In conclusion this work gave to the reader a deeper look into the poroelasticity both in general and applied to CM-related syringomyelia.

The presented relations between permeability, pressure and swelling can be used to estimate the behavior of more complex poroelastic models. The evaluations about Young's modulus, Poisson's ratio, and geometry highlighted the role of these properties in the poroelastic material response. These findings can help to better understand the poroelastic behavior of the spinal cord.

The study conducted about the CM gives an overview of the spinal cord behavior in different situations. And can be improved to reflect more accurately the clinical conditions and explain some unexpected results.

Further steps can be the improvement of materials modelling. This may be done by considering the materials anisotropy and different permeabilities for each tissue. These improvements may help to better model the behavior of the spinal cord and surrounding structures. In vivo recorded data can be used to create

and implement more accurate CSF inlet condition. The geometry can be extended to also include the cerebral tonsils allowing the modeling of their movements. Finally, clinical images can be used to build a 3D patient specific geometry which can help to capture phenomena which cannot be observed in the 2D geometry.

## References

1. A. A. Fernández *et al.*, "Malformations of the craniocervical junction (chiari type i and syringomyelia: Classification, diagnosis and treatment)," *BMC Musculoskeletal Disorders*, vol. 10, no. SUPPL. 1. 2009. doi: 10.1186/1471-2474-10-S1-S1.
2. B. A. Martin, R. Labuda, T. J. Royston, J. N. Oshinski, B. Iskandar, and F. Loth, "Spinal subarachnoid space pressure measurements in an in vitro spinal stenosis model: Implications on syringomyelia theories," *Journal of Biomechanical Engineering*, vol. 132, no. 11, 2010, doi: 10.1115/1.4000089.
3. C. D. Bertram and M. Heil, "A Poroelastic Fluid/Structure-Interaction Model of Cerebrospinal Fluid Dynamics in the Cord with Syringomyelia and Adjacent Subarachnoid-Space Stenosis," *Journal of Biomechanical Engineering*, vol. 139, no. 1, 2017, doi: 10.1115/1.4034657.
4. C. A. Silvera Delgado, "Modelling the lymphatic system: Computational model of lymphatic capillaries-interstitium interaction in normal physiological and pathological conditions.," Torino, 2017.
5. Asawari Pratiksha Kumbhar, "A Computational Biomechanics study of the Spinal Cord in Patients with Chiari Malformation and Syringomyelia," Ghent, 2020.
6. C. Rossi *et al.*, "Water diffusion anisotropy in white and gray matter of the human spinal cord," *Journal of Magnetic Resonance Imaging*, vol. 27, no. 3, 2008, doi: 10.1002/jmri.21252.



## Summary

<b>1</b>	<b>Central Nervous system anatomy.....</b>	<b>1</b>
1.1	The brain.....	1
1.1.1	Cerebrum.....	2
1.1.2	Cerebellum .....	3
1.1.3	Brain stem .....	4
1.2	The spinal cord.....	4
1.3	Interstitial fluid .....	7
1.4	CSF pathways.....	7
<b>2</b>	<b>Chiari Malformation.....</b>	<b>10</b>
2.1	Pathophysiology .....	10
2.2	Treatment .....	11
<b>3</b>	<b>Syringomyelia .....</b>	<b>13</b>
3.1	Pathophysiology .....	13
3.2	Treatment.....	14
3.3	Theories about syrinx formation .....	15
<b>4</b>	<b>State of the art.....</b>	<b>18</b>
4.1	Introduction to experimental and in vivo techniques.....	18
4.2	Numerical methods .....	20
4.2.1	CFD models.....	20
4.2.2	FSI models .....	22
4.2.3	Poroelastic models .....	22
<b>5</b>	<b>Objectives .....</b>	<b>26</b>

<b>6</b>	<b>Study of Poroelastic material .....</b>	<b>27</b>
6.1	Materials and methods .....	27
6.1.1	Poroelasticity theory .....	27
6.1.2	Geometry and boundary conditions .....	32
6.2	Results.....	34
6.2.1	Steady simulations .....	35
6.2.2	Time-dependent simulations .....	38
6.3	Discussion .....	41
<b>7</b>	<b>Spinal cord models .....</b>	<b>43</b>
7.1	Materials and method .....	43
7.1.1	Geometry and boundary conditions .....	43
7.1.2	Mesh sensitivity study.....	47
7.2	Results.....	51
7.2.1	Setup 1.....	51
7.2.2	Setup 2.....	54
7.2.3	Setup 3.....	56
7.3	Discussion .....	59
<b>8</b>	<b>Conclusions .....</b>	<b>61</b>
	<b>References .....</b>	<b>63</b>

## List of figures

Figure 1: Overview of the CNS [1] .....	1
Figure 2: The components of the meninges [1] .....	2
Figure 3: Schematic of a neuron [1] with arrows showing signal direction.....	3
Figure 4: Cerebellum and brain stem sagittal section drawing [5] .....	4
Figure 5: Anatomy of the spinal cord [6] .....	5
Figure 6: Image showing a) Spinal cord sections at different levels [2]. b) Spinal cord overall shape and spinal cord fitting into the spine [1]. .....	6
Figure 7: Exchange of CSF and ISF along perivascular spaces [6] .....	7
Figure 8: Image of CSF pathways [8] .....	8
Figure 9: Sagittal T1 image of a patient showing Chiari Malformation type 1, with a herniation of approximately 7mm [13].....	10
Figure 10: Schematic of PFD with duraplasty [24] .....	12
Figure 11: MRI of a patient with CMI related syringomyelia [22].....	13
Figure 12: Illustration of main steps of syrinx-SAS shunting procedure. 1-View of pinal cord after dura opening. 2-The shunt catheter is inserted into the SAS. 3-The syrinx cavity is opened and one end of the catheter is inserted into the cavity. 4-The shunt catheter is sutured to the arachnoid, to avoid dislocation. [30] .....	15
Figure 13: Comparison of CSF and cerebellar tonsils movement through the cardiac cycle [32] .....	16
Figure 14: Pressure recordings in [32]. .....	18
Figure 15: Picture of the model used by Martin et al. [38], from ref. [39].....	19
Figure 16: Contours of general Reynold's numbers for a vertical (a) and horizontal plane (b) [40] .....	20
Figure 17: Different geometries used in Clarke et.al [42].....	21
Figure 18: Streamline plot for healthy case, with fine structures (left) and without (right) [43] .....	22
Figure 19: Picture of different geometries used [44] The color legends indicate the numbering of the boundaries; 4- central canal, 6- gray matter, 7- geometry sidewall, 9-white matter. ....	23
Figure 20: Sketch of the geometry of the model where $L/D=30$ and $D=20\text{mm}$ [51] .....	24
Figure 21: a) the fluid movement between SAS and syrinx. b) the average changes in syrinx volume over cycles for syrinx aligned with stenosis (red), positioned cranially to the stenosis (gold), and caudally to the stenosis (black) [48] .....	25
Figure 22: Stresses in a cubic solid element in a 3D Cartesian system. From Silvera [55] .....	29
Figure 23: Geometry of the model.....	32
Figure 24: Mesh used in the poroelastic material study.....	32
Figure 25: schematic of the applied boundary conditions. ....	34
Figure 26: Step function used to ramp up the inlet in time-dependent simulations. ....	34
Figure 27: Pressure field in model with baseline material properties.....	35
Figure 28: Velocity field and streamlines in model with baseline material properties.....	35

Figure 29: Impact of different permeability values on percentual swelling and pressure difference between the fluid compartments.....	36
Figure 30: Plot of Young's modulus effect on percentual swelling.....	37
Figure 31: Plot of Poisson's ratio effect on percentual swelling.....	37
Figure 32: Plot of height-width ratio effect on percentual swelling.....	38
Figure 33: Plot of height-width ratio effect on pressure difference.....	38
Figure 34: Pressure field in time-dependent simulation with baseline material properties...	39
Figure 35: Final mesh used for time dependent simulations. ....	39
Figure 36: Pressure field in time-dependent simulation with baseline material properties and new mesh. ....	40
Figure 37: Area of poroelastic medium over time. ....	40
Figure 38: Velocity field and streamlines in time-dependent model with baseline material properties at the end of the transient. ....	41
Figure 39: Scheme of Geometry 1. Please notice the x axis is scaled by a factor of 20. ....	44
Figure 40: Pressure inlet used in setup 1. ....	45
Figure 41: Pressure inlet A used in setup 2. ....	45
Figure 42: Pressure inlet (B) used in setup 2.....	46
Figure 43: Mass flow inlet (C) used in setup 2. ....	46
Figure 44: Scheme of the geometries used in setup 3, without CM (left) and with CM (right). ....	47
Figure 45: Section from mesh n1 highlighting the boundary layers.....	47
Figure 46: Scheme of the geometry with the position of pressure evaluation points (left). Plot of evaluation points in time over inlet profile (right). ....	48
Figure 47: Pressure percentual variation at t=0.2.....	49
Figure 48: Pressure percentual variation at t=0.3.....	49
Figure 49: Pressure percentual variation at t=0.4.....	49
Figure 50: Volumes percentual variation at t=0.2. ....	50
Figure 51: Pressure percentual variation at t=0.3.....	50
Figure 52: Pressure percentual variation at t=0.4.....	50
Figure 53: Solids deformation during inflow phase (top) and outflow phase (bottom). Deformation enhanced by 50 times. ....	51
Figure 54: Overall volume changes in the last 4 cycles for models of setup 1 for different permeability values. ....	52
Figure 55: Spinal cord volume changes in the last 4 cycles for models of setup 1 for different permeability values. ....	52
Figure 56: Syrinx volume changes in the last 4 cycles for models of setup 1 for different permeability values. ....	53
Figure 57: Syrinx-SAS pressure difference at different z coordinates (legend). The coordinates are in mm and the syrinx extends from -110 (top) to -180 mm (bottom). ....	53
Figure 58: Streamlines comparison between model with permeability $1e-13m^2$ (left) and $1e-10m^2$ (right), during inflow phase.....	54

Figure 59: SAS volume changes for models of setup 2. A) pressure inlet amplitude 500Pa frequency 2.5 Hz. B) pressure inlet amplitude 500Pa frequency 1.25 Hz. C mass flow rate inlet amplitude 5ml/s frequency 1.25 Hz ..... 55

Figure 60: Syrinx volume changes in the last 1.6s (2 or 4 cycles) for models of setup 2..... 55

Figure 61: Pressure in SAS at z=-145mm (syrinx location) for models of setup 2. .... 56

Figure 62: Overall volume changes for models of setup 3 ..... 56

Figure 63: Syrinx volume changes in the last 4 cycles for models of setup 3..... 57

Figure 64: Spinal cord volume changes in the last 4 cycles for models of setup 3..... 57

Figure 65: Solids deformation during inflow phase (top) and outflow phase (bottom). Setup 3 model with CM. Deformation enhanced by 50 times..... 58

Figure 66: Streamlines comparison between models of setup 3 (model with CM on the right, model without CM on the left) during inflow phase. .... 58



## List of tables

Table 1: Different types of Syringomyelia.....	13
Table 2: Materials properties used by Bertram et.al [48], [51]. .....	24
Table 3: Baseline material properties. ....	33
Table 4: Range of values considered in the study for each parameter .....	33
Table 5: Material properties used in setup 1, derived from Bertram et al.[48]......	44
Table 6: Material properties used in setup 2, derived from Bertram et al. [48] .....	45
Table 7: Different mesh considered in mesh sensitivity study. ....	48
Table 8: Table of mass flow rate peak values recorded at syrinx border. ....	53



## List of abbreviations

CFD	.....	Computational Fluid Dynamics
CM	.....	Chiari Malformation
CMI	.....	Chiari Malformation type 1
CNS	.....	Central Nervous System
CSF	.....	Cerebrospinal fluid
FSI	.....	Fluid Structure Interaction
ISF	.....	Interstitial fluid
MR	.....	Magnetic Resonance
MRI	.....	Magnetic Resonance Imaging
PC-MRI	.....	Phase contrast Magnetic Resonance Imaging
PNS	.....	Peripheral Nervous System
PFD	.....	Posterior Fossa Decompression
PFDD	.....	Posterior Fossa Decompression with Duraplasty
SAS	.....	Subarachnoid space



## List of symbols

$\rho$	Density	Kg/m <sup>3</sup>
$\vec{v}$	Velocity	m/s
$\vec{P}$	Pressure	Pa
$\mu$	Viscosity	Pa s
$\vec{F}$	Volume forces	N
$\vec{v}_d$	Fluid velocity inside porous medium	m/s
$k$	Permeability	m <sup>2</sup>
$Q_m$	Mass source	kg/(m <sup>3</sup> s)
$\epsilon_p$	Porosity	
$e_i$	Normal component of strain field	
$\tau_{ij}$	Tangential component of strain field	
$\sigma_i$	Component of normal stress field	Pa
$\gamma_{ij}$	Component of shear stress field	Pa
$H$	Biot's constant. Measure the compressibility of the porous medium for a change in fluid pressure	Pa
$Q$	Biot's second constant (amount of water entering a porous block while the volume of the block is constant).	Pa
$E$	Young's modulus	Pa
$G$	Shear modulus	Pa
$\nu$	Poisson's ratio	
$\vec{\epsilon}$	Strain Field	
$u$	x component of the displacement	m
$v$	y component of the displacement	m
$w$	z component of the displacement	m
$\alpha$	Biot's coefficient	
$\Theta$	Increment of water content	



## 1 Central Nervous system anatomy

The following chapter is meant to give a general overview of neuroanatomy, providing the reader the basic anatomical notions to navigate through the exposed work and literature.

Anatomically the nervous system can be divided into two parts: the central nervous system (CNS) consisting of the brain and the spinal cord, and the peripheral nervous system (PNS) which has the role to connect the CNS with the rest of the body (muscles, sensory organs...) [1].

The CNS can be anatomically subdivided into different parts: the spinal cord located in the vertebral canal and the brain located in the skull (Figure 1).

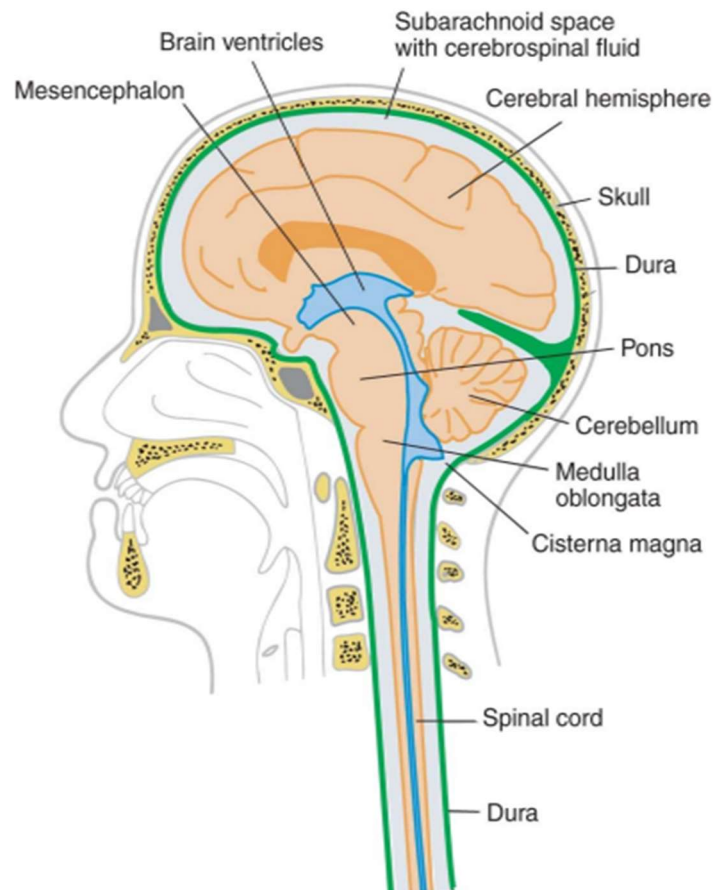


Figure 1: Overview of the CNS [1]

### 1.1 The brain

The brain is located inside the skull, which provides protection against external forces. In addition to this bony protection, the brain, as well as the spinal cord, is wrapped into three layers of tissue named “meninges” [1]. The outermost membrane is the dura mater (or simply dura), which is a thick and strong layer of connective tissue that covers the inside of the skull.

The second layer is the arachnoid, a thin membrane that follows the inside of the dura leaving only a narrow space between the two, the subdural space. The last layer, the pia mater (or simply pia), closely follows the brain surface. The pia is separated from the arachnoid by the subarachnoid space (SAS), a cavity filled with cerebrospinal fluid (CSF, we will talk about it later in this section). The SAS does not have a fixed width but can vary depending on its location in the central nervous system. Moreover, it is not an empty space (Figure 2) but crossed by numerous thin threads of connective tissue connecting the pia with the arachnoid and populated with blood vessels and veins [1], [2].

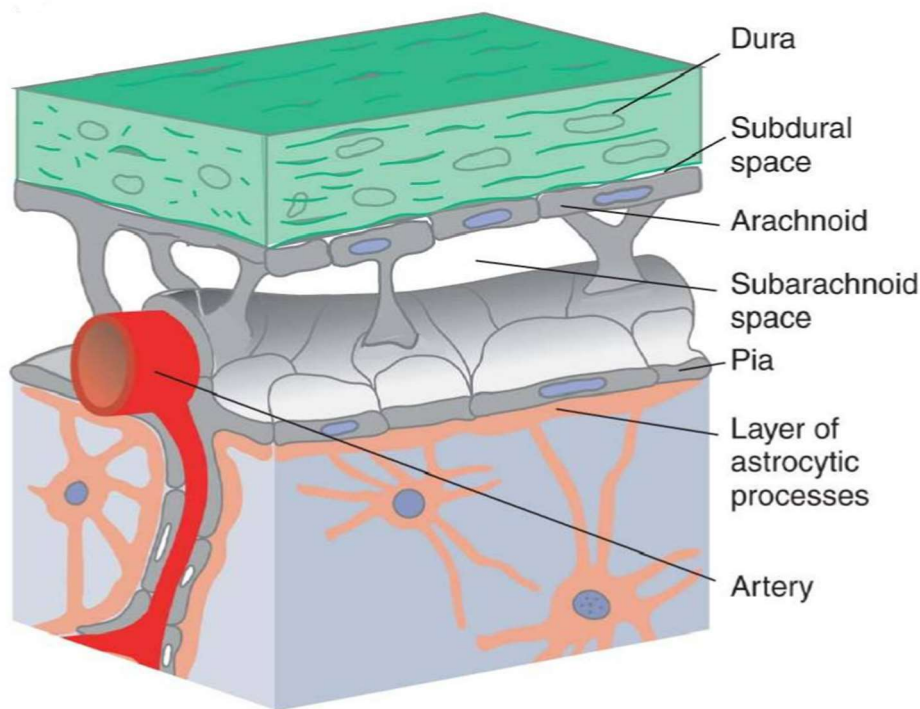


Figure 2: The components of the meninges [1]

The brain itself can be subdivided into different anatomical structures, being the cerebrum, the cerebellum, and the brainstem.

### 1.1.1 Cerebrum

The cerebrum is the biggest part of the brain and occupies most of the cranial cavity. It consists of two hemispheres. Each hemisphere is covered by a layer of 3-5 mm of gray matter, the cerebral cortex. Underneath there is the white matter. White and grey matter have different properties due to the different microstructures of which they are composed.

The nervous system is made up of two cell types: neurons and glial cells. Neurons are characterized by the ability to receive and transmit electrical signals. Figure 3 shows a schematic of a neuron consisting of a cell body or “soma”, multiples short extensions “dendrites” used for receiving signals from other neurons or cells, and a single long extension “axon” able to conduct impulses to other neurons or cells. Many axons are surrounded by a myeline sheaths which increase the conduction velocity. Myeline sheaths are produced by

glial cells, the most numerous units in the brain. Different kinds of glial cells exist that differ in structure and functions, but the main activities of this group of cells are controlling chemical stability of extracellular fluid and providing electrical insulation of neurons [1].

Cell bodies and dendrites are mainly found in grey matter, as neurons themselves are gray in color. Meanwhile, in the white matter mainly myelinated axons are found, and the white color is given by the myelin. This difference in the constitutive structures reflects on the properties of different matters [1].

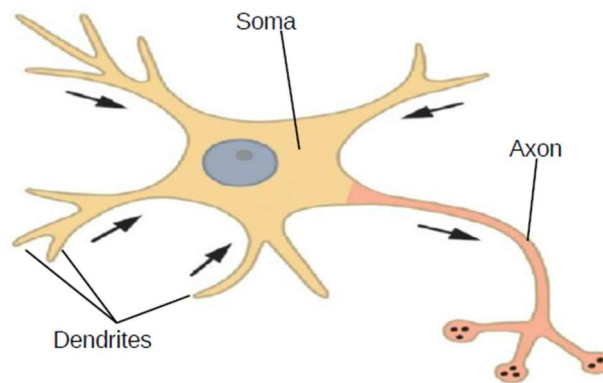


Figure 3: Schematic of a neuron [1] with arrows showing signal direction.

The cerebrum is the part of CNS where all the information is processed, indeed it is responsible for interpretation of images and sounds. Also, other complex tasks such as speaking, reasoning, and control of fine movements are governed by the cerebrum [1], [3].

### 1.1.2 Cerebellum

The cerebellum (literally “little brain”) is located at the base of the cerebrum in the posterior cranial fossa, a large depression in the floor of the cranial cavity [4] situated in the posterior part of the skull. Like in the cerebrum, two hemispheres are present, the cerebellar hemispheres. The cerebellar tonsils (one for each hemisphere) are the lowest part of the cerebellum (Figure 4: Cerebellum and brain stem sagittal section drawing [5]Figure 4) and can sometimes extend through the foramen magnum [2], the opening at the skull base. The cerebellum is responsible for the coordination of complex movements but also for posture and balance control [3].

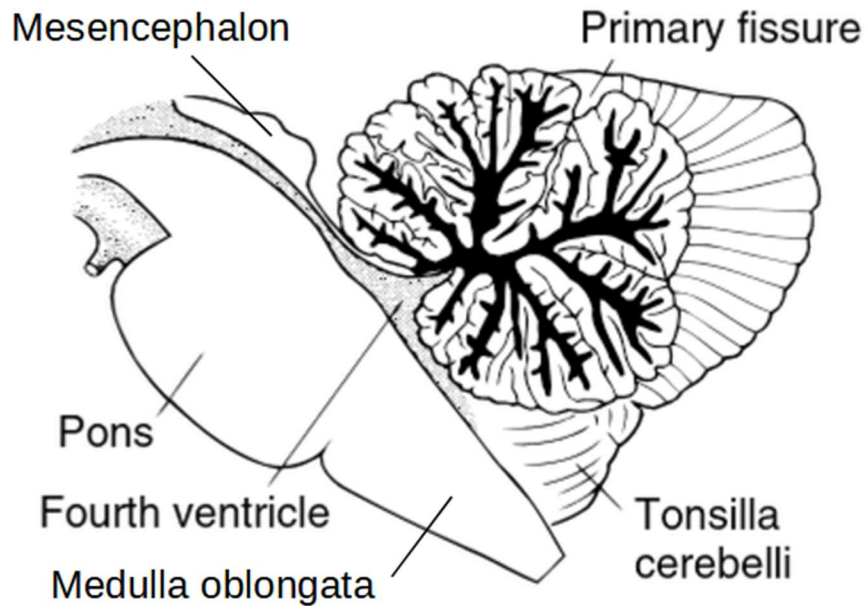


Figure 4: Cerebellum and brain stem sagittal section drawing [5]

### 1.1.3 Brain stem

The brain stem is the lower part of the brain, situated in front of the cerebellum and caudally (away from the brain) connected with the spinal cord. It is generally subdivided into three parts: the medulla oblongata (or just medulla), which extends through the foramen magnum and is directly connected with the spinal cord, the pons, and the mesencephalon (midbrain). The brainstem is the connection between the cerebrum and the rest of the body, it contains many neural nuclei and is a transit point for either sensory or motor signals. Beside this connection role the brain stem is responsible for the control of some primary functions such as blood circulation and respiration [1].

## 1.2 The spinal cord

The spinal cord is a cylinder of nervous tissue which extends from the brain stem as a downward continuation of the medulla oblongata. Its length is approximately 40-45 cm in an adult, extending from the first cervical vertebra to the second lumbar vertebra (Figure 6) [1] and thickness varies along his length with two major enlargements at cervical and lumbar level. The structure is enclosed by the vertebral column which provides mechanical support and protection [1].

The meninges covering the spinal cord are the same and continuous with those surrounding the brain. In the spine, the dura is not directly attached to the bone, but the epidural space is found between the dura and the spinal canal. This space contains fat and the veins of the internal vertebral venous plexus. Underneath the dura, there are the arachnoid, the subarachnoid space (SAS), and the pia, as in the brain. Two incomplete membranes (septa), named denticulate ligaments (Figure 5), laterally connects the spinal cord with the arachnoid and dura mater. At his caudal (lower) extremity, the spinal cord ends with a conic shaped section named conus (Latin for cone). Below this end some spinal nerves extends inside the

vertebral canal forming a collection known as cauda equina (horsetail), as illustrated in Figure 6 [1]. Although the spinal cord terminates at the level of the lumbar region, as depicted in Figure 6, the arachnoid, the dura, and the subarachnoid space extends up to the sacrum (the lower region of the spine) [1], [2].

The spinal cord is a segmental<sup>1</sup> structure. From each segment, a pair of spinal nerves depart as depicted in Figure 5. A total of 31 pairs of spinal nerves (8 cervical, 12 thoracic, 5 lumbar, 5 sacral, and 1 coccygeal) connects the CNS with the rest of the body. Spinal nerves are both afferent (carrying impulses to the CNS) and efferent (carrying impulses from the CNS to the effectors) pathways, transmitting both sensory and motor information [1].

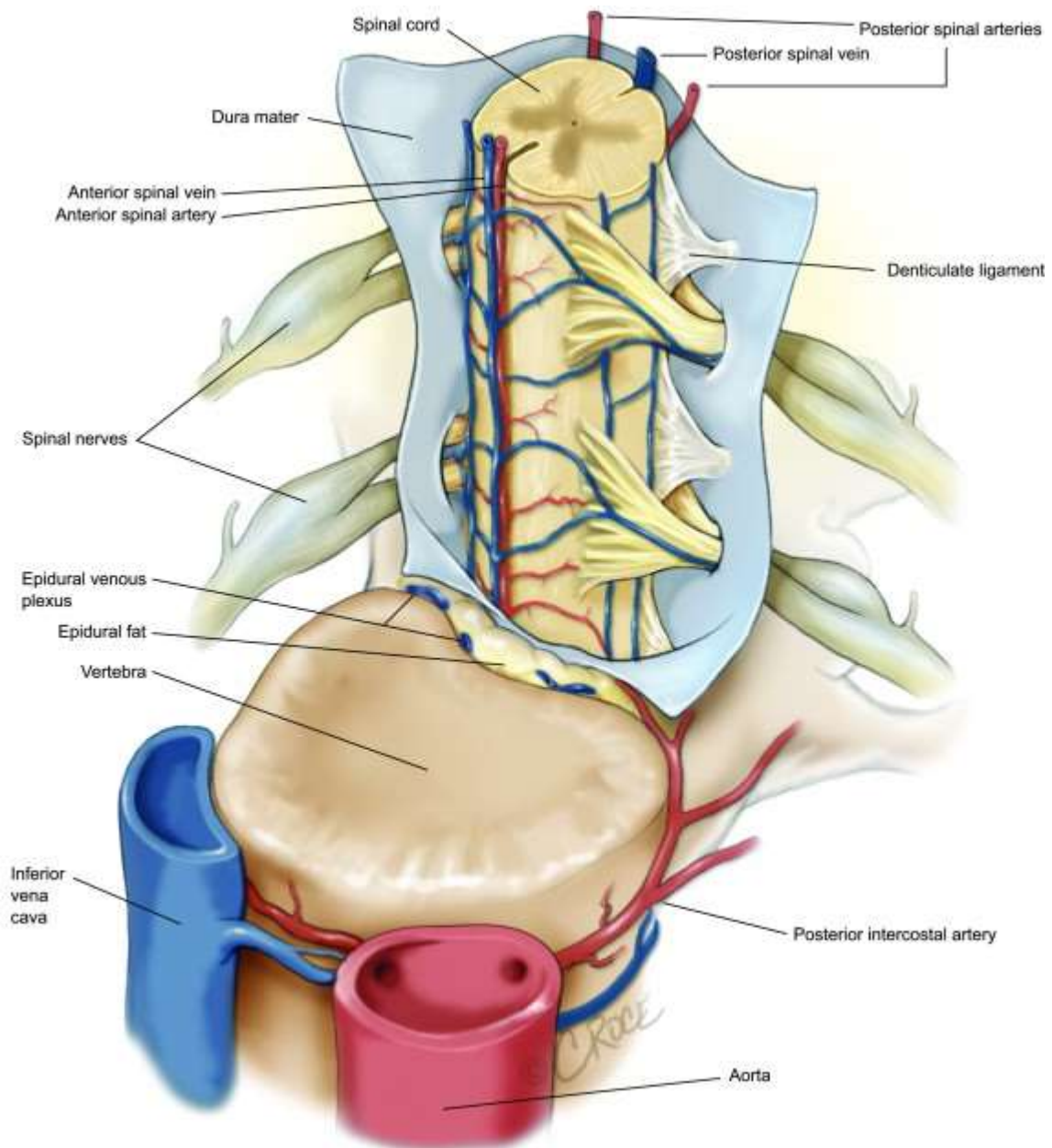


Figure 5: Anatomy of the spinal cord [6]

<sup>1</sup> Segmental: divided into segments [4]

As depicted in Figure 6 the spinal cord is composed of a central region of gray matter, consisting of nerve cell bodies, surrounded by a region of white matter, containing nerve fibers. The center of the cord is the central canal, a narrow opening communicating with brain's ventricular system and ending in the caudal end of the cord. As cord's section is not constant, also the proportion and shape of white and gray matter regions vary along the spinal cord length.

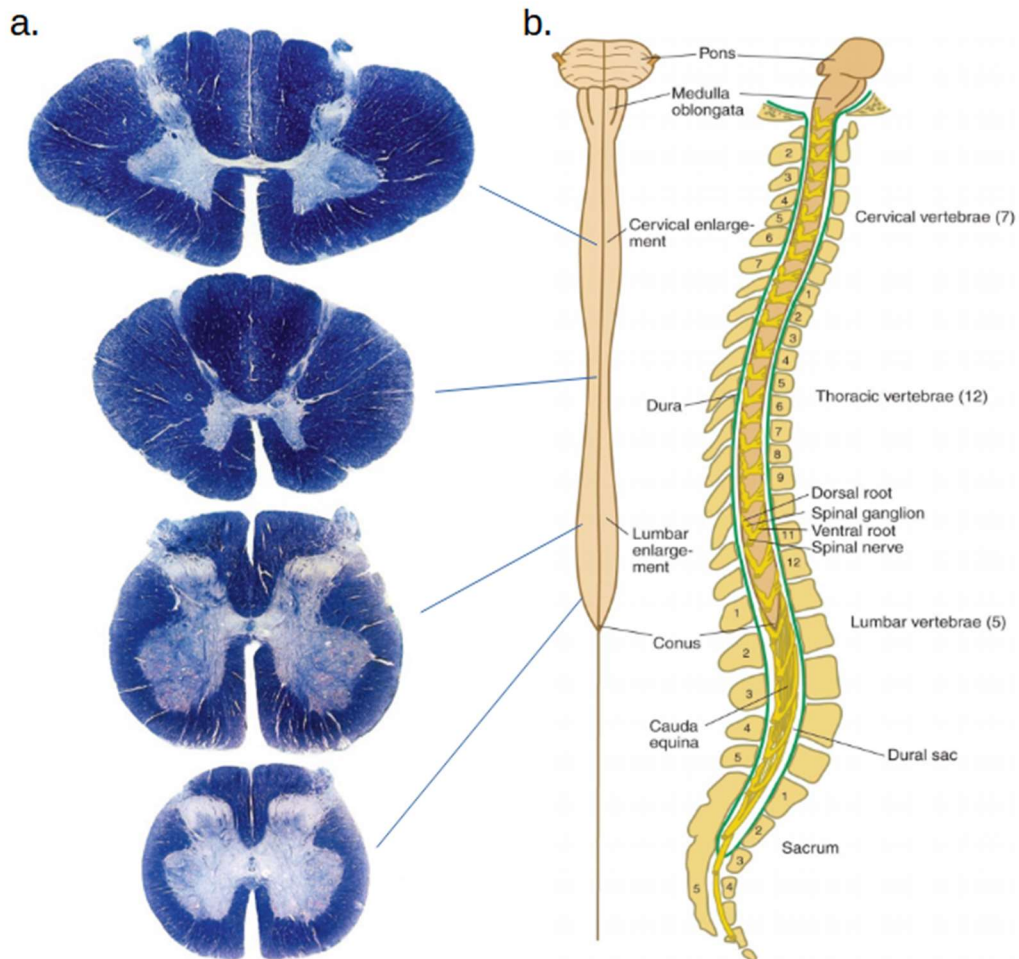


Figure 6: Image showing a) Spinal cord sections at different levels [2]. b) Spinal cord overall shape and spinal cord fitting into the spine [1].

The gray matter region of the spinal cord is H-shaped, with four protrusions, two dorsal (posterior) and two ventral (anterior) horns (figure 6). Size and shape of the horns changes depending on the level. Three main types of neurons can be identified inside the spinal cord and they can be distinguished based on where they send their axons. The first type is neurons sending their axons out of the CNS to deliver signals to muscles and glands. The second type is neurons sending their axons to higher levels of the CNS to inform the brain of body and spinal cord activities, indeed they receive signals from sense organs. The last type is neurons sending their axons to other parts of the spinal cord. The axons of these cells do not leave the spinal cord and they establish connections with other neurons in other segments [1].

The white matter of the spinal cord can be divided into anterior, posterior, and lateral funiculi (bundle of nerve fibers [4]). It is composed of long myelinated axons organized in tracts that can be ascending or descending.

### 1.3 Interstitial fluid

The CNS extracellular spaces, which cover up to 23% of the overall brain volume, are filled with interstitial fluid (ISF) [6]. It is a fluid derived from water crossing the blood-brain barrier<sup>2</sup> and from brain's metabolic activity. Maintenance of ISF balance is a basic element for every organ function. In the CNS, the flow exchange between CSF and ISF contributes to regulation of this balance and clearance of waste products from the ISF. As depicted in (Figure 7), the main way for this fluid exchange is through peri-vascular or "Virchow-Robin" spaces [7], which are spaces connected with the SAS and filled with CSF [7]. They surround every blood vessel entering the brain or the spinal cord. The layer of pia surrounding perivascular spaces become more porous with the increasing depth from the brain or spinal cord surface [6].

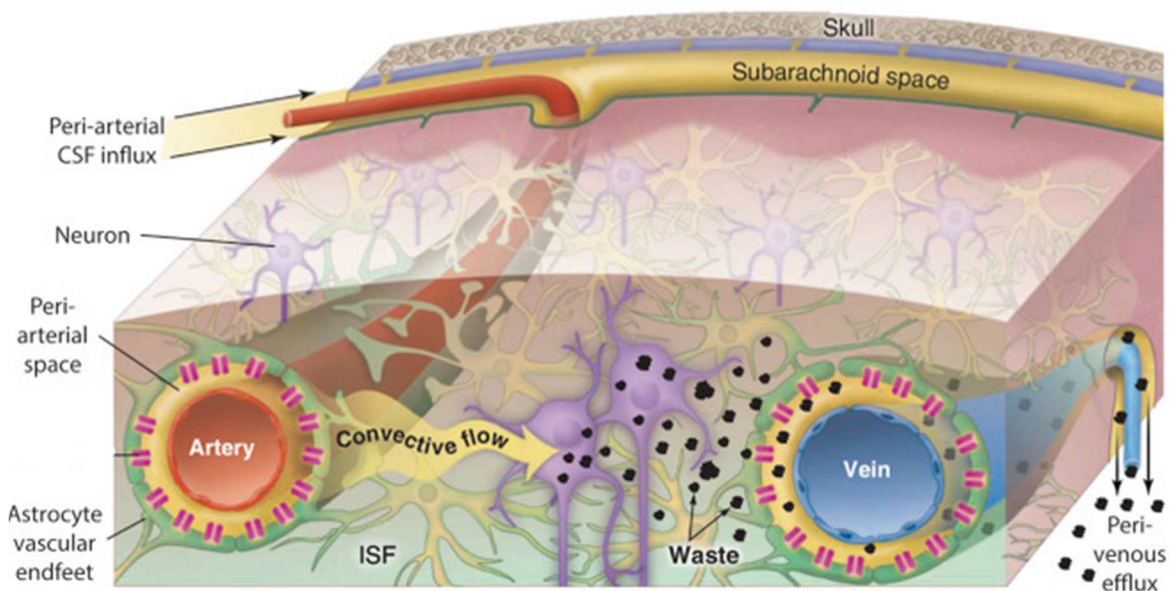


Figure 7: Exchange of CSF and ISF along perivascular spaces [6]

### 1.4 CSF pathways

Cerebrospinal fluid (CSF) was already mentioned as it fills the subarachnoid space surrounding the brain and the spinal cord. Cerebrospinal fluid is clear and colorless, with a density like water ( $1,003 - 1,008 \text{ g/cm}^3$  [8]). In an adult CNS there is on average 140 ml of CSF, divided between the cranial subarachnoid space, the spinal canal, and the ventricular system, a system of four communicating cavities presents inside the brain. The primary function of CSF is to protect the brain and the spinal cord from impacts with the surrounding bone tissue. Research and theoretical calculations suggest that the buoyancy of the brain in the CSF can

<sup>2</sup> Blood-Brain Barrier: "a naturally occurring barrier created by the modification of brain capillaries [...] that prevents many substances from leaving the blood and crossing the capillary walls into the brain tissues." [4]

reduce its weight from 1500g to only 50g, drastically reducing the mechanical stress on nerves and vessels connected with CNS [1], [8].

CSF is mainly produced by the choroid plexus, a structure present inside all the four ventricles producing CSF at an approximate rate of 500 ml/day [1], [8]. The choroid plexus is an epithelial structure like ependyma (the inside covering of ventricular system), highly vascularized and arranged in a complex structure of thin branching protrusions called villi. Unlike ependyma the epithelial cells of choroid plexus have tightly sealed junctions, which prevents any traffic of solutes between blood and CSF and forms the blood-CSF barrier [1], [8].

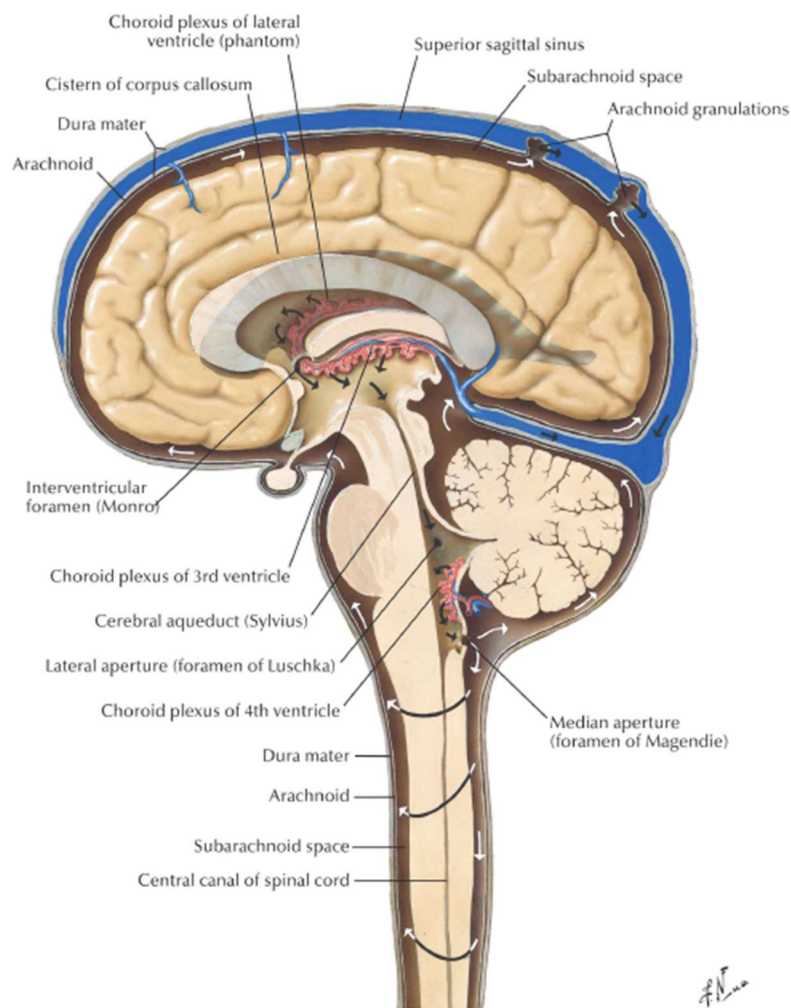


Figure 8: Image of CSF pathways [8]

The cerebrospinal fluid produced in the lateral ventricles flows into the third ventricle through the interventricular foramen (of Monro). Next, it reaches the fourth ventricle through the cerebral aqueduct (aqueduct of Sylvius). From there, the liquid leaves the ventricular system through three openings, the midline foramen (of Magendie) and the two lateral foramina (of Luschka). The CSF is then free to spread out over the cranial subarachnoid space and the spinal canal [8] (Figure 8). Throughout its entire path, CSF moves in a pulsatile manner. This results from cardiac-cycle related variations in cerebral blood volume as well as brain and spinal cord movements (also related to cardiac cycle). Respiratory functions also affect CSF movement,

i.e. during a cough or Valsalva's maneuver CSF flows first cranially (to the head) than caudally (away from head [8]). Another element influencing the CSF flow is the body position in the space. The effect of gravity will be reflected on CSF flow differently if the subject is lying on the back, is standing, or is doing movements such as standing up quickly or lifting objects.

Cerebrospinal fluid reabsorption routes are not completely known but arachnoid villi are usually assumed to be the main responsible of CSF drainage. Arachnoid villi are small infoldings of the arachnoid, they are organized in protrusions called arachnoid granulations. Arachnoid granulations are in venous areas to allow the reabsorption of CSF into the venous flux [8]. Beside this mechanism, new findings show the existence of another drainage route involving the lymphatic system [9].

Different pathologies are related to CSF disorders. They arise from different origins as metabolic disfunctions or pathways blockage and can be detected either in children or adults. Hydrocephalus is a condition in which an imbalance in the formation, flow or reabsorption of CSF leads to excess of CSF volume or elevated pressure inside the skull. In adults, this condition compresses the brain and impair its functions [8]. Depending on the pathophysiology it can be classified as acquired or congenital, and obstructive or communicating [10]. Trauma during surgery, meningitis or shrinking of the cerebrum due to dehydration can lead to fluid collection located in the subdural space, so-called Peri cerebral collections, which can cause impairments in CSF reabsorption and eventually external hydrocephalus [8]. Another relevant pathology related to the CSF is Syringomyelia related to Chiari malformation, which will be the focus of this work. Details about these conditions are given in the following chapters.

## 2 Chiari Malformation

### 2.1 Pathophysiology

Chiari Malformations are a group of deformities of the posterior fossa and the hindbrain. They are classified in four types, depending on their morphology and severity of anatomical defects. Typically, diagnosis and classification are possible through imaging techniques; usually magnetic resonance imaging (MRI) is the golden standard [11].

Chiari Malformation Type 1 (CMI) is the most common but least severe type. It is characterized by the herniation of cerebellar tonsils through the foramen magnum for a minimum of 3-5mm inside the upper cervical spinal canal (figure 9). Different causes have been proposed to explain the pathogenesis of this malformation. Most of them suggest that it is linked with limited or abnormal development of the skull, resulting in a reduced posterior fossa. This forces the cerebellar tonsils, whose volume is unchanged, to herniate through the foramen magnum [12]. However, not all patients presenting CMI have a small posterior fossa, so there is not yet agreement about the causes leading to this condition.

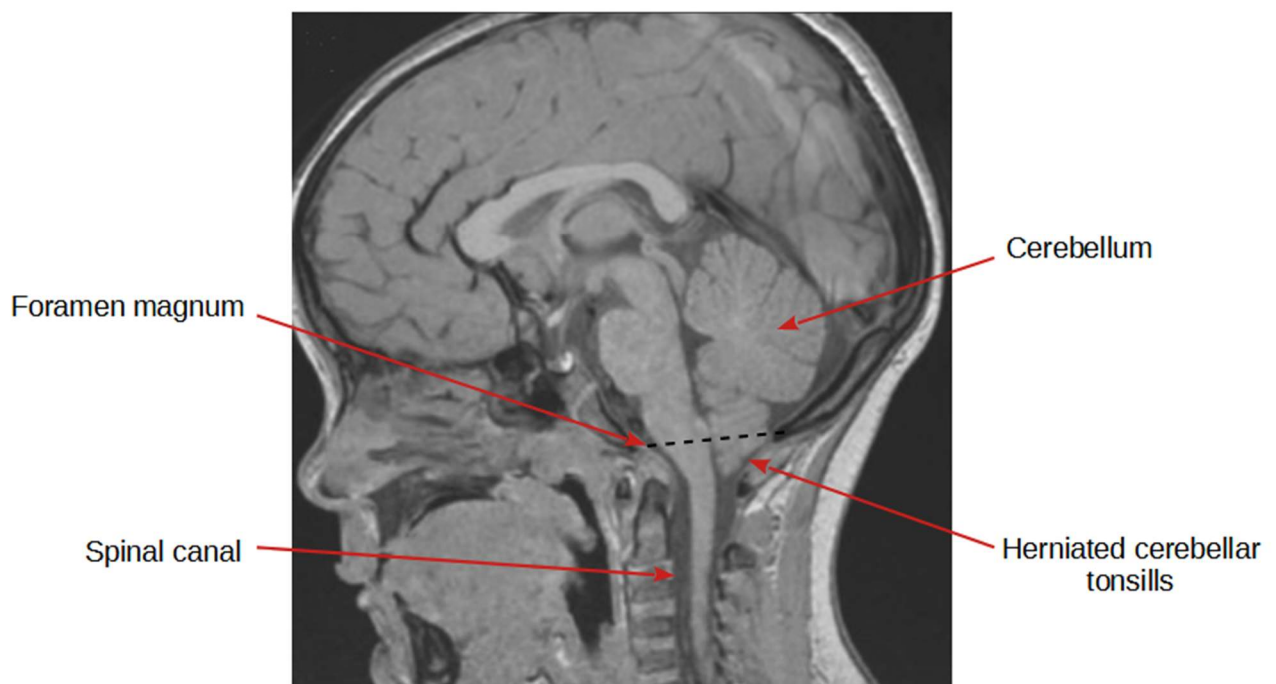


Figure 9: Sagittal T1 image of a patient showing Chiari Malformation type 1, with a herniation of approximately 7mm [13]

CMI can be associated with various other anatomical anomalies, i.e. Hypoplasia, Spina bifida, Hydrocephalus, Hydromyelia, Syringomyelia. As CMI can occur in combination with many other anomalies, has been difficult to find a theory able to explain all these possibilities [14].

CMI prevalence has not been clearly stated yet although, some imaging studies have been conducted to assess it. In a review of 22,591 patients undergoing brain MRI, Meadow et al. [15] found 175 patients showing CMI, resulting in a prevalence of 0,77%. Aitken et al. [16] performed a similar study on a pediatric population (people under age 20) of 741,815 subjects

who underwent an MRI scan. They even found a prevalence of 1,0%. Meanwhile, the frequency of CMI diagnose in the whole population was estimated to be 0.7 out of 10,000. Other studies like Strahle et al. [17] showed higher prevalence, up to 3,6%.

Many patients with Chiari type 1 malformation are asymptomatic and symptoms may only show in at an older age. According to different studies [16], [18], the most common symptoms related to CMI are headache (experienced by 81% in Milhorat et al. study [18]), neck pain and vertigo. Other otoneurological<sup>3</sup> disturbance such as dizziness or hearing loss are common in adult patients.

## 2.2 Treatment

The treatment of patient with CMI should be evaluated considering not only the diagnosis done via imaging (MRI) but primarily the symptoms presented by the patient, i.e. Mastorakos et al. [19] advised to carefully evaluate the clinical findings before deciding for a surgical treatment and Fernandez et al. [20] clearly states that asymptomatic patient should never be considered for surgical treatment.

Non-surgical approaches presented in [19] vary from pharmacological treatments (drugs for pain relief) to osteopathy (manipulation of the region to reduce symptoms). All these treatments are useful to relief patient's pain and counteract the symptoms, but do not act on the causes. Thus, this approach does not solve the problem and can be applied for patients with mild symptoms only. For severe symptomatic patients, a surgical approach is needed. Surgical treatment aims to achieve the restoration of CSF flow through the foramen magnum and consists of a decompression procedure named "Posterior fossa decompression" (PFD). During the procedure, a section of the skull surrounding the cranial posterior fossa is removed (Figure 10). The posterior arch of C1 vertebra could also be removed. This resection increases the available space, avoiding the tonsils to be forced down into the foramen magnum. PFD can be combined with other procedures, like duraplasty and partial tonsillar resection [21], which can be carried out during the same surgery. A duraplasty is a procedure of reconstruction of the dura mater which is opened during the decompression procedure and partial tonsillar resection. The duraplasty is usually performed using synthetic tissue grafts [22]. Surgical decompression results in a resolution of symptoms in 83% of patients [20]. However, the procedure is complex and showed the insurgence of different complications during or after surgery. In a study analyzing 2649 patients who underwent PFD or PFDD between 2000 and 2009, Shweikeh et al. [23] found that 14.6% (387 patients) showed complications. Particularly, 1.3% needed a reoperation, 5.9% (156 patients) developed Hydrocephalus, 3.9% (102 patients) developed Pseudomeningocele<sup>4</sup> and 1.4% (38 patients) had procedure-related complications including bleeding and infections.

---

<sup>3</sup> An otoneurological disturb is a disturb related to ears and brain, as dizziness or hearing loss.

<sup>4</sup> "A pseudomeningocele is a collection of CSF not lined by arachnoid or dura mater." [60]

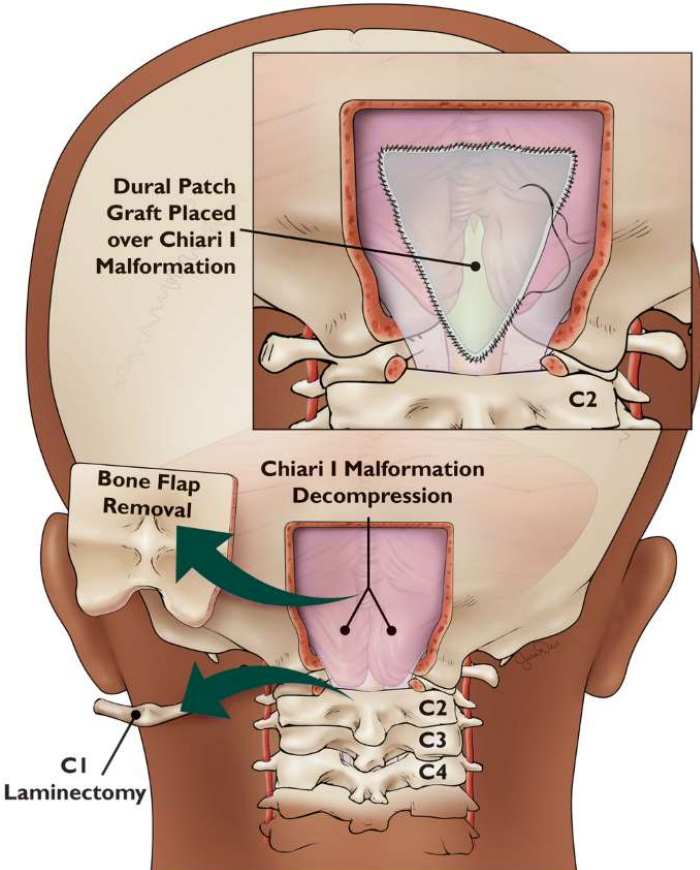


Figure 10: Schematic of PFD with duraplasty [24]

### 3 Syringomyelia

#### 3.1 Pathophysiology

The most common defect associated with Chiari Malformation type 1 is syringomyelia, which develops in almost 40-75% of patients with CMI. Up to 90% of syringomyelia are associated with CMI [20] and most of the others are post-traumatic. Syringomyelia is a neurological disorder characterized by the presence of a fluid-filled cavity inside the spinal cord [25] (Figure 11). The syrinx cavity is filled up with a clear fluid similar to CSF or extracellular fluid. Usually, the Syrinx develops at cervical level, but the cavity may also extend cranially (upwards) to the brain stem or caudally (downwards) to the thoracic level.

Syringomyelia can be classified into 4 different types [20] presented in the following Table.

Table 1: Different types of Syringomyelia.

<b>Type 1</b>	<b>Syringomyelia associated with an obstruction of foramen magnum due to CMI, a tumor or other causes.</b>
<b>Type 2</b>	Syringomyelia without foramen magnum obstruction, or idiopathic.
<b>Type 3</b>	Syringomyelia associated with other spinal cord pathologies like tumors, myelopathy, spinal arachnoiditis or myelomalacia due to spinal cord compression.
<b>Type 4</b>	Syringomyelia associated with hydrocephalus, pure hydromyelia.

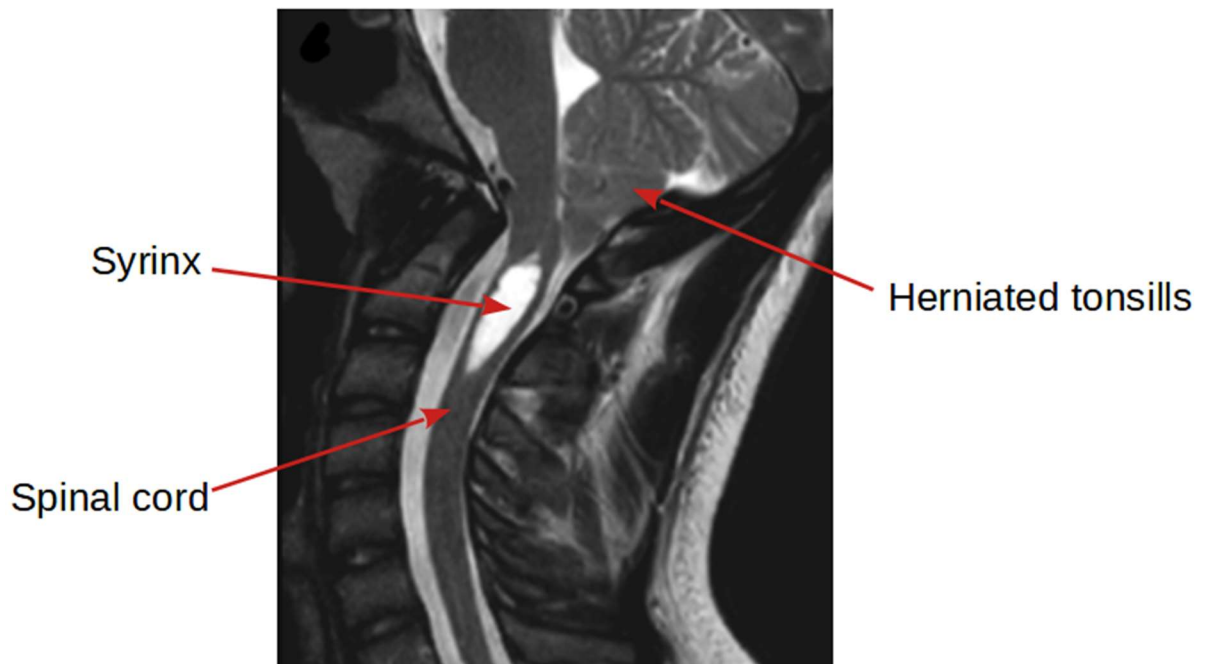


Figure 11: MRI of a patient with CMI related syringomyelia [22]

Symptoms of syringomyelia are mainly due to mechanical stress applied to neurons of the spinal cord subsequently to syrinx formation. Following Aghakhani et al. [26], a study about the outcome of surgical treatment of Chiari related syringomyelia, most present symptoms were pain (70%), sensory disturbance (23%), and motor weakness (22%). A more recent study by Sivaramakrishna et.al [27], highlighted the same symptoms but with much higher incidences. The difference between these studies may be the result of differences in study criteria, but also because they were investigating in different periods (1989-2000 for [26], 2012-2015 for [27]).

Based on these two studies, the symptoms related to Syringomyelia can be grouped in 3 categories: Pain (neck pain, sub-occipital pain), motor (weakness, scoliosis), and sensory problems.

### 3.2 Treatment

Treatments for syringomyelia are different depending on the causes. Mainly we can distinguish two groups, post traumatic syringomyelia and Chiari related syringomyelia.

To treat post traumatic syringomyelia different techniques can be used. A recently published literature review by Kleindienst et al. [28] considering reports from 1980 to 2020 highlights two main surgical treatments. According to this review the most used procedure is the arachnoid lysis, chosen in 48% of the cases and presenting a failure rate of 5-7%. This procedure has the goal of restoring the free CSF passage and decompress the spinal cord [29]. The second most used procedure reported by Kleindienst et al. [28] are drainage procedures, used in 31% of cases. Drainage procedures aims to remove a certain fluid from a space, either removing it from the body or directing it in a location where it can be reabsorbed. Various methods of drainage exist, shunting procedures (Figure 12) are widely investigated and reported in literature. Shunting consists in the insertion of a shunt allowing the syrinx to communicate with other spaces, that can be the peritoneum<sup>5</sup>, the pleura<sup>6</sup> or even the subarachnoid space. The purpose is to connect the syrinx with a space where the fluid can be drained and reabsorbed. Shunting procedures are difficult, have a high failure rate reported around 50% [29] and can lead to many complications.

Chiari related syringomyelia is usually treated not acting on the syringomyelia itself, but on the original cause, being the Chiari malformation. The surgical procedure used is the Posterior fossa decompression with (PFDD) or without (PFD) duraplasty. Despite this surgery usually helps to reduce syrinx volume or even completely solve it, the outcomes may be variable, and many dangerous complications may occur. Hence, there is a need for more new treatments.

---

<sup>5</sup>Peritoneum: the smooth transparent serous membrane that lines the cavity of the abdomen of a mammal and is folded inward over the abdominal and pelvic viscera [4].

<sup>6</sup>Pleura: the delicate serous membrane that lines each half of the thorax of mammals and is folded back over the surface of the lung of the same side[4].

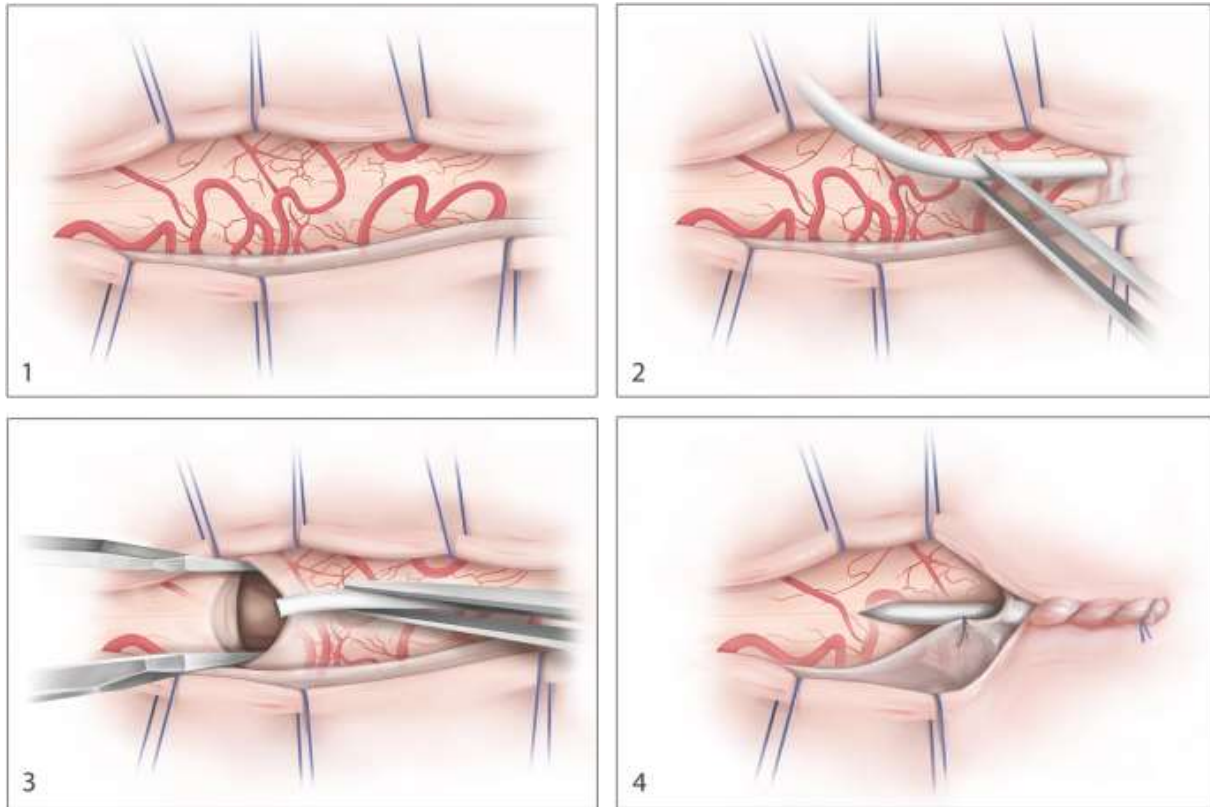


Figure 12: Illustration of main steps of syrinx-SAS shunting procedure. 1-View of pinal cord after dura opening. 2-The shunt catheter is inserted into the SAS. 3-The syrinx cavity is opened and one end of the catheter is inserted into the cavity. 4-The shunt catheter is sutured to the arachnoid, to avoid dislocation. [30]

### 3.3 Theories about syrinx formation

The pathophysiology leading to the formation of the syrinx in Chiari Malformation type 1 patients has not yet been clarified. Several theories have been proposed to explain this phenomenon. All of them agree that the disruption of the CSF flow at the cranio-cervical junction plays a central role but each one proposes a different mechanism for syrinx formation [25].

Since the problem of syrinx formation was first addressed, different theories have been proposed. Chronologically the first was the so called “Water-Hammer pulse theory”, proposed by Gardner in 1958 [31]. In healthy patients the expansion of the arteries inside the skull, happening during the systole, is balanced by the downward flow of CSF through the foramen magnum into the spinal subarachnoid space. Gardner’s theory basically states that the presence of an obstruction of the foramen magnum prevent the CSF to flow downward during systole (Figure 13), forcing the CSF to flow from the 4<sup>th</sup> ventricle inside the central canal where it is trapped and forms the syrinx.

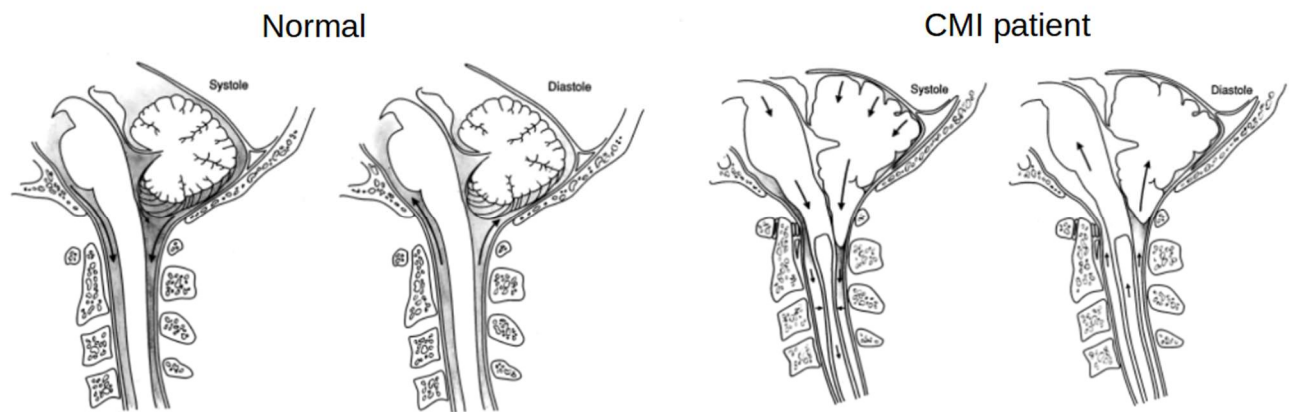


Figure 13: Comparison of CSF and cerebellar tonsils movement through the cardiac cycle [32]

A modernized version of the previous theory was provided by Williams [33]. Williams describes the herniated tonsils as a partial one-way valve, allowing almost exclusively an upward flux of CSF through the foramen magnum. He also stated that the Valsalva's maneuvers play an important role in the development of the syrinx. A Valsalva's maneuver<sup>7</sup> (e.g., sneezing, coughing) will lead to an expansion of the veins in the spinal venous plexus, this expansion will force the CSF out of the spinal canal into the skull. That will suddenly increase the pressure inside the skull, according to Williams [34] the pressure difference between head and spine can rise to 100 mmHg in this phase. In a normal subject the pressure will drop rapidly due to the CSF coming back from the intracranial compartment into the spinal cord. In patients with Chiari malformation the one-way valve effect of herniated tonsils will not allow CSF flowing downward to the spinal cord, and that will lead to a large pressure difference between the spinal canal and the head. In this situation, there is an accumulation of CSF inside the skull (increasing the pressure). So, CSF will be forced (sucked) into the spinal canal to balance the pressure, giving rise to syrinx formation and enlargement.

The major issue of these first two theories is that in many patients there is no communication between the syrinx and the 4<sup>th</sup> ventricle. Moreover, the central canal cannot be seen in MRI scans, which complicates the investigation of this canal as the entrance path of CSF to syrinx.

In contrast, Oldfield et al. [35] hypothesized that the origin of syrinx formation was the migration of CSF from the subarachnoid space. They stated that the downward moving pressure wave, generated in the intracranial space, periodically pushes down the cerebellar tonsils. Consequently, the tonsils act as a piston pushing the CSF present in the spinal SAS to enter the spinal cord and thus generating a syrinx.

Gent university hospital's neurosurgery department proposed a new theory based on several clinical observations. This new theory keeps some elements of the previous ones. As proposed by Williams[33], they describe the tonsils behavior as a one-way valve and consider the subsequent pressure difference as the cause of syrinx formation They theorized that this pressure difference leads to tensile stresses acting on the spinal cord, eventually leading to

<sup>7</sup>Valsalva maneuver: a forceful attempt at expiration when the airway is closed at some point [4].

accumulation of interstitial fluid in the spinal cord. Thus, in contrast to the previous hypotheses that the fluid inside the syrinx is “sucked” through the central spinal canal, this novel theory could give an explanation to syrinx formation in patients without a central canal or non-communicating syringomyelia. They highlighted that the tonsils obstruction must not be considered as solid, but as *“fragile balance which can be easily reversed.”* It was stated that during the “steady-state” the tonsils allow a slow downward CSF flow, able to slowly compensate the pressure imbalance. Disruption of this “steady-state” can be caused by Valsalva’s maneuvers or rapid postural changes (e.g., standing up quickly). Unique preliminary findings showed that avoiding such movements and other measures aimed to limit venous drainage when changing position, as lower limbs compression, can lead to an important syrinx volume reduction.

## 4 State of the art

The study of Chiari malformation-related syringomyelia has always required researchers to face some important issues. The recurrence of the pathology itself limited the possibility to gather new information from clinical observation, and the methods to gather in vivo data (pressures or velocities) are highly invasive. Moreover, the required measurement locations are not easily accessible. Nowadays new techniques such as Phase-contrast Magnetic resonance imaging (PC-MRI later described) allow for velocity measurements, but pressure measurements still require invasive procedures.

### 4.1 Introduction to experimental and in vivo techniques

As already mentioned, methods to gather experimental in vivo data are quite invasive. For example, Heiss et al. [32] inserted two spinal needles at C1-2 and L4-5 level to gather CSF pressure measurements (showed in Figure 14) in spinal SAS. To correctly position the needles fluoroscopic guidance was necessary. Other measurements such as the pressure inside the ventricle or the syrinx could only be performed during surgery, as done also by Milhorat et al. [36] two years earlier. Therefore, new advances in imaging techniques drastically improved the possibility to observe and study syringomyelia.

Pressure recordings in 19 patients with Chiari I malformation and syringomyelia and in 18 healthy volunteers\*

Measurement	Patients Pretreatment	Healthy Volunteers (p value)	Patients Posttreatment (p value)
cervical pressure (mm Hg)			
mean	15.5 ± 5.6†	11.2 ± 2.5 (0.006)	9.7 ± 2.1 (0.02)‡
pulse	2.3 ± 0.6†	1.6 ± 0.6 (0.002)	1.8 ± 0.6 (0.04)‡
lumbar pressure (mm Hg)			
mean	13.0 ± 3.0†	11.2 ± 2.3 (0.05)	10.2 ± 2.1 (0.004)‡
pulse	1.3 ± 0.7	1.0 ± 0.4 (0.15)	1.1 ± 0.6 (0.49)
craniospinal compliance (ml CSF/mm Hg)	3.3 ± 2.3†	6.0 ± 4.0 (0.02)	5.6 ± 4.0 (0.05)‡
jugular compression			
rate of increase (mm Hg/sec)	4.2 ± 1.8†	6.6 ± 2.0 (0.001)	6.9 ± 2.4 (0.006)‡
peak intrathecal pressure (mm Hg)	37.6 ± 9.4	35.4 ± 8.9 (0.48)	35.3 ± 8.0 (0.17)

\* Values are expressed as the mean ± standard deviation. One patient refused preoperative and postoperative pressure recording, although he underwent all other tests.

† Significant difference compared with healthy volunteers (unpaired t-test).

‡ Significant difference compared with pretreatment patient group (paired t-test).

Figure 14: Pressure recordings in [32].

MRI helped to better observe the anatomy of the pathology and to lead less invasive patient follow-up. Phase contrast MRI (PC-MRI) is a magnetic resonance imaging technique that take advantage of the flow-dependent phase of MR signal to calculate flow velocity. Two different images are acquired with different velocity-dependent signal phase. Subtraction of the two images allows calculation of velocity images. This technique can provide 2D velocity maps for an individual slice; multiple slices can be acquired and aligned to have an idea of the 3D flow field [37]. 4D-MRI relies on the same principle as PC-MRI. In this case four different images are taken simultaneously: a reference image, and three velocity encoded images along the three main axis. By comparing the velocity encoded images with the reference one is possible to

visualize the time evolution of the flow in a 3D space. 4D-MRI allows an easier evaluation of moving fluid volumes and minimizes errors due to misalignment of the analysis plane which may occur in PC-MRI [37].

The mentioned difficulties and limitations of in vivo measurements led to the use of in vitro models for evaluation of CSF pressures and velocities in the SAS and spinal cord [38]. In vitro measurements can be useful to get some data which may be hard to get in in vivo models.

A mechanical model was built by Martin et al. [38] to investigate the pressure environment in different situations of stenosis and syringomyelia. They performed experiments with 4 different setups: I- syrxinx and aligned SAS stenosis, II- only syrxinx, III- only stenosis, IV syrxinx with cranially located stenosis to mimic Chiari malformation-related syringomyelia. The model was built with a total length of 48cm and pressure sensors every 4cm (Figure 15). To reproduce the spinal cord a material with a Young's modulus of 500 kPa was chosen. At cranial end, a computer-controlled pump imposed a cyclic pressure wave.

In the model of Chiari malformation, the pressure fluctuation in the syrxinx was nearly identical to the one observed in the SAS. Based on the results of this model, the researchers concluded that large pressure differences between the syrxinx and SAS cannot be attributed to a stationary flow blockage at the craniospinal junction. Rather, a valve mechanism (like the one proposed by Williams [33]) should be present to produce greater pressure differences. Indeed, a valve mechanism will be more efficient in avoiding the fluid flow from spinal to cranial SAS.

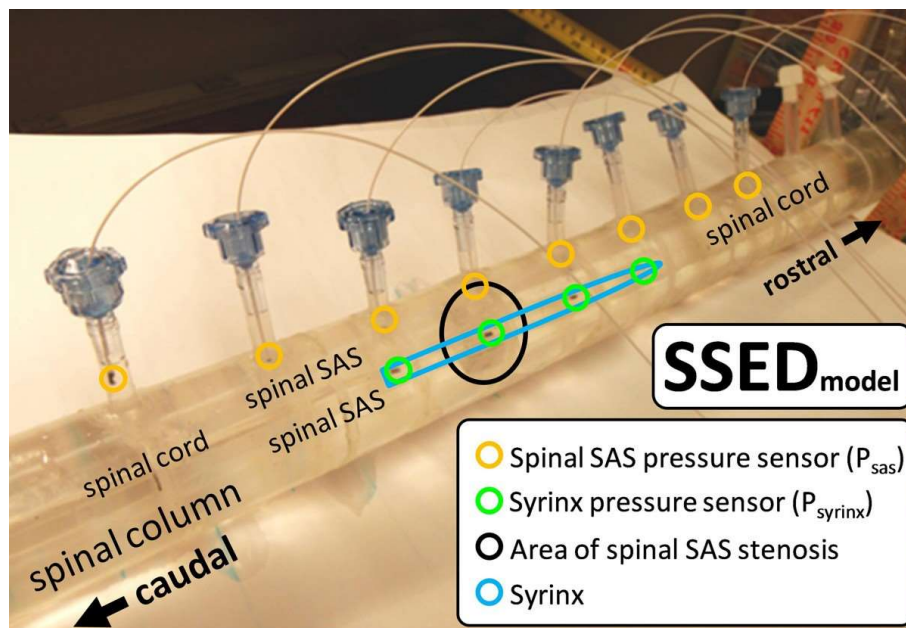


Figure 15: Picture of the model used by Martin et al. [38], from ref. [39]

Even though experimental models may be useful to understand the complexity of the problem, they have some important limitations. The complex geometries and different tissues are difficult to replicate, neither are the boundary conditions [39].

## 4.2 Numerical methods

Given the issues in the carrying of experimental research, computational models are in general the preferred option to study syringomyelia, either with idealized or subject-specific geometries. With computational modes it is possible to investigate complex geometries otherwise hard to reproduce. These models allow us to observe the complete field distribution of variables (pressures and velocities), also providing information about difficult to measure locations. Therefore, numerical simulations played a crucial role in the study of syringomyelia during the last two decades.

### 4.2.1 CFD models

It is widely accorded that disturbed fluid dynamics plays a central role in CMI and in syrinx development. That is why computational fluid dynamics (CFD) models are the most used modelling method for the study of this condition. They have been used to study the effect of CMI on CSF flow in terms of pressure and velocities.

Helgeland et al. [40] leaded a numerical (CFD) simulation in a patient-specific geometry of the spinal canal. The pulsating flow of CSF was simulated for 29 cardiac cycles using a time varying velocity pulse defined at the geometry's lower boundary. The pulse amplitude was set to generate systolic and diastolic peak velocities in the order of 10cm/s and 7,5cm/s, in accordance with PC-MRI measurements reported by Shah et al. [41]. They performed an analysis of Reynold's numbers in the flow to assess the locations where the stability of the flow is most likely to be compromised. They found a highly heterogeneous distribution of CSF velocities, synchronous bidirectional flow, pressure and velocities in accordance with those reported in other researches [40]. As depicted by Figure 16, the higher Reynold's numbers were registered in the region near the deformation, identifying it as the most significant region of unstable flow. In this study some anatomical structures (as nerves and denticulate ligaments) where neglected and the walls were assumed to be rigid.

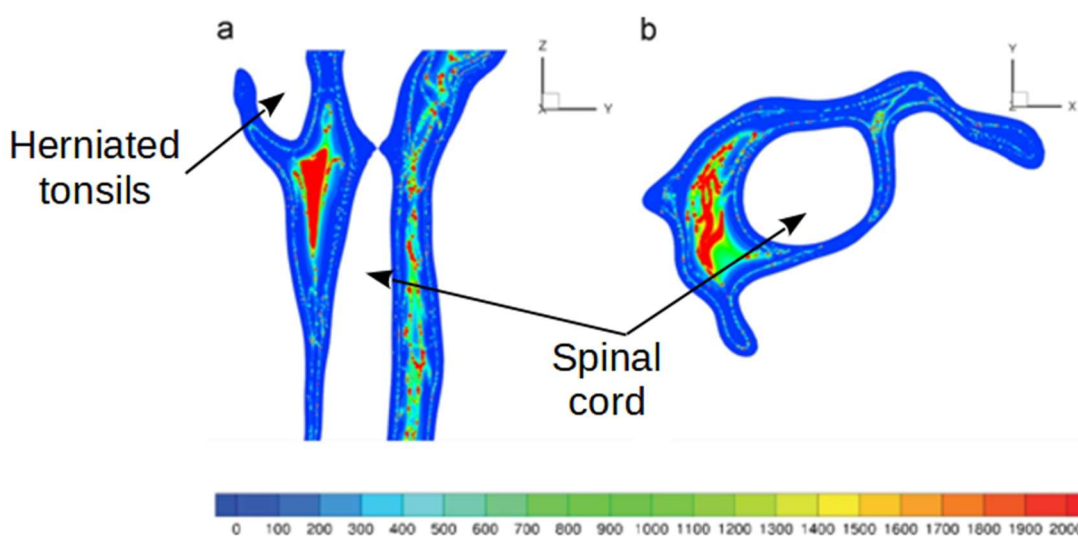


Figure 16: Contours of general Reynold's numbers for a vertical (a) and horizontal plane (b) [40]

Clarke et al. [42] performed a comparison between the CSF flux in three different patient-specific geometries: one derived from a healthy patient, one from a patient with CMI but no syringomyelia, and one with CMI and syringomyelia (Figure 17). Flow's boundary conditions for these simulations were calculated fitting a Fourier function to the data from PC-MRI scans. In this way both upper and lower boundary conditions were calculated. Simulations showed a good correlation with MRI measured velocities, with no significant difference in peak values for any of the three cases. These simulations suggested the pressure magnitude to be strongly influenced by the anatomy at the cranio-cervical junction. However, pressure's peak values were closer to normal in patients with syringomyelia than without [42]. Moreover, the pressure values calculated in the model with syringomyelia were quantitatively consistent with the ones found by Martin et al. [39]. As in the work of Helgeland et al. [40], in this model walls were assumed to be rigid.

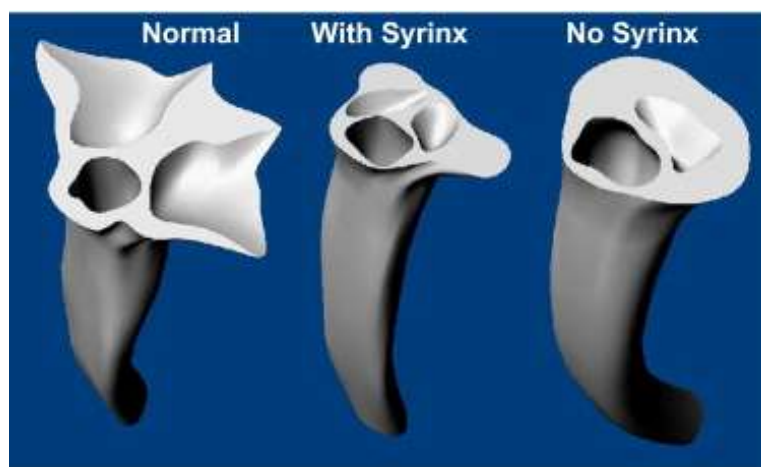


Figure 17: Different geometries used in Clarke et.al [42]

In the works presented above the anatomical structures present inside the subarachnoid space were always neglected. A study of Pahlavian et al. [43] focused on this aspect. In this study two subject-specific geometries of the cervical spine (one of a healthy subject and one of a CM patient) were used to perform CFD simulations. CSF flow velocities were measured via 4D-MRI and used as boundary conditions in the models. For each geometry, two models were built, one neglecting nerves and denticulate ligament and one including an idealized geometry of this elements.

The simulations highlighted the impact of these structures on CSF flow in the cervical spine. They have an impact on the flow velocity patterns (Figure 18: Streamline plot for healthy case, with fine structures (left) and without (right) [43]Figure 18) with an anterior and antero-lateral dominance of CSF flow. However, the effects observed on overall flow dynamics and pressure distribution at the cervical level were limited [43].

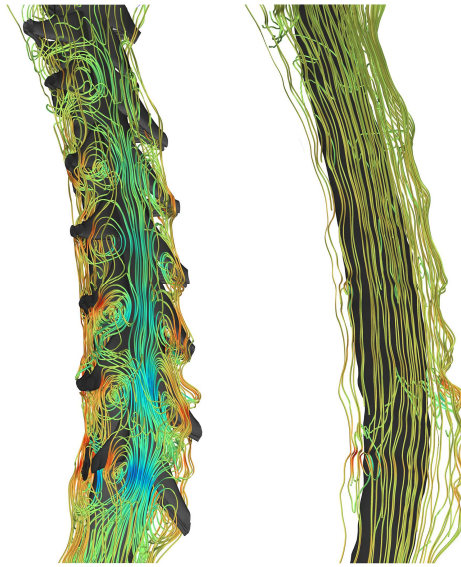


Figure 18: Streamline plot for healthy case, with fine structures (left) and without (right) [43]

CMI related syringomyelia is a complex problem involving many different factors, even considering only the mechanical one. An only-CFD approach is useful to study the conditions of CSF flow inside the SAS. But it neglects the interaction between the CSF and the spinal cord, which may play a central role in the development or reduction of the syrinx. To account for this aspect some studies were done with Fluid-Structure Interaction (FSI) models. These models allow to consider the effect of fluid movements and pressure changes on the surrounding solid structures and vice versa.

#### 4.2.2 FSI models

To account for the role of solid materials in CSF flow some studies were done with Fluid-Structure Interaction (FSI) models. These models allow to consider the effect of fluid movements and pressure changes on the surrounding solid structures and vice versa. Through the years, these models have been used mainly to study the pressure-wave propagation inside the spinal SAS [44]. Solid anatomical structures involved in the syrinx formation process (dura, pia, and spinal cord) are usually modelled as linear elastic materials, but sometimes they may also be considered viscoelastic, as in Bertam et al. [45]. Material's mechanical properties are usually taken from experimental studies led on human or animal samples, as Bilston et al. [46] or Hung et al. [47]

These FSI models show the propagation of the pressure waves but do not explain fluid flow and accumulation inside the spinal cord.

#### 4.2.3 Poroelastic models

As mentioned before, impermeable FSI models can account for the influence of solid materials on the fluid but are still considering the solids non-permeable. The first chapter (1.3 Interstitial fluid) already indicated that an important fraction of the spinal cord and

brain volume is constituted of interstitial fluid. This presence of fluid inside the spinal cord is important to consider when looking at syringomyelia development, which has been attributed to fluid (CSF or interstitial fluid) accumulation in the spinal cord. Poroelastic models allows to consider this aspect. They model a solid porous matrix and incompressible fluid flow through matrix's pores. So, it is possible to simultaneously account for the mechanical interaction between fluid and solid, the flow, and fluid accumulation inside the porous material. This hydraulic connection between SAS and spinal cord is particularly relevant when studying syrinx formation.

In a study published in 2016, Støverud et al. [44] investigated the differences between 11 linear elastic and poroelastic models. A portion of a sheep spinal cord was manually segmented from MR images, and a geometry including distinction between pia, white and grey matter. 11 different models (some depicted in Figure 19) were derived from this geometry by varying not only poroelastic or linear elastic modulization of the materials, but also other parameters related to material properties (permeability, Young's modulus) or white matter geometry. The surrounding fluid was not inserted in the model and a pressure wave was set as input at the outer surface of the geometry.

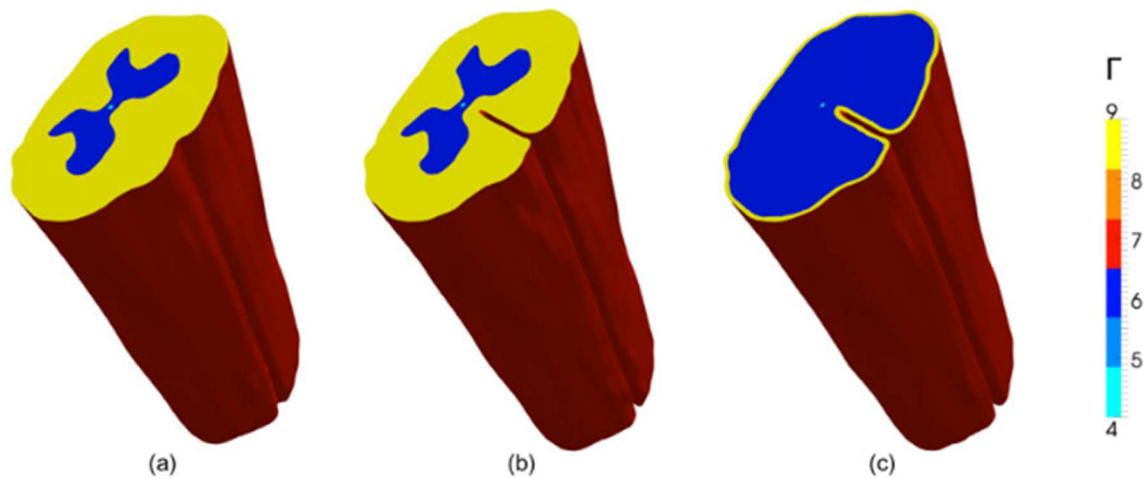


Figure 19: Picture of different geometries used [44] The color legends indicate the numbering of the boundaries; 4- central canal, 6- gray matter, 7- geometry sidewall, 9-white matter.

Comparing the results of different models, they concluded that the pia and central canal play an important role for the pressure distribution inside the cord. Pressure gradients in the cords were greater in the region close to the boundary. In terms of displacements, elastic and poroelastic models showed similar results but the models differ when the pia is considered separately from the cord. The greatest advantages of the poroelastic models are the information they can provide about the fluid movements inside the spinal cord.

A group that has been very active in the field of syringomyelia through the last decade is the group of Bertram et al. [45], [48]–[51]. They investigated syringomyelia related to subarachnoid space stenosis but their approach and results may also improve the understanding of Chiari related syringomyelia. In their last publication about this topic, Bertram et al. [48] included poroelasticity in their model, which geometry is showed in Figure

20. Their focus was on syringomyelia with adjacent subarachnoid space stenosis and thus, their model included a syrinx and a SAS stenosis aligned with it. The cord and the dura were constrained at their caudal and cranial end (Figure 20). A pressure wave with 500Pa amplitude was imposed at the cranial end of the SAS, which was the same condition used previously in their non-porous model.

Table 2: Materials properties used by Bertram et.al [48], [51].

<b>Material</b>	<b>Density [kg/m<sup>3</sup>]</b>	<b>Young modulus [MPa]</b>	<b>Poisson ratio</b>	<b>Dynamic viscosity [Pa s]</b>	<b>Permeability [m<sup>2</sup>]</b>	<b>Porosity</b>
<i>Cord</i>	1000	0.005	0.35	7e-4	e-12 / e-14	0.3
<i>Filum</i>	1000	0.0625	0.35	7e-4	e-12 / e-14	0.3
<i>Pia</i>	1000	1.25	0.35	7e-4	e-12 / e-14	0.3
<i>Dura</i>	1000	1.25	0.49	NA	NA	NA
<i>CSF</i>	1000	NA	NA	0.001	NA	NA

Bertram et al. [48] theorized that the syrinx grows due to CSF exchange with the spinal SAS. When comparing results of the model including poroelasticity with the ones of the non-porous model, they found negligible differences in the cord displacement and that the pressure peaks in the syrinx and in the SAS caudally to the stenosis were slightly increased. Moreover, they observed a certain fluid exchange between the porous tissues and the SAS, which led to a general mechanism of fluid movement between the syrinx and the SAS (Figure 21.a). The porous tissue surrounding the syrinx presented a slight swelling due to the incoming fluid. Another interesting finding of this study is that the syrinx was more likely to grow when it is positioned caudally to the stenosis, while is more likely to reduce if positioned cranially (Figure 21.b). All these changes in syrinx volume, fluid movement, and tissue swelling were evaluated in a time scale very short compared to the syrinx growth in patients [48].

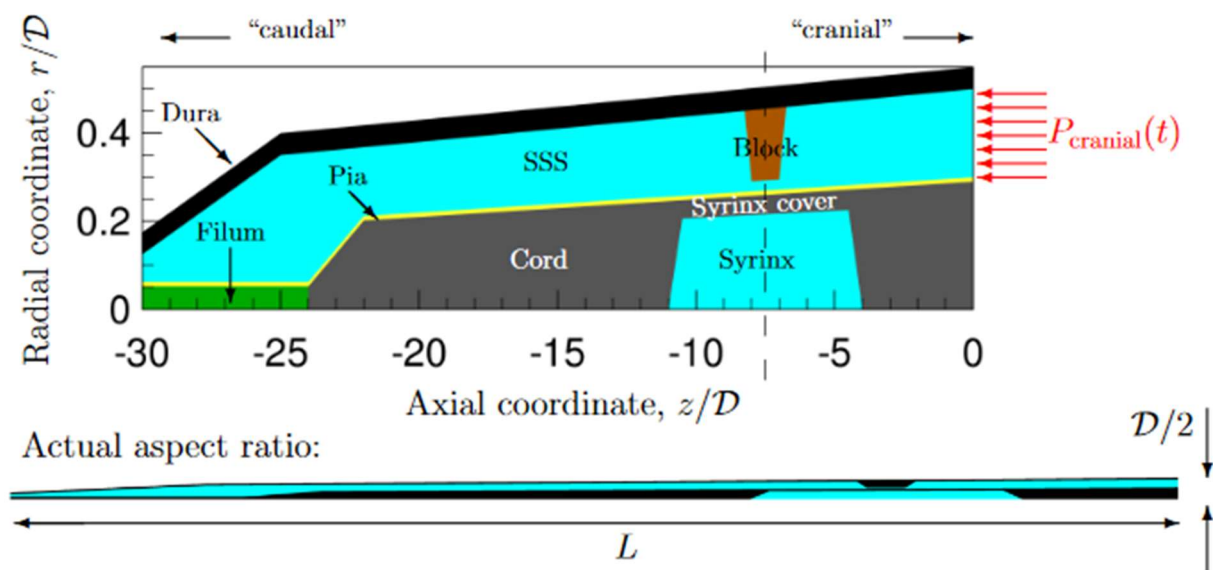


Figure 20: Sketch of the geometry of the model where  $L/D=30$  and  $D=20\text{mm}$  [51]

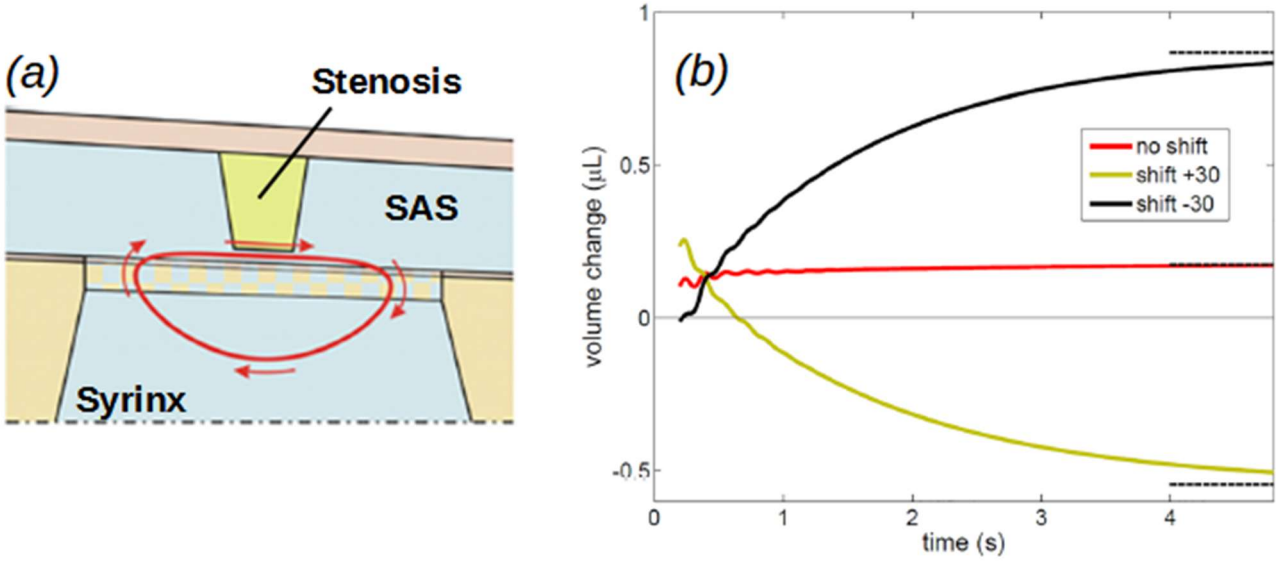


Figure 21: a) the fluid movement between SAS and syringe. b) the average changes in syringe volume over cycles for syringe aligned with stenosis (red), positioned cranially to the stenosis (gold), and caudally to the stenosis (black) [48]

## 5 Objectives

As discussed in the previous section, poroelasticity constitute an essential element in the modelling of CMI related syringomyelia. However, few studies can be found in literature considering this behavior for the syrinx development, and even less with focus on CMI related syringomyelia. So, the first objective of this work is to perform a general evaluation of the poroelastic behavior of the spinal cord (see 1.2 The spinal cord). With this knowledge, the second objective is to evaluate the influence of normal and pathological conditions on the spinal cord. With a particular focus on the effects on the fluid accumulation and exchange between the syrinx, the cord, and the SAS.

## 6 Study of Poroelastic material

First a simple study on the general poroelastic materials behavior will be led to gather information useful to evaluate results in following steps. The following evaluation will focus on material properties and their influence over the mechanical reaction of the solid under stable conditions.

### 6.1 Materials and methods

As Highlighted in previous chapters, various methods may be used to implement a computational model of CSF flow in the SAS and spinal cord. The usage of poroelastic models is crucial because it allows the investigation of fluid flow and its migration between SAS, spinal cord, and syrinx, which is a central element in the development and evolution of syringomyelia. In this work, the theory of poroelasticity is used to describe the behavior of fluids inside the spinal cord and pia mater while the flow in the SAS and syrinx is modeled according to the Navier-Stokes's equations.

#### 6.1.1 Poroelasticity theory

The classical formulation of poroelasticity relies on Biot's theory [52], [53], where the author proposes to model porous materials as linear elastic materials whose behavior can be described applying Hooke's law. Meanwhile, the fluid behavior inside the porous medium is described using Darcy's law. In Biot's theory, the coupling between these two physics is achieved by adding a term accounting for the effect of fluid pressure to Hooke's law (detailed later in this chapter). In the flow equations, no adjustment is needed because Darcy's law already accounts for the effect of solid matrix on fluid flow and pressure.

Biot's theory has been used in different studies to model the poroelastic behavior of various biological systems as bones, brain, and tumors. In his work Biot [52], [53] describes poroelasticity by the relation between three equations:

- Hooke's law
- Darcy's law
- Mass conservation

However, Darcy's law presents some limitations as it cannot account for viscous stresses and does not provide a good approximation at the fluid/solid interface [54], [55]. Brinkman's equations are a valid alternative to Darcy's law. These equations are an extension of Darcy's law and Navier-Stokes's equations allowing continuous velocity and pressure fields at the fluid/solid interface.

In this work, the COMSOL® "Free and Porous Media Flow Interface" was used to model the liquid flow. This interface uses Navier-Stokes's equations to describe flow in open regions and Brinkman's equations in porous regions [56].

*Equations for fluid description*

In COMSOL Multiphysics® the fluid flow is described by the Navier-Stokes's equations as follows:

$$\rho \frac{\partial \vec{v}}{\partial t} + \rho(\vec{v} \cdot \nabla)\vec{v} = \nabla \cdot [-\vec{P}\mathbf{I} + \mu(\nabla\vec{v} + (\nabla\vec{v})^T)] + \vec{F} \quad (6.1)$$

Hereby is  $\vec{v}$  is the velocity,  $\vec{P}$  the pressure,  $\rho$  is the density, and  $\mu$  the dynamic viscosity of the fluid.  $\vec{F}$  represents the contribution of the volume forces, and  $\mathbf{I}$  is the identity matrix. When Reynold's numbers are low, the convective term can be neglected leading to a Stokes flow. Therefore, the equation 6.1 can be reduced to:

$$\rho \frac{\partial \vec{v}}{\partial t} = \nabla \cdot [-\vec{P}\mathbf{I} + \mu(\nabla\vec{v} + (\nabla\vec{v})^T)] + \vec{F} \quad (6.2)$$

From Navier-Stokes's equations, Darcy's law can be derived by considering the effect of the porous material permeability on the fluid flow and pressure [57]. Hence the general form of Darcy's law for fluid flow inside a porous medium is the following:

$$\vec{v}_d = -\frac{k}{\mu} \nabla \cdot \vec{P} \quad (6.3)$$

In this equation is  $\vec{v}_d$  is the fluid velocity inside porous medium (Darcy's velocity),  $k$  the material's permeability,  $\mu$  the viscosity of the fluid, and  $\nabla \cdot \vec{P}$  the divergence of fluid's pressure [57].

As already mentioned, Brinkman's equations can be obtained from Navier-Stokes's equations and Darcy's law. To accomplish this the following assumptions, need to be taken [57]: include the effect of viscous shear stress in Darcy's law, add the porosity factor, and neglect the inertial term of Navier-Stokes's equation. Thus, the formulation of Brinkman's equation used in COMSOL Multiphysics® is the following [56]:

$$\begin{aligned} \frac{\rho}{\epsilon_p} \frac{\partial \vec{v}_d}{\partial t} = \nabla \cdot \left[ -\vec{P}\mathbf{I} + \frac{\mu}{\epsilon_p} (\nabla\vec{v}_d + (\nabla\vec{v}_d)^T) - \frac{2\mu}{3\epsilon_p} (\nabla \cdot \vec{v}_d)\mathbf{I} \right] + \\ - \left( \frac{\mu}{k} + \beta_f |\vec{v}_d| + \frac{Q_m}{\epsilon_p^2} \right) \vec{v}_d + \vec{F} \end{aligned} \quad (6.4)$$

In equation 6.4 a mass source term  $Q_m$  is added to the Darcy's equation to account for mass deposit in the porous domain [56] along with a Forcheimer drag coefficient  $\beta_f$ .  $\epsilon_p$  is the porosity of the material and  $k$  the permeability, both derived from the coefficients used in

Darcy's law. A viscosity term (Equation 6.4.1) is also included to account for the compressibility of the fluid.

$$-\frac{2\mu}{3\epsilon_p} (\nabla \cdot \vec{v}_d) \mathbf{I} \quad (6.4.1)$$

In the studied situation two fluids are presents, namely the CSF and the ISF. As both can be considered incompressible the viscosity term expressed in equation 6.4.1 is equal to zero. This led to the following reduced formulation of equation 6.4.

$$\frac{\rho}{\epsilon_p} \frac{\partial \vec{v}_d}{\partial t} = \nabla \cdot \left[ -\vec{P} \mathbf{I} + \frac{\mu}{\epsilon_p} (\nabla \vec{v}_d + (\nabla \vec{v}_d)^T) \right] - \left( \frac{\mu}{k} + \beta_f |\vec{v}_d| + \frac{Q_m}{\epsilon_p^2} \right) \vec{v}_d + \vec{F} \quad (6.5)$$

#### Equations for solid description

Looking at the solid material model we can consider a cube of porous material filled with fluid in a Cartesian coordinates system (x, y, z). The cube can be subject to normal and tangential stresses (Figure 22). The relation between stresses and deformations is described for a linear elastic and isotropic material by Hooke's law.

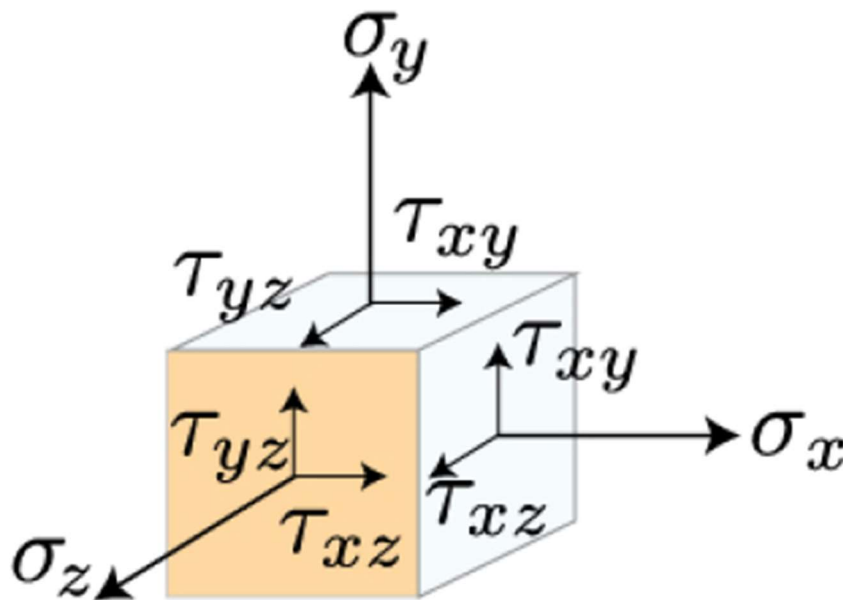


Figure 22: Stresses in a cubic solid element in a 3D Cartesian system. From Silvera [55]

To consider poroelasticity a term accounting for the contribution of fluid pressure was added [52]. Moreover, Biot [52] assumed the shear stresses in the matrix to be zero reducing Hooke's law to the following equations:

$$e_x = \frac{1}{E} \left( \sigma_x - \nu(\sigma_y + \sigma_z) \right) + \frac{P_x}{3H} \quad (6.6)$$

$$e_y = \frac{1}{E} \left( \sigma_y - \nu(\sigma_x + \sigma_z) \right) + \frac{P_y}{3H} \quad (6.7)$$

$$e_z = \frac{1}{E} \left( \sigma_z - \nu(\sigma_y + \sigma_x) \right) + \frac{P_z}{3H} \quad (6.8)$$

$$\gamma_{xy} = \frac{\tau_{xy}}{G}; \gamma_{yz} = \frac{\tau_{yz}}{G}; \gamma_{xz} = \frac{\tau_{xz}}{G} \quad (6.9)$$

Where  $E$ ,  $\nu$ , and  $G$  are respectively Young's modulus, the Poisson ratio, and the shear modulus.  $P$  is the fluid pressure,  $H$  is a constant accounting for block's compressibility.  $\sigma_i$  and  $\tau_{ij}$  are the normal and shear stresses in the three orthogonal directions. Meanwhile,  $e_i$  and  $\gamma_{ij}$  are the components of the strain field. The displacement field and strains are related by the following equations:

$$e_x = \frac{\partial u}{\partial x}; e_y = \frac{\partial v}{\partial y}; e_z = \frac{\partial w}{\partial z} \quad (6.10)$$

In previous equations, there are four unknown parameters: the fluid pressure  $P$ , and the displacement components along the three directions ( $u, v, w$ ). The fourth equation necessary to solve the problem is mass conservation.

$$\frac{\partial \Theta}{\partial t} = - \left( \frac{\partial v_x}{\partial x} + \frac{\partial v_y}{\partial y} + \frac{\partial v_z}{\partial z} \right) \quad (6.11)$$

In the equation above is  $\Theta$  the increment in time of the water content. From equations 6.3, 6.6, 6.7, 6.8 and 6.11, the following four equations describing poroelastic behavior can be derived [52].

$$k \nabla^2 P = \alpha \frac{\partial \vec{\varepsilon}}{\partial t} + \frac{1}{Q} \frac{\partial \vec{P}}{\partial t} \quad (6.12)$$

$$G \nabla^2 u + \frac{G}{1-2\nu} \frac{\partial \vec{\varepsilon}}{\partial x} - \frac{\partial \vec{P}}{\partial x} = 0 \quad (6.13)$$

$$G \nabla^2 v + \frac{G}{1-2\nu} \frac{\partial \vec{\varepsilon}}{\partial y} - \frac{\partial \vec{P}}{\partial y} = 0 \quad (6.14)$$

$$G \nabla^2 w + \frac{G}{1-2\nu} \frac{\partial \vec{\varepsilon}}{\partial z} - \frac{\partial \vec{P}}{\partial z} = 0 \quad (6.15)$$

$Q$  is the quantity of fluid that can be forced into the porous material while the porous medium volume is constant and the Biot coefficient  $\alpha$  is defined as:

$$\alpha = \frac{2(1 + \nu)G}{3(1 - 2\nu)H} \quad (6.16)$$

In the studied situation, it is possible to assume that no air is present inside the fluid phase. This assumption led to consider  $Q = \infty$  and  $\alpha = 1$ . Therefore, the equation 6.12 can be reduced and expressed as a function of the velocity field leading to:

$$\rho \nabla \vec{v}_d = \rho \frac{\partial \vec{\epsilon}}{\partial t} \quad (6.17)$$

The conservation of the fluid mass is affected by its interaction with the solid. Effects on the fluid pressure can be produced by the deformation of the solid. To couple the solid and the fluid physics a two-way coupling system is necessary. The effect of the solid deformation on the fluid mass conservation is expressed in equation 6.17. Vice-versa the influence of the fluid pressure gradient on the solid is present in the equations governing the mechanical movement of the solid (eq. 6.13, 6.14, 6.15).

#### *COMSOL® implementation of poroelasticity*

To recreate the poroelasticity theory in COMSOL® Multiphysics, two coupling terms considering the effect of the solid mechanics on the fluid and vice versa are included. In Brinkman's equation (6.5) a mass source term  $Q_m$  is added, defined as follows:

$$Q_m = -\rho \cdot \frac{\partial \vec{\epsilon}}{\partial t} = -\rho \cdot \frac{\partial}{\partial t} \left( \frac{\partial u}{\partial x} + \frac{\partial v}{\partial y} + \frac{\partial w}{\partial z} \right) \quad (6.18)$$

This term considers the volume changes of the porous matrix. When the porous matrix expands, the volume available for the fluid will increase and lead to an inflow of fluid inside the medium. For this reason, the sign in equation 6.18 is reversed [55]. The effect of fluid over the solid material is integrated into the solid mechanics physics with three volume forces corresponding with the fluid pressure components acting along the three principal directions:

$$F_{vx} = -\frac{\partial \vec{P}}{\partial x}; F_{vy} = -\frac{\partial \vec{P}}{\partial y}; F_{vz} = -\frac{\partial \vec{P}}{\partial z}; \quad (6.19)$$

### 6.1.2 Geometry and boundary conditions

The goal of this first study was to evaluate the influence of different properties on the mechanical behavior of a poroelastic material. Therefore, a 2D model was built. The geometry was chosen to be qualitatively similar to the clinical condition, with a porous material dividing two fluid compartments. It was composed of three rectangles with the same dimensions (1 cm x 5 cm) posed one on top of the other, as depicted in Figure 23.

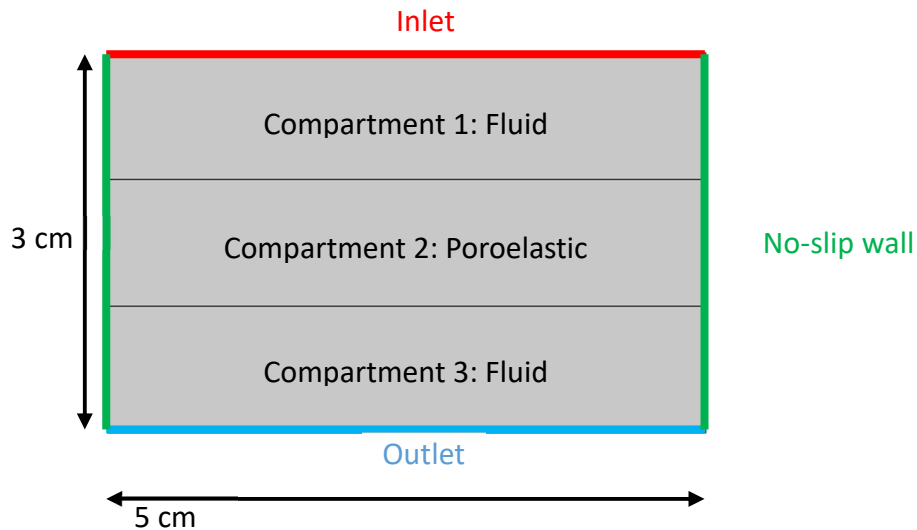


Figure 23: Geometry of the model

The model was implemented in COMSOL® Multiphysics using the following modules:

- Free and Porous Media Flow
- Solid Mechanics

As previously mentioned in section 6.1.1, these modules were coupled using a mass source term (acting on the fluid) and a body force term (acting on the solid) as done by Silvera [55]. The mesh was built using the automatic tool implemented in COMSOL® Multiphysics setting the element size to “Fine”. This tool automatically set the mesh settings based on the geometry and physics involved in the simulation. The final mesh (Figure 24) consisted of 2750 domain and 252 boundary elements. The average element quality (skewness rated from 0 to 1 where 1 is the perfect mesh) was 0.8736 and the dimensions ranged from  $5.7E-4 \text{ m}^2$  to  $19E-4 \text{ m}^2$ .

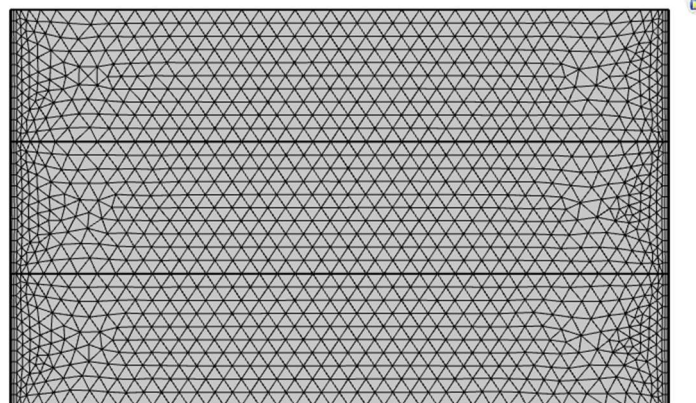


Figure 24: Mesh used in the poroelastic material study.

Both the CSF and the ISF are usually considered to have properties similar to the ones of water. Thus, water properties present in the COMSOL® Multiphysics materials library were used to model the fluid (considered fluid temperature was 20°C). The poroelastic material was the focus of the study and therefore his properties were changed during the experiment. The base for the poroelastic material properties was the isotropic model of cord presented in Heil et al. [51] resumed in Table 2. Effects of changes of porosity, permeability, Young’s modulus, and Poisson’s ratio were investigated while density and dynamic viscosity were kept fixed. For each of these parameters a range of values (showed by Table 4) was considered. While investigating the effect of one material’s property, all the others were kept constant to the values of baseline material shown in Table 3.

Table 3: Baseline material properties.

<b>Density [kg/m<sup>3</sup>]</b>	<b>Young modulus [MPa]</b>	<b>Poisson ratio</b>	<b>Dynamic viscosity [Pa s]</b>	<b>Permeability [m<sup>2</sup>]</b>	<b>Porosity</b>
1000	0.005	0.35	7e-4	e-14	0.3

Table 4: Range of values considered in the study for each parameter

<b>Parameter</b>	<b>Range</b>
<b>Density [kg/m<sup>3</sup>]</b>	1000
<b>Young’s modulus [MPa]</b>	0.004 – 1.25
<b>Poisson’s ratio</b>	0.2 – 0.4
<b>Dynamic viscosity [Pa s]</b>	7E-4
<b>Permeability [ m<sup>2</sup>]</b>	8E-15 – 1E-13
<b>Porosity</b>	0.2 – 0.4

Beside this evaluation, the effect of the geometrical properties of the model were investigated. Three different widths were considered (3cm, 4cm, 5cm) and the ratio between height and width of each block was varied between 0.4 and 0.1.

The boundary conditions were arbitrary chosen to induce a fluid flow between the two fluid compartments through the poroelastic medium. A normal velocity of 6E-8 m/s (entering the domain) was imposed at the inlet, while a 0Pa pressure outlet was imposed at the bottom, as depicted by schematic in Figure 25.

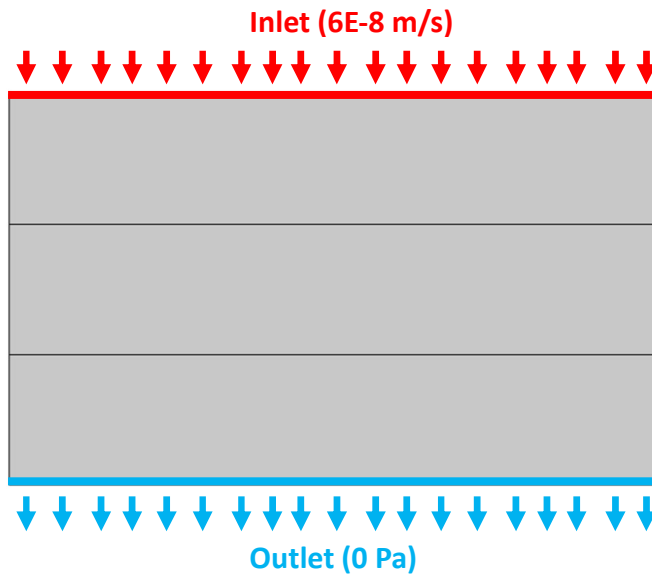


Figure 25: schematic of the applied boundary conditions.

The study was performed using stationary simulations. However, some time-dependent simulations were run for comparison purposes. For time-dependent simulations the inlet was ramped up using the step function depicted by Figure 26. Each run simulated at least 2s in order to have a relatively long plateau phase (from 0.25s to 2s).

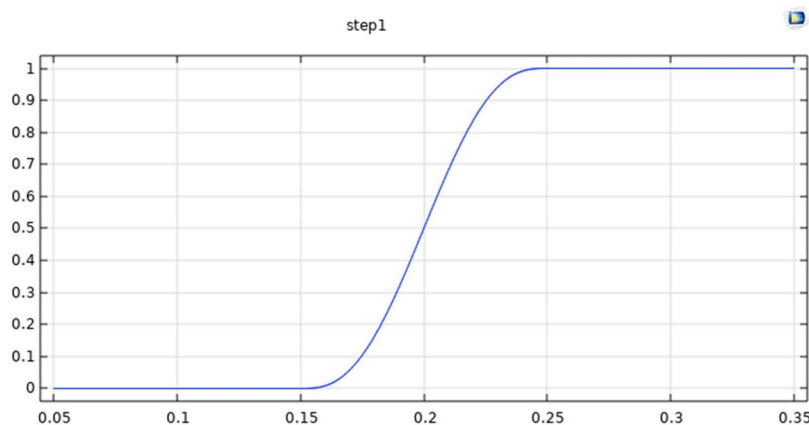


Figure 26: Step function used to ramp up the inlet in time-dependent simulations.

## 6.2 Results

In the following chapter, the results of the previously described model will be presented. The objective of this first study is to gather information regarding the behavior of a poroelastic material when a fluid flow is imposed through it. This information will be useful to, subsequently, evaluate the results of the second model. Seen the goal of this first model the focus will be on the qualitative behavior of the material rather than on the quantitative response to the imposed conditions.

### 6.2.1 Steady simulations

The chosen boundary conditions were first applied to a model where the poroelastic material properties were as depicted in Table 3.

As can be seen in Figure 28, the imposed boundaries induced a fluid flux between compartments 1 and 3 through compartment 2 (see Figure 23). The pressure difference between the two fluid compartments (1, 3) was 60 Pa (Figure 27), while the velocity of the fluid through the poroelastic material was the same imposed at the inlet ( $6 \times 10^{-8}$  m/s). The poroelastic material was bent by the effect of the pressure and presented an inflection of 2.91 mm (evaluated in the medium point of compartment 2 lower bound) and a swelling of  $0.006 \text{ cm}^2$  corresponding to a 0.12% increase in area.

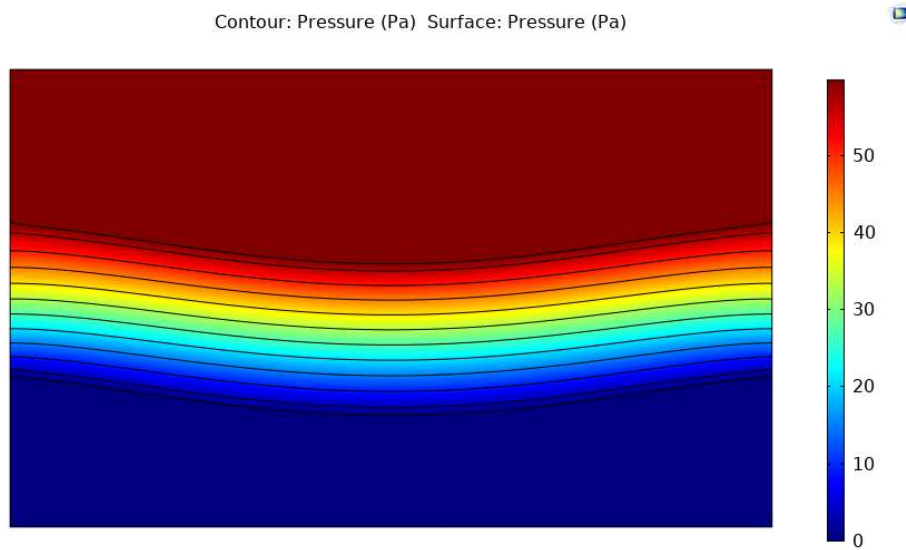


Figure 27: Pressure field in model with baseline material properties.

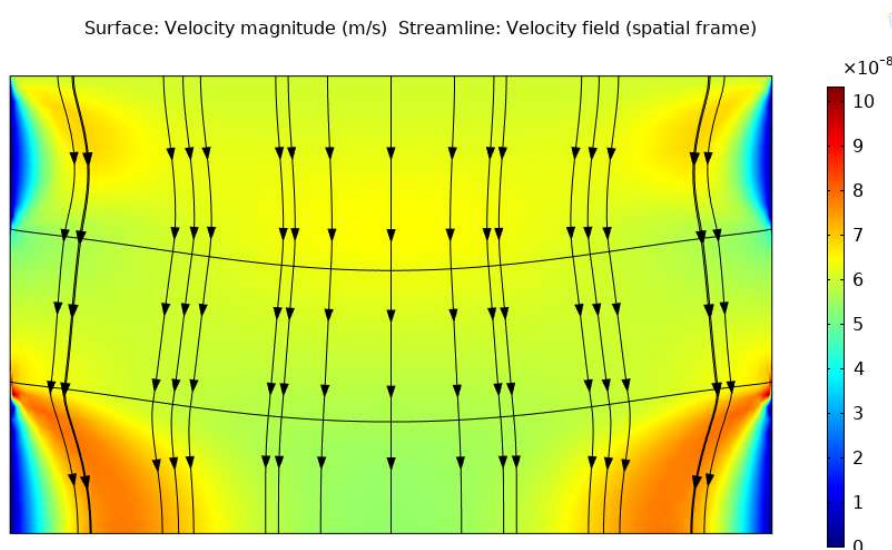


Figure 28: Velocity field and streamlines in model with baseline material properties.

Throughout all the simulations with different material properties, the pattern of pressure and velocity fields was preserved even though sometimes with different absolute values.

All the chosen parameters (permeability, Young’s modulus, Poisson’s ratio, and width/height ratio) gave an effect in terms of inflection and swelling. Thus, to evaluate the influence of each parameter, the percentual swelling was chosen. It was calculated from the absolute area increase in Microsoft Excel® using the following formula:

$$S_{\%} = \frac{A_f - A_i}{A_i}$$

Where  $S_{\%}$  is the percentual swelling,  $A_i$  is the initial area, and  $A_f$  is the final area.

Permeability was the only parameter that influenced both the swelling of the material and the pressure difference between the two fluid compartments. As highlighted by the graph in Figure 29, the percentual swelling decrease with the increased permeability. In the observed range of values, the relation between swelling and permeability corresponds to a decreasing exponential as well as for the pressure.

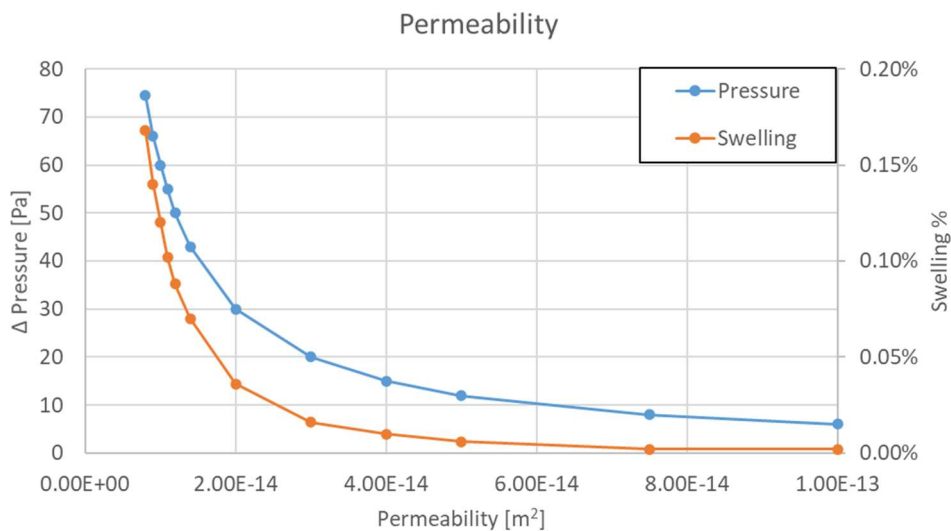


Figure 29: Impact of different permeability values on percentual swelling and pressure difference between the fluid compartments.

Young’s modulus only influenced the swelling and did not affect the pressure difference. The relationship between its magnitude and the percentual swelling was exponentially decreasing too, reaching values lower than 0.001% already at 0.0625 MPa, as depicted in Figure 30.

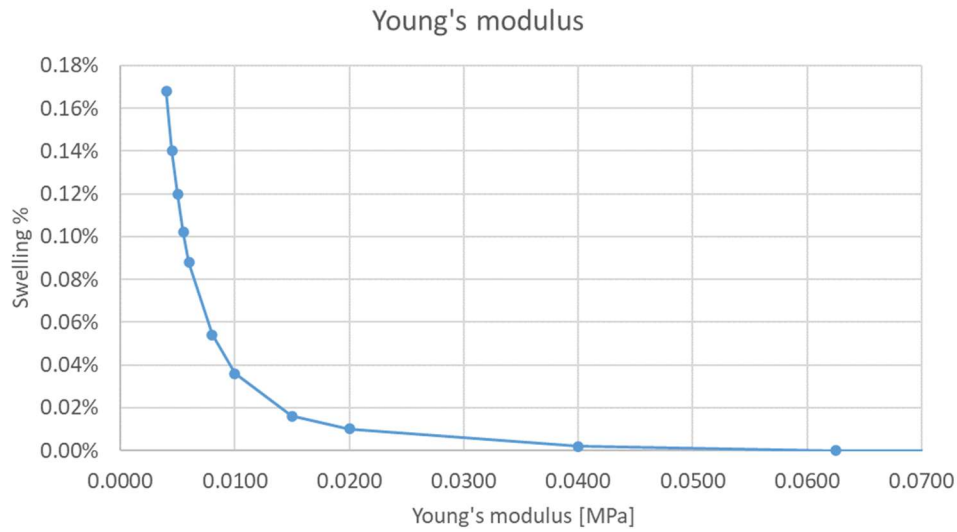


Figure 30: Plot of Young's modulus effect on percentual swelling.

Poisson's ratio was linearly related to the percentual swelling, as depicted in Figure 31. For values above 0.4, the swelling had negative values. That means that the poroelastic material was shrinking and fluid was pushed out of the domain.

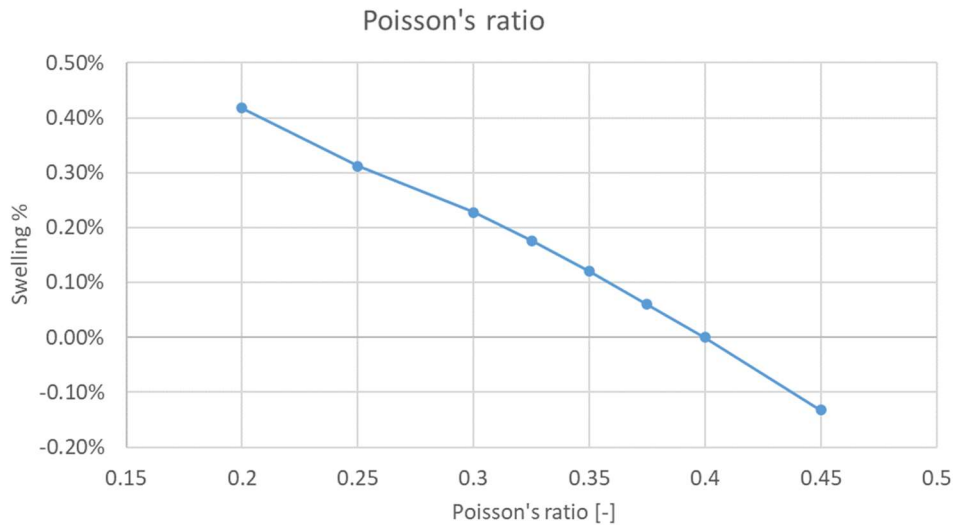


Figure 31: Plot of Poisson's ratio effect on percentual swelling.

The geometry of the domain itself showed to influence both the pressure difference between the fluid compartments and the percentual swelling (Figure 32, 33). The pressure difference appears to be related to the height-width ratio by a linear relation, whose slope seems to depend on the chosen width (Figure 33). The percentual swelling decreases exponentially with the increasing height-width ratio. In this case, when the ratio value exceeds 0.3, the poroelastic material is compressed (negative swelling, see Figure 32).

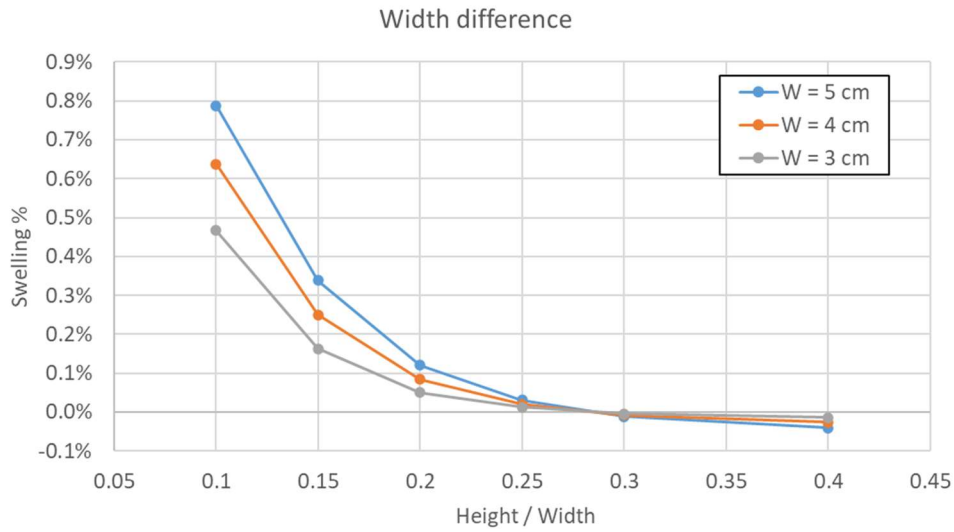


Figure 32: Plot of height-width ratio effect on percentual swelling.

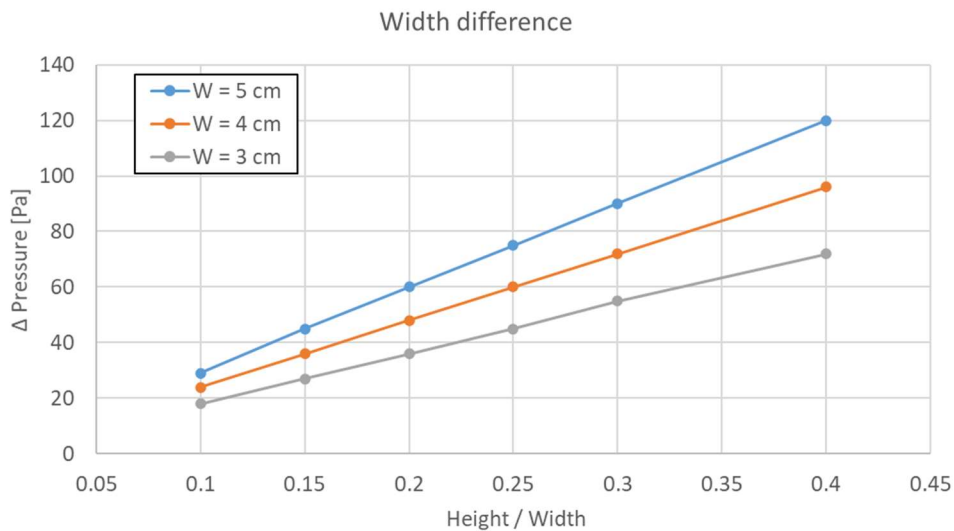


Figure 33: Plot of height-width ratio effect on pressure difference.

### 6.2.2 Time-dependent simulations

As previously explained in section 6.1.2, the boundary conditions used for time-dependent simulations were the same as the steady ones except for the inlet. Which was ramped up to the same value (6E-8 m/s) using a step function, showed in Figure 26. The first time-dependent simulations gave unexpected results. The poroelastic material bent in the opposite direction with respect to what it did in the steady simulations. However, this behavior was consistent with the obtained pressure field, which showed a particular pressure pattern inside the poroelastic medium, characterized by three high and three low-pressure zones distributed in a checkboard pattern (Figure 34).

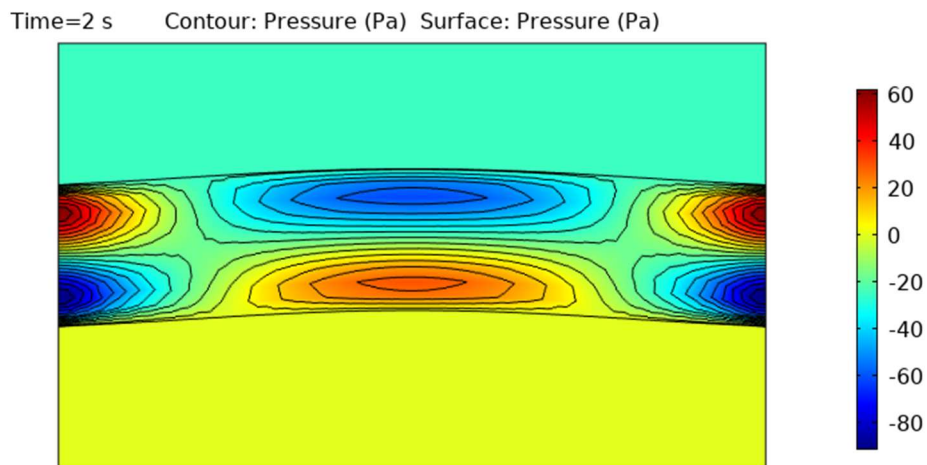


Figure 34: Pressure field in time-dependent simulation with baseline material properties.

Furthermore, the fluid was not flowing through the poroelastic medium, and the flux through the outlet showed fluid entering the mode through this boundary rather than exiting. This behavior was observed in several models with different permeability values of the poroelastic medium ( $e-12 \text{ m}^2$ ,  $e-13 \text{ m}^2$ ,  $e-14 \text{ m}^2$ ). The models in which higher values of permeability ( $e-11 \text{ m}^2$ ,  $e-10 \text{ m}^2$ ) were used showed an opposite behavior, perfectly matching the one expected from the steady simulations.

The behavior of the models with the lowest permeability was probably due to simulation errors, finally resulting in a wrong solution even though convergence was always reached. To solve this issue, the mesh was modified, adding boundary layers at the interfaces between the fluid and the porous medium. The final mesh is showed in Figure 35.

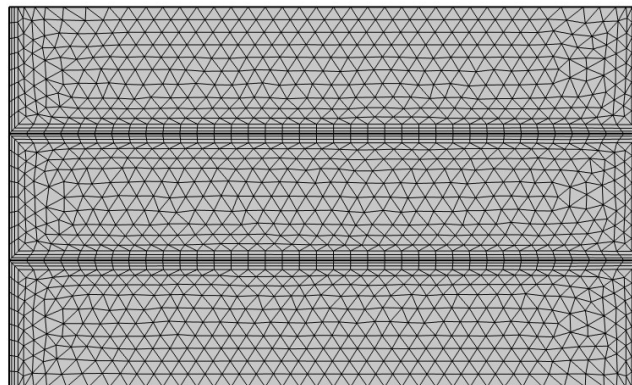


Figure 35: Final mesh used for time dependent simulations.

With the new mesh, the time-dependent models gave the expected result behaving like the steady ones.

Time-dependent simulations showed a transient of variable duration (up to some minutes) where a checkboard pressure pattern can be observed (Figure 36). Unlike the one previously obtained (showed in Figure 34), this time high and low-pressure zones were inverted.

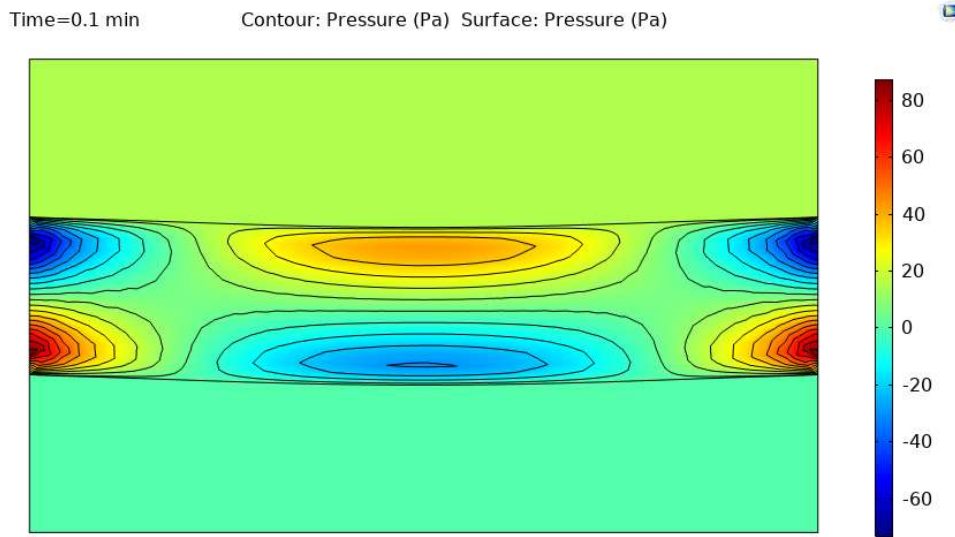


Figure 36: Pressure field in time-dependent simulation with baseline material properties and new mesh.

In the first 0.25 seconds of the transient simulation, the flow inside the model is gradually increased and recirculation inside domain 1 can be observed. Thus, during this first transient period, proper fluid flux through the poroelastic medium is not present. Only after a certain period (varying with the permeability from 0.01s for permeability of  $e-11 \text{ m}^2$  to 5 minutes for  $e-14 \text{ m}^2$ ), fluid flow is established across the poroelastic medium, and the model behaves as the steady one (as can be observed in Figure 38). This first transient period also affects the area of the poroelastic material. As can be seen in Figure 37, the area first decreases, meaning that the poroelastic material is compressed, and only after a certain period it starts to swell

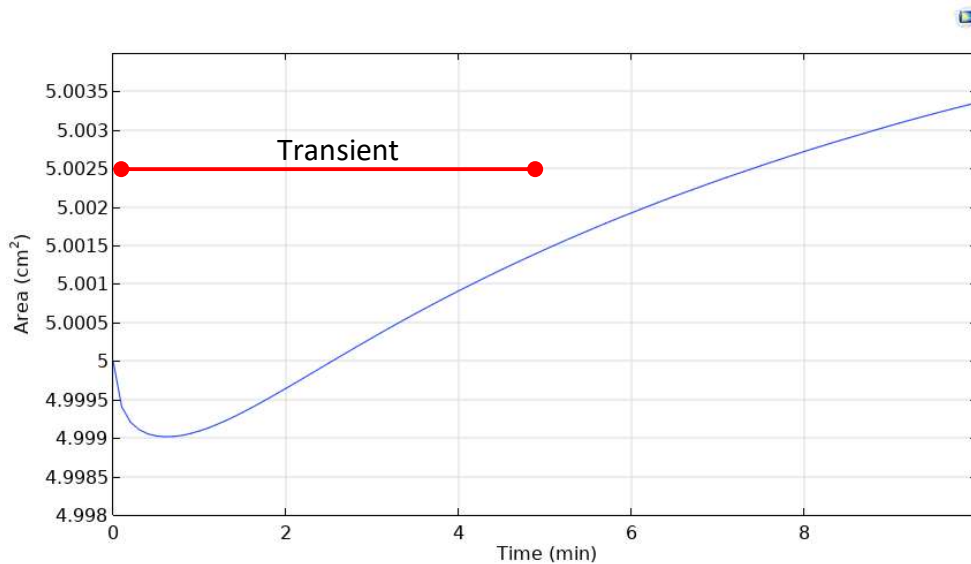


Figure 37: Area of poroelastic medium over time.

The amount of time needed for the fluid flow to establish through the material showed to be dependent on the permeability of the poroelastic medium, increasing with the decreasing permeability. For the baseline material properties, this amount of time can be evaluated around 5 minutes.

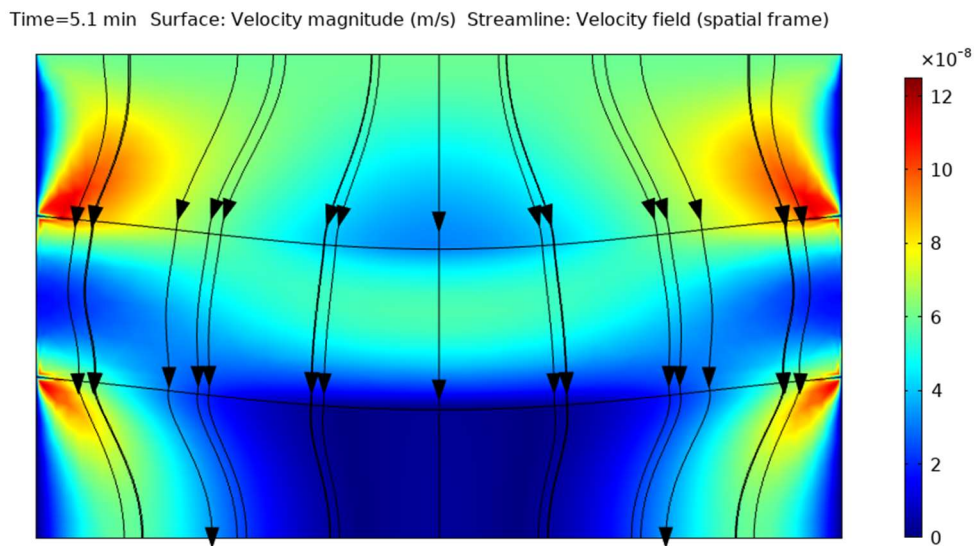


Figure 38: Velocity field and streamlines in time-dependent model with baseline material properties at the end of the transient.

### 6.3 Discussion

Even though poroelasticity plays a central role in modeling multiple physiological tissues, only a few studies can be found focusing on the poroelasticity itself. The findings described in the previous section are therefore useful to have a general idea of the phenomenon in the physiological conditions.

The pressure pattern (Figure 27) shows clearly that when a fluid is flowing through the poroelastic material the change in pressure is located in the material itself. Coupling it with the velocity field (Figure 28) is possible to state that for a permeability value of  $1e-13 \text{ m}^2$ , a 60Pa pressure difference across the material corresponds to a fluid flowing through it at roughly  $6e-8 \text{ m/s}$ .

The effect of material properties indicates that an increase in the material stiffness and rigidity (Young's modulus and Poisson's ratio) is associated with a decrease in the swelling. This is because these two parameters do not affect the velocity of fluid flow through the poroelastic domain or the pressure distribution, but only the mechanical response of the material to the forces generated by fluid flow. Consequently, the forces applied to the solid material do not change, while an increase in rigidity results in a decrease in the swelling and bending of the material.

The effect of the height-width ratio also falls under this mechanism. A bigger ratio, meaning a thicker block of material, causes a reduction in the swelling and an increase in the pressure difference needed to force the fluid through the domain. This change in pressure is not observed for stiffness and rigidity. The permeability impacts the degree of swelling because it increases or decreases the resistance to the fluid passage changing the ability of the material to hold part of the fluid. Additionally, it influences the pressure difference because the force needed to drive the same flow across the material differs with permeability. As observed in

Figure 29 both swelling and pressure difference decrease with the increased permeability, meaning that a material with a higher permeability is less capable to hold back fluid but, at the same time, a lower force is needed to push the fluid through it.

In conclusion the steady models highlighted that, Young's modulus, Poisson's ratio, and height-width ratio do not affect the solid opposition of the material to the fluid flow, rather they affect the ability of the solid to hold fluid and its reaction to the subsequently generated forces. The permeability rather affects the effect of the poroelastic material on the fluid flow.

Time-dependent simulations highlighted the presence of a transient period at the beginning of the simulation. The time needed for the fluid flow to be established across the poroelastic material depends on the permeability value (as mentioned in section 6.2.2). The presence of this transient period suggests that in the next model (chapter 7), where the inlet condition will be sinusoidal, the continuous change of the pressure condition may not allow the establishment of a proper fluid flow across the poroelastic spinal cord.

Some relevant computational issues that will need attention during the building phase of the next model were also highlighted. The main understanding is that, when starting from zero-field conditions, the model can give wrong results showing a behavior opposite to the expected one. This issue is always solved by the introduction of a boundary layer of mesh elements at the interface between fluid compartments and any poroelastic material.

In conclusion, mainly two findings came out of the transient simulations. First, the time needed for the fluid to start flowing through the poroelastic material may be too long to allow the observation of a proper flow across the spinal cord in the next model. Second, attention is necessary when meshing the geometry and a boundary layer must be included to avoid incorrect results.

## 7 Spinal cord models

The findings from the previous study were used to build a poroelastic model of the spinal cord. This model would allow to evaluate the behavior of the spinal cord under different conditions. Simplified geometry of the spinal cord and SAS of a patient presenting syringomyelia was built and the effects of different permeability, geometry, and boundary conditions were evaluated.

### 7.1 Materials and method

In these models, the poroelasticity theory was used to describe the fluid behavior inside the poroelastic materials (pia, filum, and spinal cord), while Navier-Stokes's equations were used to describe the flow in the SAS and syrinx. The poroelasticity theory and the approach used to model the physics was already treated in chapter 6.1.1 and will not be repeated here.

#### 7.1.1 Geometry and boundary conditions

In order to get a wide evaluation of the effect of different parameters, three different setups were used to carry out this second study.

##### *Geometry for setup 1-2*

Based on the geometry of Bertram et al. [45] a baseline 2D axisymmetric model was built. It had a total length of 600mm and an external radius that gradually decreases from 11mm (at the cranial end) to 3.5mm (at the rostral end). The geometry consists of 4 axisymmetric layers being (from the symmetry axis) the spinal cord, the pia, the SAS, and the dura (Figure 39). In the lowest section the spinal cord ends, and its place is taken by the filum. The spinal cord has a radius of 5.8mm at the top of the geometry and is covered by a layer of pia 0.2mm thick. The SAS has a thickness of 4mm constant throughout all the geometry except for the lower section and is limited by a dura layer of 1mm. Inside the spinal cord, a syrinx was placed, with the same dimensions as the one used by Kumbhar [58]. Having a 20% cavitation concerning the diameter of the spinal cord, a total length of 70mm, and an initial volume of 1.149ml. The spinal cord, the pia, and the filum are modeled as poroelastic materials, while the dura is modeled as impermeable linear elastic material, consistently with Bertram et al. [45]. No block or restriction of the SAS was implemented; therefore, the modeled situation can be linked to the one of a patient who already underwent a PFD surgery. The Foramen Magnum is the only opening of the model, acting as both inlet and outlet. The cord, the pia, and the dura were constrained at the top and at the bottom edges of the geometry (green lines in Figure 39). The model is allowed to expand only in the external direction (the dura can move towards the outside) while it cannot cross the symmetry axis.

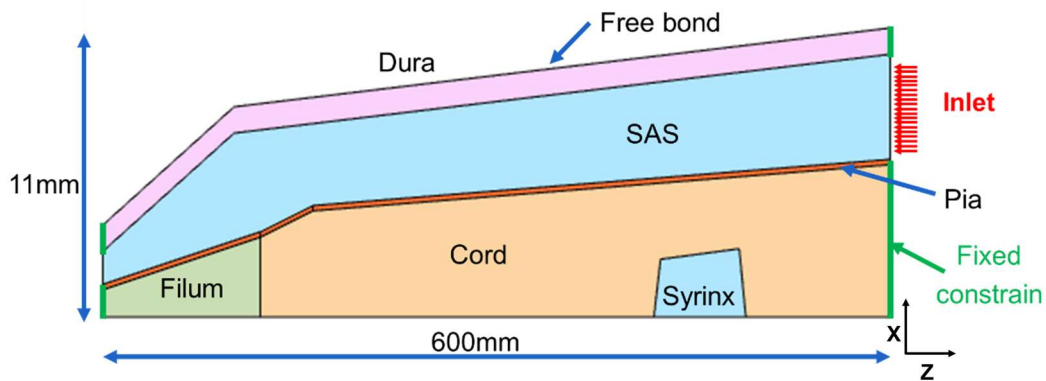


Figure 39: Scheme of Geometry 1. Please notice the x axis is scaled by a factor of 20.

Different setups were prepared to evaluate different aspects, every simulation was run for a minimum of 4.8s corresponding to either 6 or 12 cycles depending on the inlet wave frequency. The time step size was set to “free” this allows the solver to arbitrarily change the dimension of each time step. However, the maximum dimension of one time step was set to 0.01s.

To solve the model a fully coupled solver already implemented in COMSOL® was used. The nonlinear method used by the solver was set to “Automatic (Newton)”, while the minimum damping factor was dropped to 1e-12 and the maximum number of iterations was limited to 50.

### Setup 1

The objective of this first setup was to evaluate the effect of different permeability values on the model behavior. In Geometry 1 the material properties were as in Bertram et al.[48] (resumed in Table 5). Five different values of permeability were given to the poroelastic materials, ranging from e-11 to e-15.

Table 5: Material properties used in setup 1, derived from Bertram et al.[48].

<b>Material</b>	<b>Density [kg/m<sup>3</sup>]</b>	<b>Young modulus [MPa]</b>	<b>Poisson ratio</b>	<b>Dynamic viscosity [Pa s]</b>	<b>Permeability [m<sup>2</sup>]</b>	<b>Porosity</b>
<i>Cord</i>	1000	0.005	0.35	7e-4	e-11 / e-15	0.3
<i>Filum</i>	1000	0.0625	0.35	7e-4	e-11 / e-15	0.3
<i>Pia</i>	1000	1.25	0.35	7e-4	e-11 / e-15	0.3
<i>Dura</i>	1000	1.25	0.49	NA	NA	NA
<i>CSF</i>	1000	NA	NA	0.001	NA	NA

In this setup, the same inlet condition applied by Bertram et al. [48] was used. It consists of a sinusoidal pressure wave with an amplitude of 1000Pa and a frequency of 2.5Hz. Bertram et al. [48] used both the waveform with 0Pa mean and the one with 500Pa average. It was decided to use the wave with 500Pa average (depicted in Figure 40), as it was noticed during preliminary evaluations that an inlet condition crossing the 0 value could sometimes cause computational issues.

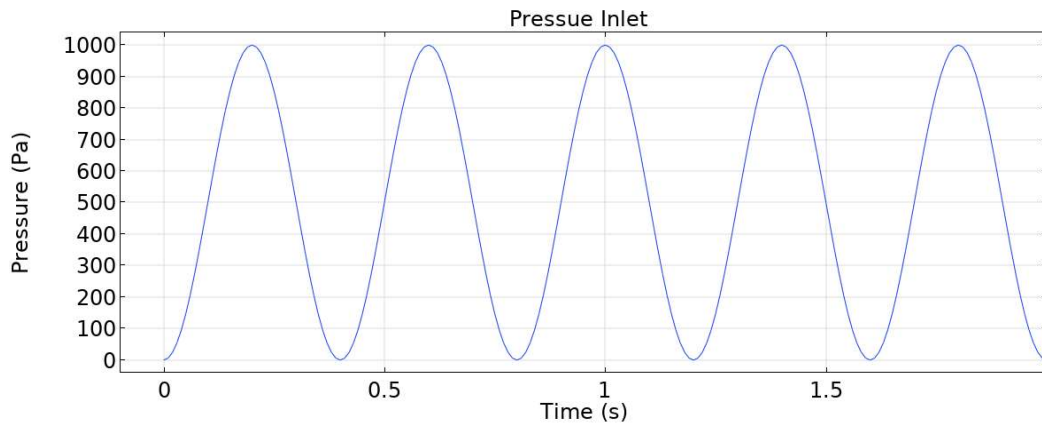


Figure 40: Pressure inlet used in setup 1.

### Setup 2

The second setup was used to evaluate the effect of different inlet conditions corresponding to different physiological behaviors. The same geometry of setup 1 was used and the only change in material properties was the permeability value fixed at  $1e-13 \text{ m}^2$ , as in the following table.

Table 6: Material properties used in setup 2, derived from Bertram et al. [48]

<b>Material</b>	<b>Density [kg/m<sup>3</sup>]</b>	<b>Young modulus [MPa]</b>	<b>Poisson ratio</b>	<b>Dynamic viscosity [Pa s]</b>	<b>Permeability [m<sup>2</sup>]</b>	<b>Porosity</b>
<i>Cord</i>	1000	0.005	0.35	7e-4	e-13	0.3
<i>Filum</i>	1000	0.0625	0.35	7e-4	e-13	0.3
<i>Pia</i>	1000	1.25	0.35	7e-4	e-13	0.3
<i>Dura</i>	1000	1.25	0.49	NA	NA	NA
<i>CSF</i>	1000	NA	NA	0.001	NA	NA

Three different boundary conditions were applied to the described model. First (A), the same was used in setup 1, directly taken from Bertram et al. [48]. A pressure inlet shaped with a sinusoidal wave of 1000Pa amplitude, 500Pa average, and frequency of 2.5Hz (Figure 41).

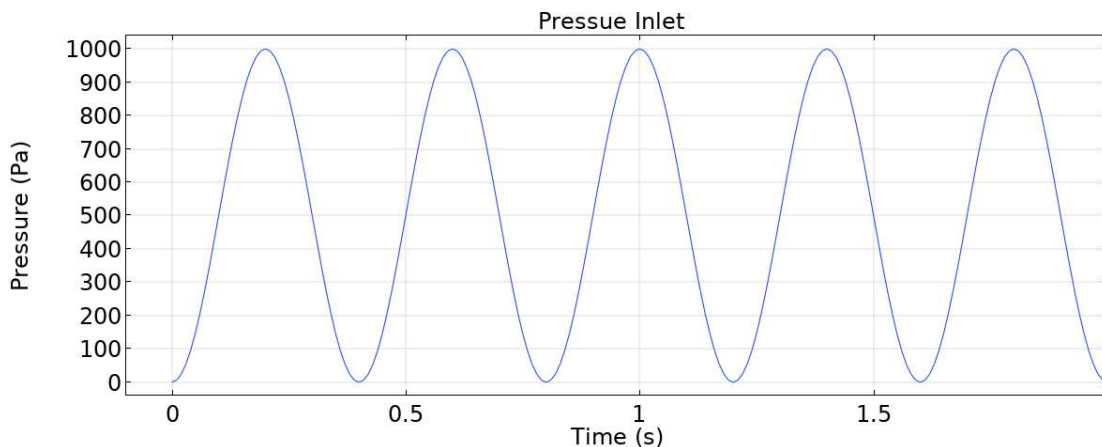


Figure 41: Pressure inlet A used in setup 2.

The second inlet condition (B) was still a pressure inlet with 1000Pa amplitude and 500Pa average but, in this case, the frequency was dropped to 1.25Hz (Figure 42). This results in a period of 0.8s, which roughly corresponds to the one of a normal cardiac cycle.

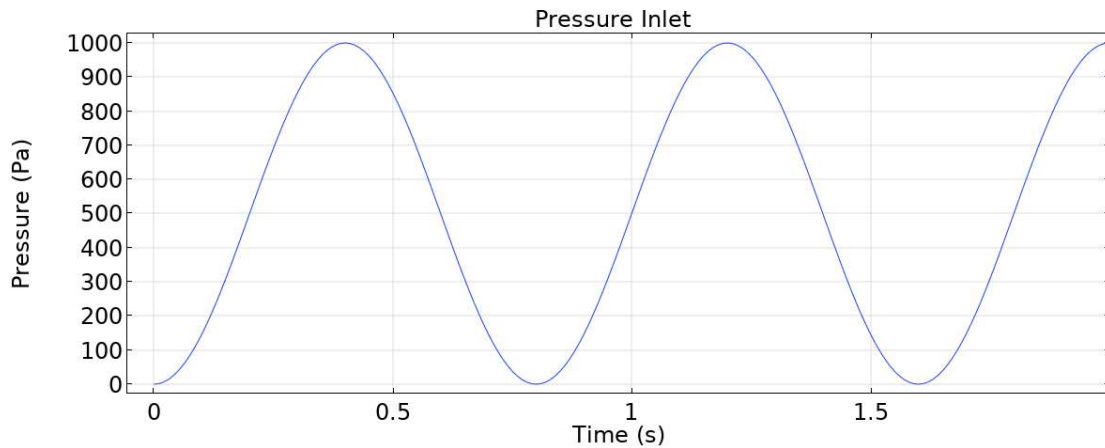


Figure 42: Pressure inlet (B) used in setup 2.

The third inlet condition (C) was a mass flow inlet condition, defined to resemble the one used by Martin et al. [39]. The wave had an amplitude of 5ml/s with a 0ml/s average and a frequency of 1.25Hz (Figure 43).

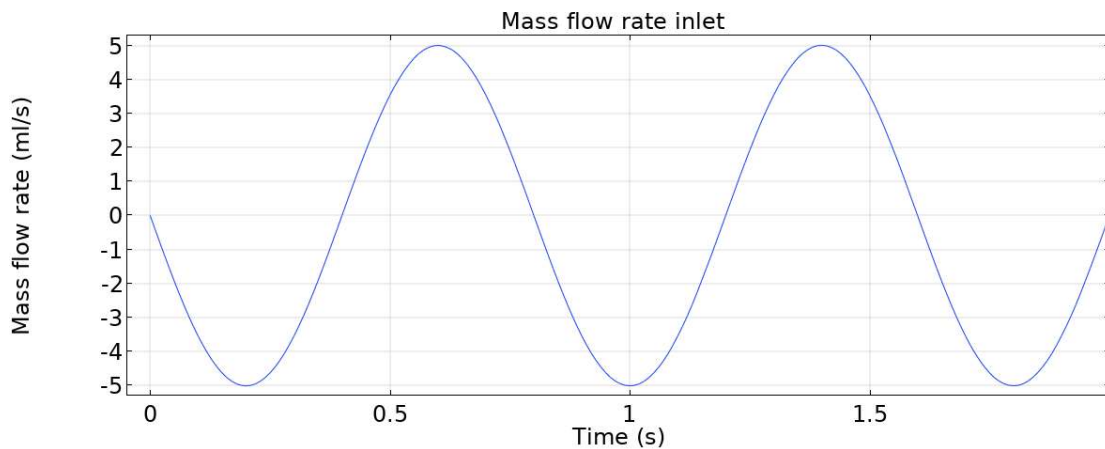


Figure 43: Mass flow inlet (C) used in setup 2.

### Setup 3

The last setup was intended to evaluate the differences between the case of a patient before and after the PFD. To do so the already described geometry was modified to resemble the one used by Martin et al. [38] in their experimental study. The syringe was extended to a total length of 200mm and an initial volume of 3.989ml. To obtain a geometry representing a patient before the PFD a block of 40mm length was introduced based on the one implemented by Martin et al. [38] (see Figure 44 right). The material properties correspond to those of setup 2 and are depicted in Table 6. The already described mass flow rate inlet condition (C) was used (see Figure 43).

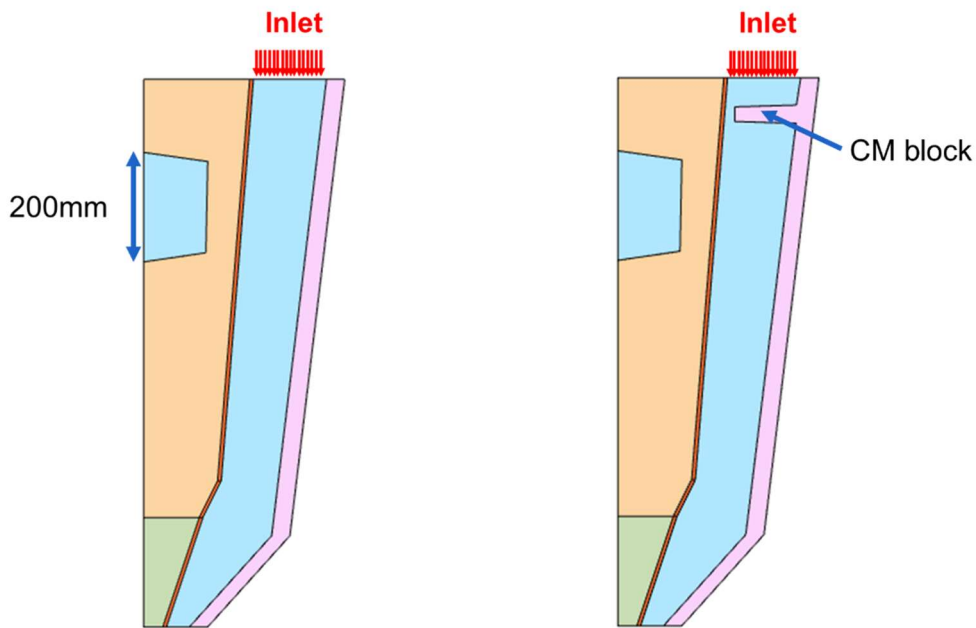


Figure 44: Scheme of the geometries used in setup 3, without CM (left) and with CM (right).

### 7.1.2 Mesh sensitivity study

As the presented model is a computational model a relevant part of it is the mesh choice. The optimal mesh should allow observation of all the relevant phenomena in the model while using the minimum number of elements to optimize the use of computational resources.

Different meshes with an increasing number of elements were built using COMSOL Multiphysics®. All the considered meshes were physics-controlled, meaning that the user does not have direct control over the mesh, but only indicates the required mesh size (normal, fine, coarse...). Triangular mesh elements were used, however, considering the experience gathered with the first model (see chapter 6.2.2 Time-dependent simulations), a boundary layer was always included at the interface between the fluid and the poroelastic materials as depicted in Figure 45.

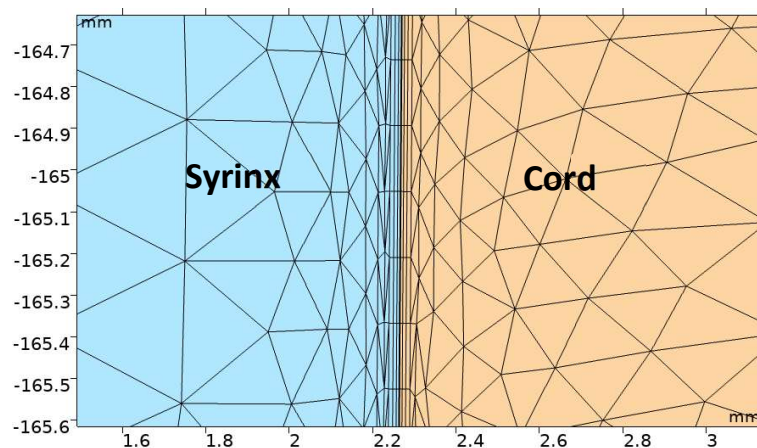


Figure 45: Section from mesh n1 highlighting the boundary layers.

Four different meshes were generated having the following mesh densities:

Table 7: Different mesh considered in mesh sensitivity study.

Mesh number	Number of elements
n1	93482
n2	222733
n3	296624
n4	553769

Setup 1 was used to carry out the study, to save time only one cycle was run for this purpose (0.5s). However, considering that at this point in time the model is in a transient phase three different time points (0.2s, 0.3s, 0.4s, see Figure 46 right) were chosen as evaluation points. Two main parameters, being the volume of the different compartments of the model (cord, filum, pia, syrxinx, SAS, and overall volume) and the instantaneous pressure value in six different points (depicted in Figure 46 left) were arbitrarily chosen to evaluate the stability of the results.

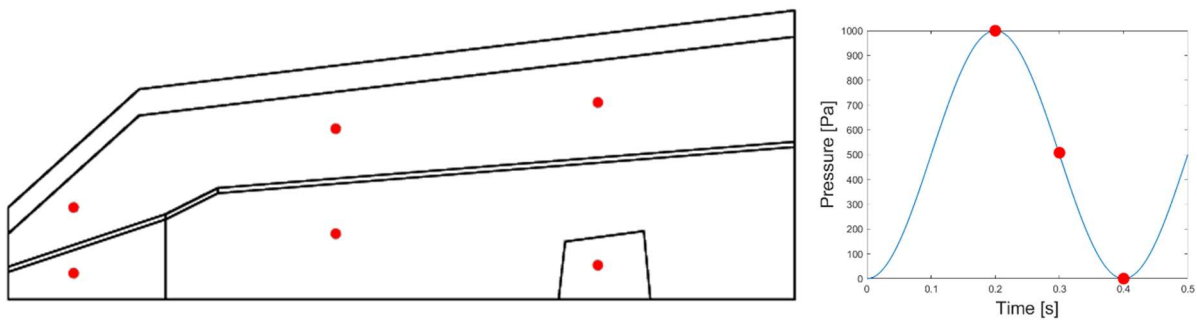


Figure 46: Scheme of the geometry with the position of pressure evaluation points (left). Plot of evaluation points in time over inlet profile (right).

The percentual difference between the calculated values was used to assess the stability of the results for the different mesh sizes. This parameter was obtained by evaluating the difference between a parameter recorded in a certain mesh and in the previous one, the obtained value is expressed in percentage of the value recorded in the coarser mesh (the one between the two with the smallest number of elements). This is done with the following formula:

$$Pd_n = \frac{v_{n-1} - v_n}{v_{n-1}}$$

Here is  $Pd_n$  the percentual difference,  $v_n$  the parameter value in the  $n^{\text{th}}$  mesh, and  $v_{n-1}$  the same parameter evaluated in mesh  $n-1$ . With this method three values were obtained for each parameter.

The obtained results are shown in the next plots (see Figures from 47 to 52). From these plots, a small percentual difference between the results corresponding to mesh n2 and n3 can be observed. This difference is in the order of 0.1% for the pressures and 0.001% for the volumes. Therefore, the mesh n2 was chosen. This mesh had a total of 222733 elements.

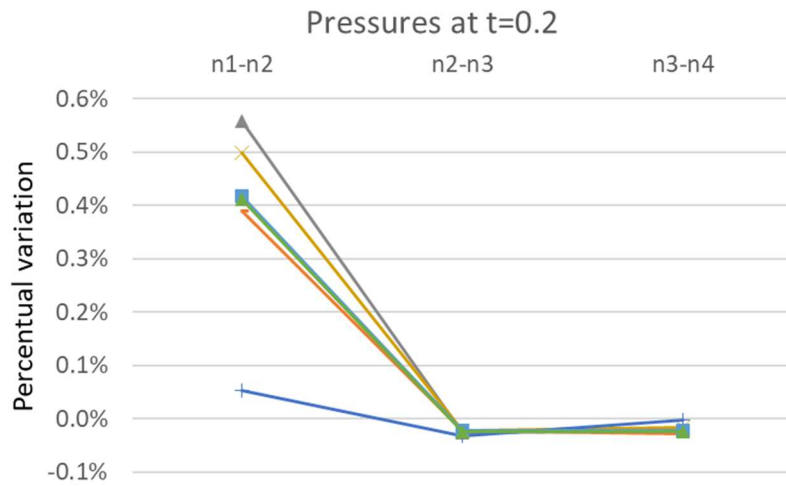


Figure 47: Pressure percentual variation at t=0.2.

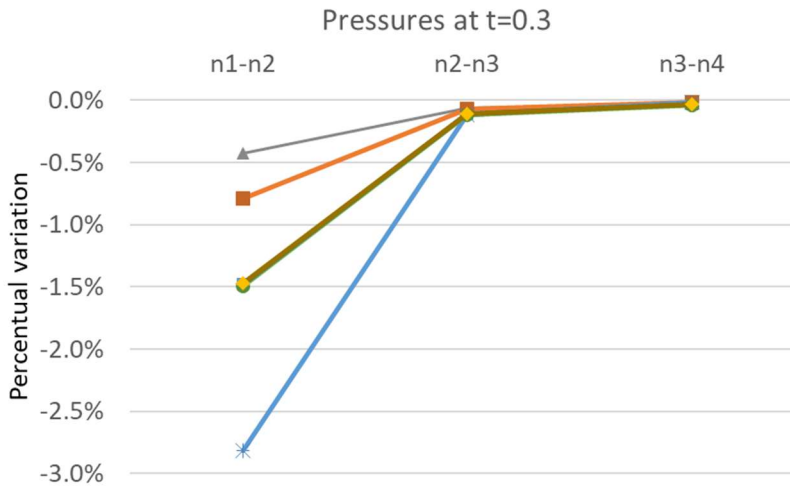


Figure 48: Pressure percentual variation at t=0.3.

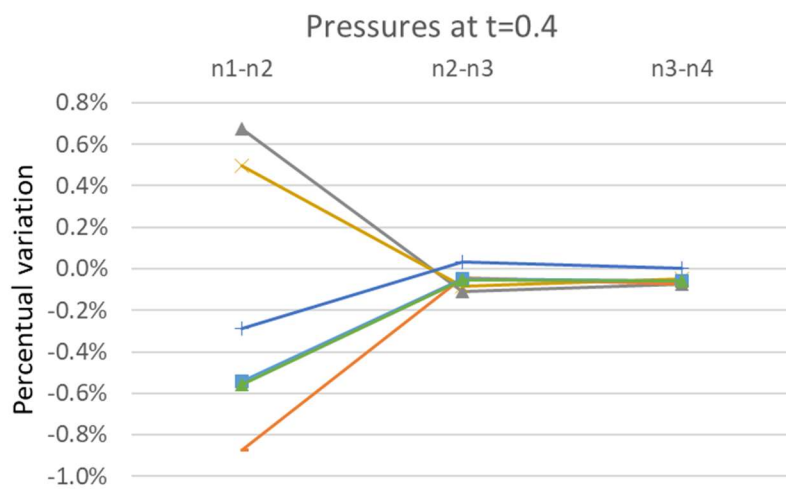


Figure 49: Pressure percentual variation at t=0.4.

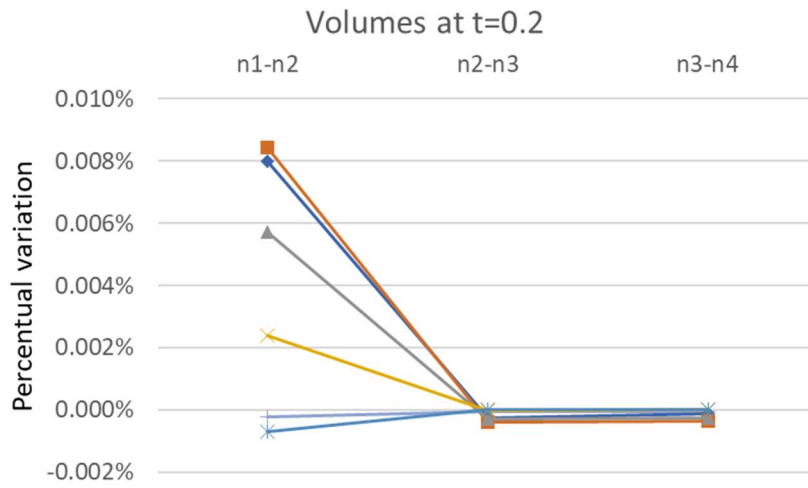


Figure 50: Volumes percentual variation at t=0.2.

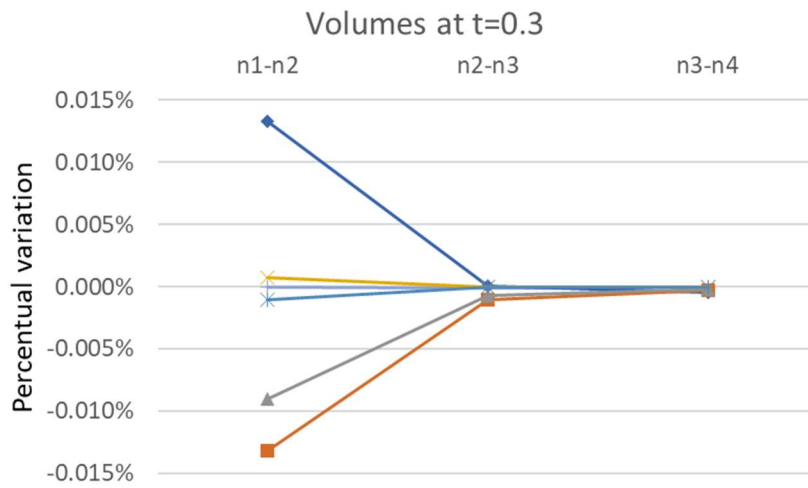


Figure 51: Pressure percentual variation at t=0.3.

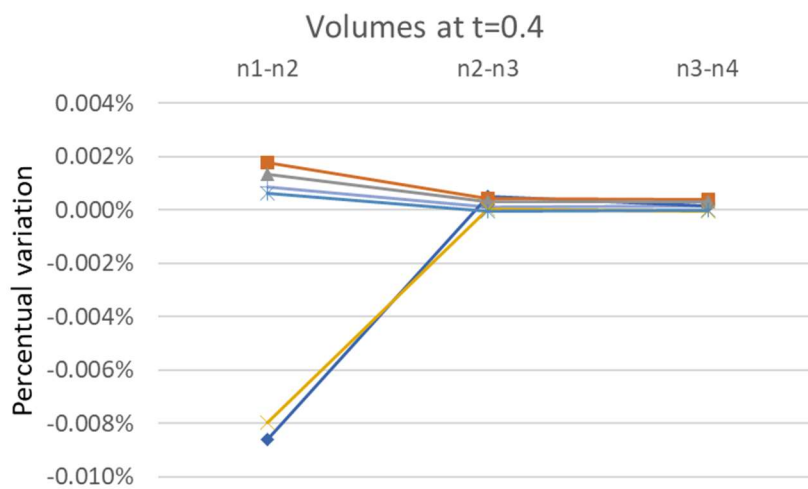


Figure 52: Pressure percentual variation at t=0.4.

## 7.2 Results

The three exposed setups led each one to evaluate different aspects of the interaction between the model geometry, the material properties, and the boundary conditions. The obtained results were processed using both the COMSOL Multiphysics® post processing tools and the commercially available software MATLAB.

### 7.2.1 Setup 1

The goal of this first setup is to assess the differences introduced in the model by the changes in material properties, specifically the permeability value of poroelastic materials.

All the models always present the same general behavior, the differences are mainly in the magnitude of the response. The models show an expected cyclic change in the overall volume. The SAS is expanding and contracting at the stimulus frequency and the movement of the solid components reflects this mechanism. During the first part of the cycle, when the fluid enters the model, the SAS expands mainly thanks to the extension of the dura towards the outside. In this phase the cord shows to swell in the top section and to shrink with the filum in the lower section. In the second phase of the cycle, when the fluid is exiting the model, the cord is shrinking at the top and swelling at the bottom (Figure 53). As effect of this movement the syringe is forced to move up and down, change shape and volume during every cycle.

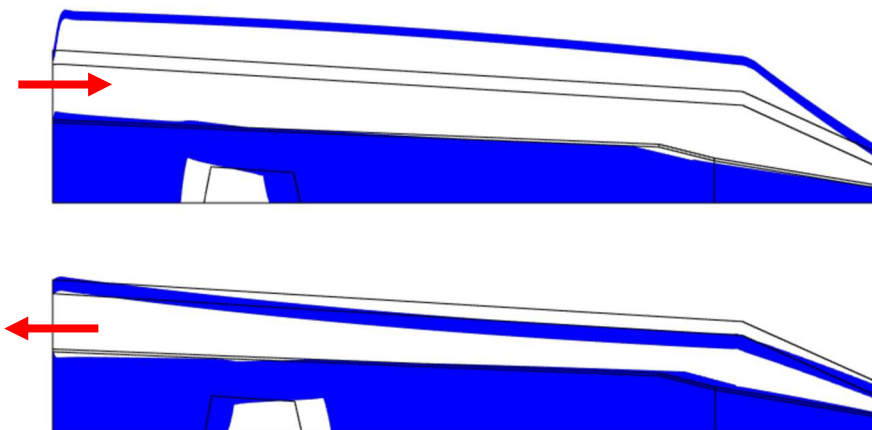


Figure 53: Solids deformation during inflow phase (top) and outflow phase (bottom). Deformation enhanced by 50 times.

One of the main parameters considered in the following sections is the volume change, this is difference between the instantaneous volume and the initial volume of one compartment (syrinx, SAS, spinal cord...). The different permeabilities don't introduce appreciable differences in the overall volume changes (change of the whole model volume). This is probably because the amount of fluid entering the model is mainly influenced by the boundary conditions, which are constant throughout the models. Therefore, the overall volume changes are almost constant (Figure 54). The SAS is the compartment accommodating the biggest part of this incoming fluid (more than 99%) and its behavior is consistent with the one of the overall volumes.

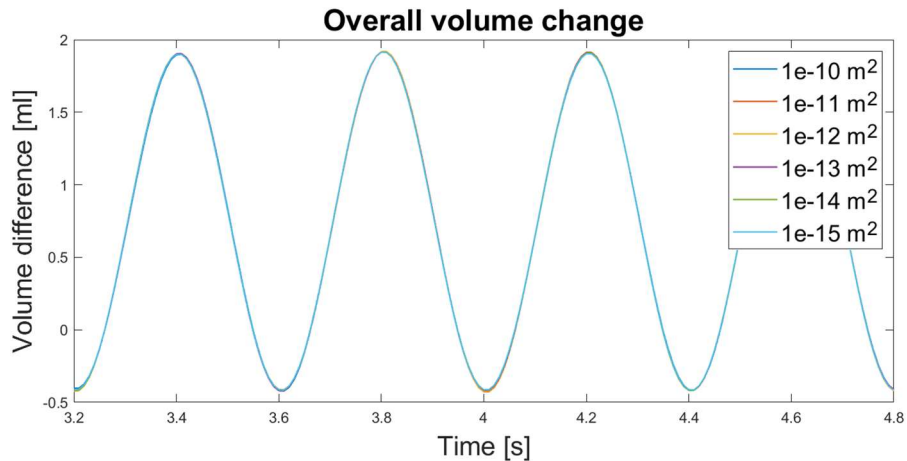


Figure 54: Overall volume changes in the last 4 cycles for models of setup 1 for different permeability values.

The responses of the poroelastic compartments are clearly some orders of magnitudes smaller than the overall volume changes (see Figures 55, 56) but presents a certain dependance on the used permeability value. The spinal cord volumes oscillations generally reflect the decrease in the permeability of the tissues. However, this relation is not linear. The difference in the response of the two models with the highest values ( $1e-10$  and  $1e-11$   $m^2$ ) is significantly smaller than the one between the two with mild values ( $1e-12$  and  $1e-14$   $m^2$ ) (see Figure 55). A lower value of permeability also induces a higher delay in the solid response. It is possible to observe that the peak of the volume change is delayed with the decrease in permeability.

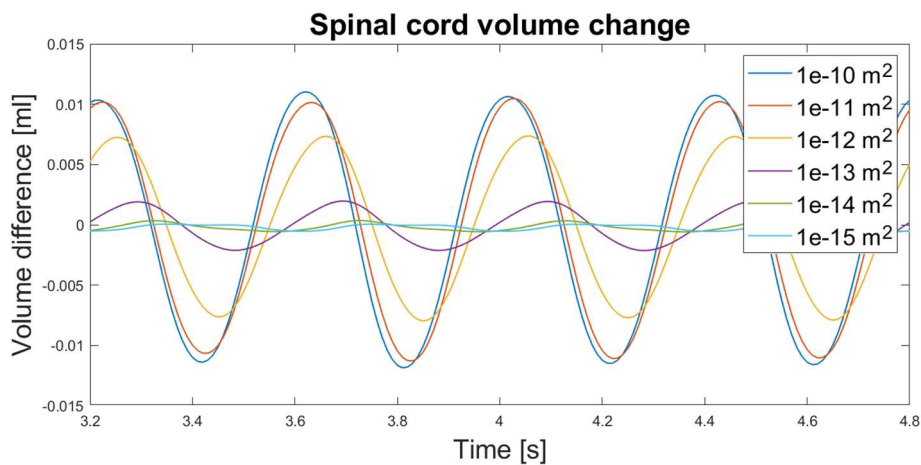


Figure 55: Spinal cord volume changes in the last 4 cycles for models of setup 1 for different permeability values.

The syrxin shows a particular behavior. The volumes changes are not dropping along with the decrease in permeability. The permeability value inducing the biggest volume change is  $1e-12m^2$  while greater values ( $1e-11$  and  $1e-10$   $m^2$ ) induces the smallest volume changes (Figure 56). When the permeability is lower than  $1e-13$  the syrxin volume change is constant. This suggests that with so low permeability values the effect of fluid entering or exiting the syrxin is negligible. Therefore, the syrxin volume changes may not be related to fluid entering or exiting. Rather, it may be mainly due to the movement of the surrounding poroelastic solids. Which cause the movement of the syrxin boundaries and subsequently induces volume changes.

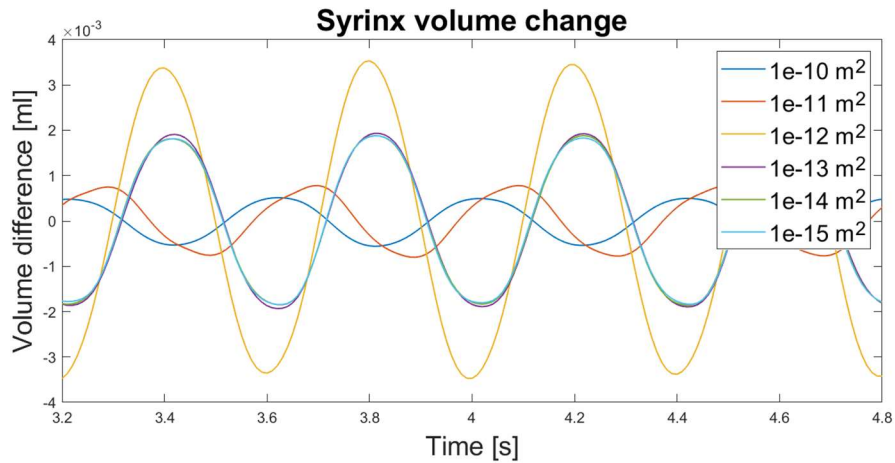


Figure 56: Syring volume changes in the last 4 cycles for models of setup 1 for different permeability values.

The mass flow rate through the syring surface gives an indication of the amount of fluid exchanged between the syring and the spinal cord. The peak value drops along with the decreasing permeability (see Table 8) highlighting the relation between these two parameters.

Table 8: Table of mass flow rate peak values recorded at syring border.

Permeability [m <sup>2</sup> ]	Mass flow rate peak [ml/s]
<b>1e-10</b>	1.2
<b>1e-11</b>	0.12
<b>1e-12</b>	0.012
<b>1e-13</b>	0.0035
<b>1e-14</b>	0.0011
<b>1e-15</b>	0.00032

An interesting parameter to look at is the pressure difference between the syring and the corresponding SAS. The pressure inside the syring is constant throughout the space, while this is not the case for the SAS. Therefore, the pressure difference between syring and SAS at a certain height is not constant. As can be observed in Figure 57, while in part of the syring the pressure difference with the SAS is positive in the other part it is negative.

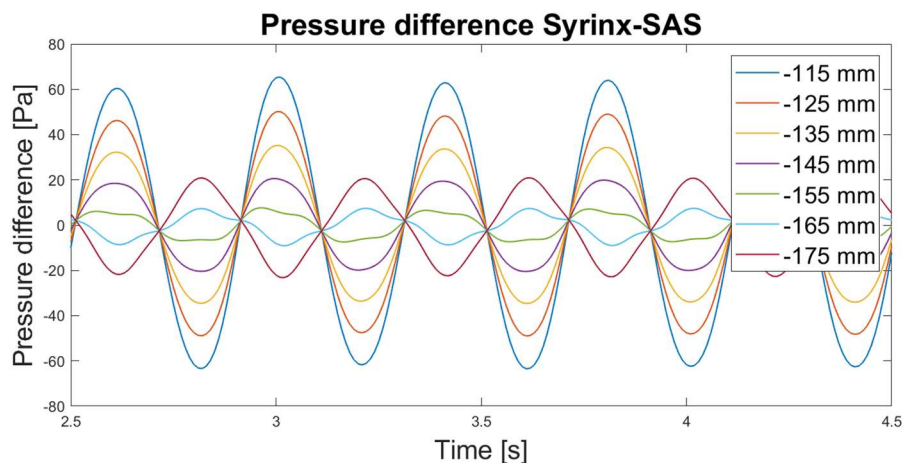


Figure 57: Syring-SAS pressure difference at different z coordinates (legend). The coordinates are in mm and the syring extends from -110 (top) to -180 mm (bottom).

The evolution of pressure difference generates a velocity field with fluid part entering the syringe from one side (top or bottom) and part exiting from the other. This pattern changes direction with the same frequency of the inlet wave as can be deduced from Figure 57. As deduced from the first study, some time is needed for the flow to be established through the poroelastic material. This amount of time increases with the decreasing permeability. Therefore, knowing that the pressure difference is cyclically changing, only in the model with higher permeability is possible to observe a clear flow from the SAS to the syringe through the spinal cord and vice-versa (Figure 58). While in the other models a clear flow through the spinal cord is harder to observe. The velocity magnitude of the fluid inside the syringe is in the order of  $e-5$ m/s. From Figure 58 is also possible to notice that the movement of the fluid inside the syringe change direction when the permeability decrease.

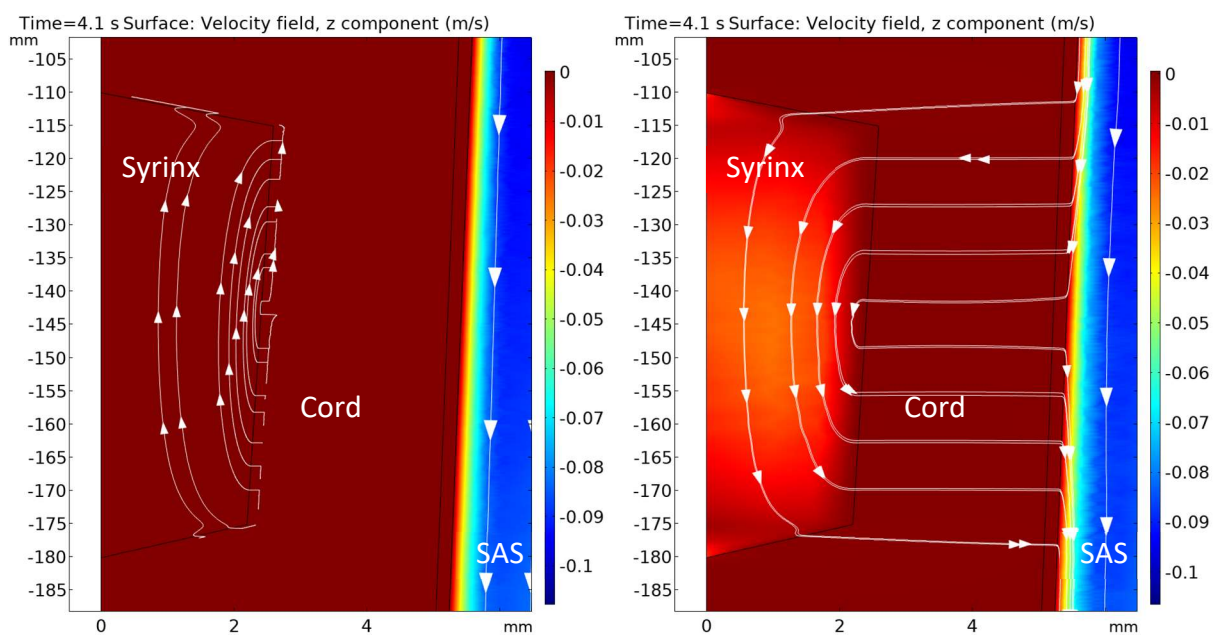


Figure 58: Streamlines comparison between model with permeability  $1e-13m^2$  (left) and  $1e-10m^2$  (right), during inflow phase.

### 7.2.2 Setup 2

This setup was intended to evaluate the influence of the inlet function on the model response. The effect of the applied inlets (A, B, C, see chapter 7.1.1) is visible in several different parameters, the focus in this section will be on the pressures and volume changes over time. The flow patterns were the same showed in section 7.2.1.

The different inlet conditions influence the volume increase of the model, as can be observed in Figure 59. The inlet A shows higher volume changes than the other 2 and inlet C is the one showing the least increase in volume. This finding is consistent with the pressures observed at the inlet, where condition C presents a lower amplitude (roughly 850Pa) than the one induced by conditions A and B (1000Pa).

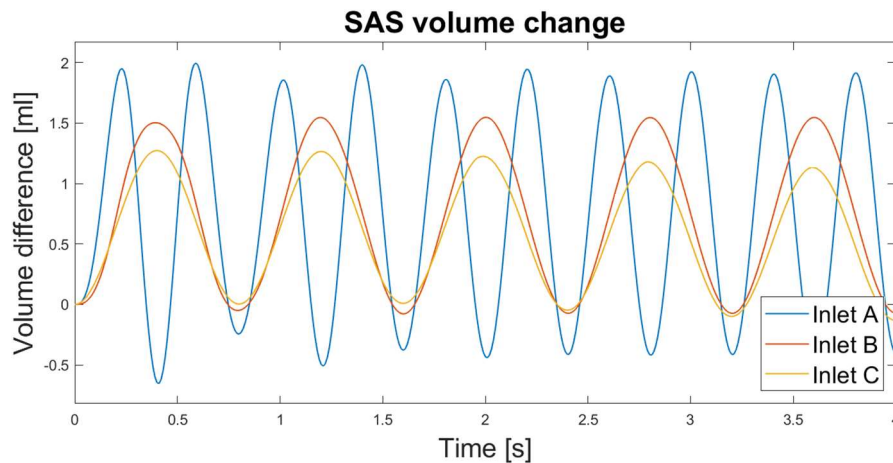


Figure 59: SAS volume changes for models of setup 2. A) pressure inlet amplitude 500Pa frequency 2.5 Hz. B) pressure inlet amplitude 500Pa frequency 1.25 Hz. C mass flow rate inlet amplitude 5ml/s frequency 1.25 Hz

Comparing the effect of conditions A and B is possible to notice the influence of the wave frequency. The model response to the wave with lower frequency is smaller in terms of both volume changes in any compartment and mass flow rate at the inlet.

Looking at the volume changes of the syringe and spinal cord is possible to observe the same behavior with a lower frequency corresponding to a lower response (see Figure 60). However, as these changes are small in magnitude, the differences between the models are reduced too.

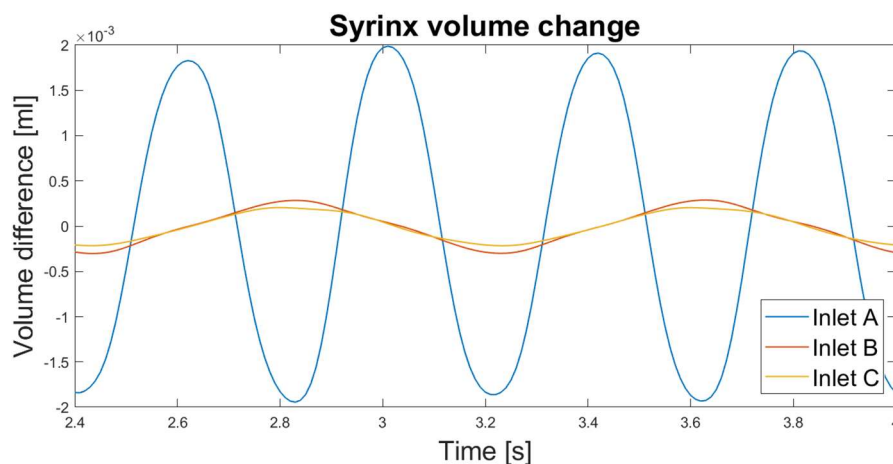


Figure 60: Syringe volume changes in the last 1.6s (2 or 4 cycles) for models of setup 2.

A relevant thing which can be noticed when applying inlet condition C, is the oscillation of the average value of the model response. Which can be observed both in the SAS volume change (Figure 59) and in the fluid pressure in the SAS (Figure 61). The elements causing the presence of this low frequency component are not yet clear and would need further investigations to be identified.

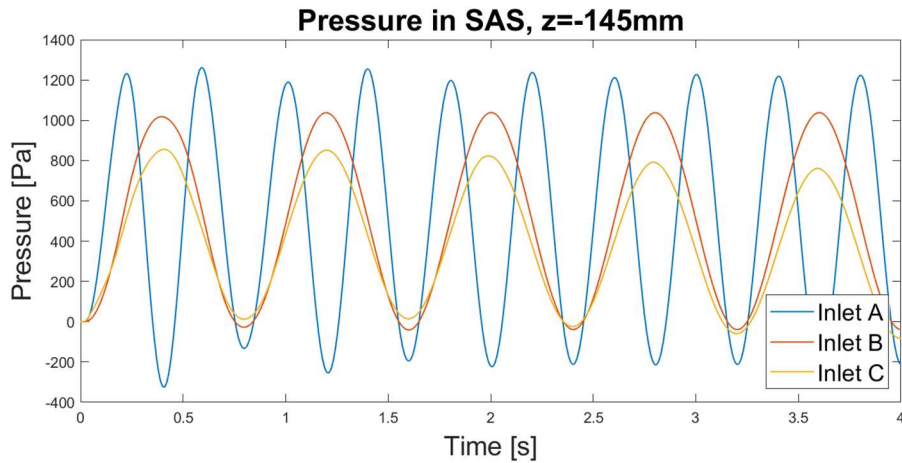


Figure 61: Pressure in SAS at z=-145mm (syrinx location) for models of setup 2.

### 7.2.3 Setup 3

The goal of the last setup was to evaluate the differences between a model with and without the Chiari malformation.

The presence of the malformation induces little changes in the volume's differences. No difference in the response amplitude can be observed in the overall volume change. However, in the model without the Chiari malformation is possible to observe a background low frequency wave (Figure 62). This wave was already observed in setup 2 when the inlet condition C was applied and can be observed also when looking at the pressure oscillations inside the SAS.

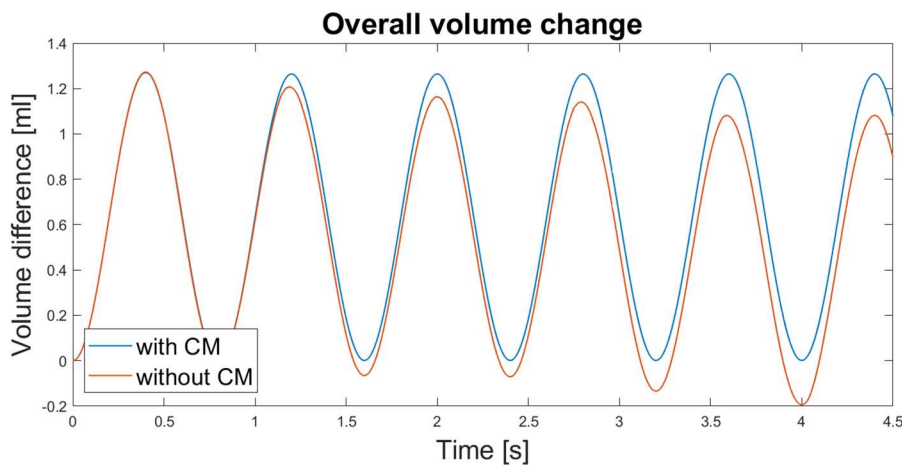


Figure 62: Overall volume changes for models of setup 3

The effect of the malformation on the syring volume changes is mainly to introduce an anticipation in the response to the inlet wave (Figure 63). With the model without the geometry showing a lag of around 60 ms with respect to the other one. The amplitude of this oscillation is also roughly the same in the two models and is consistent with the one presented by Bertram et al. [48].

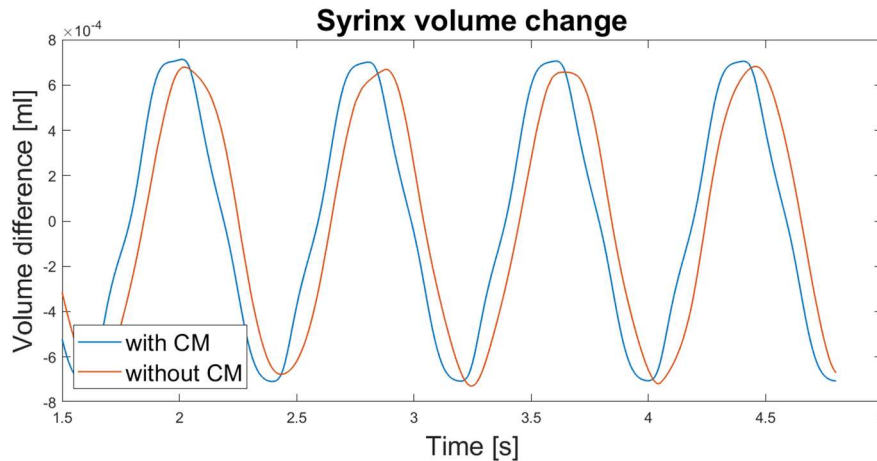


Figure 63: Syring volume changes in the last 4 cycles for models of setup 3.

A relevant difference is observable when looking at the volume changes of the spinal cord. The model without the malformation presents a smaller amplitude of the response (Figure 64). While the other one not only present a bigger amplitude but also a different average value highlighting a general reduction in the volume of the spinal cord. The same phenomenon is observed in the pia.

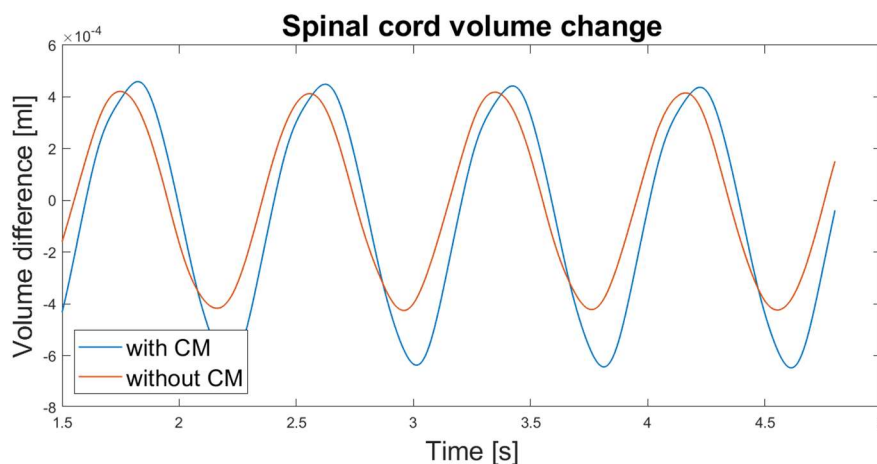


Figure 64: Spinal cord volume changes in the last 4 cycles for models of setup 3

This difference in volume changes of spinal cord and pia is probably due to the restriction of the SAS caused by the malformation. When the fluid is flowing inside the SAS, the upper section of the spinal cord (right before and near the narrowing) is compressed by the fluid (Figure 65). On the other hand, when the fluid is flowing outwards the upstream section of the spinal cord is stretched toward the outside. These deformations are clearly not present in the model without the malformation which behave as the one of setup 2 C.

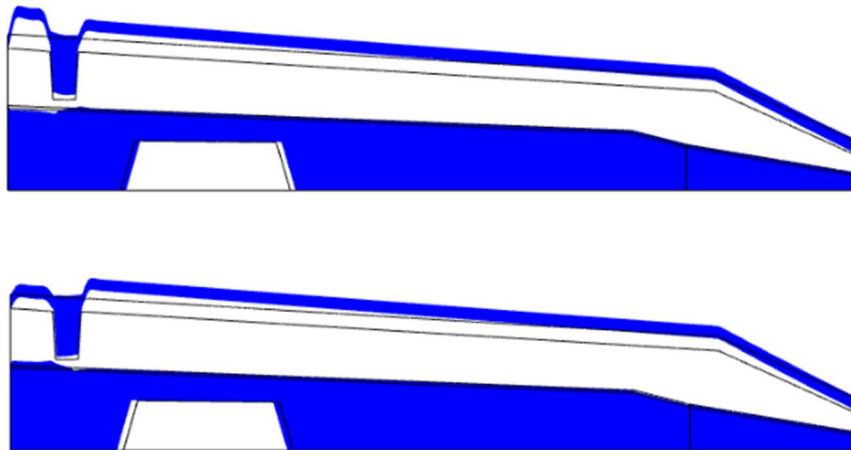


Figure 65: Solids deformation during inflow phase (top) and outflow phase (bottom). Setup 3 model with CM. Deformation enhanced by 50 times.

The flow patterns inside the spinal cord and syringe are consistent between the models and are also similar to the ones observed in the previous setups. A sort of recirculatory fluid movement like the one described by Bertram et al. [48] is present. However, as in setup 1 this cannot be clearly observed (Figure 66). This is mainly because velocity of the fluid inside the spinal cord is in the order of  $1e-8$   $1e-7$  m/s. The low velocity coupled with the cyclic changes in the flow pattern highlight the fact that there is not a proper fluid flow between the syringe and the SAS. Rather, at every cycle some fluid moves back and forth between the SAS and the Spinal cord and some moves between the spinal cord and the Syringe. From the simulations these movements look to be balanced and seems not to cause any change in the average syringe volume. However, some imbalances may be present that are too small to be captured by the presented models.

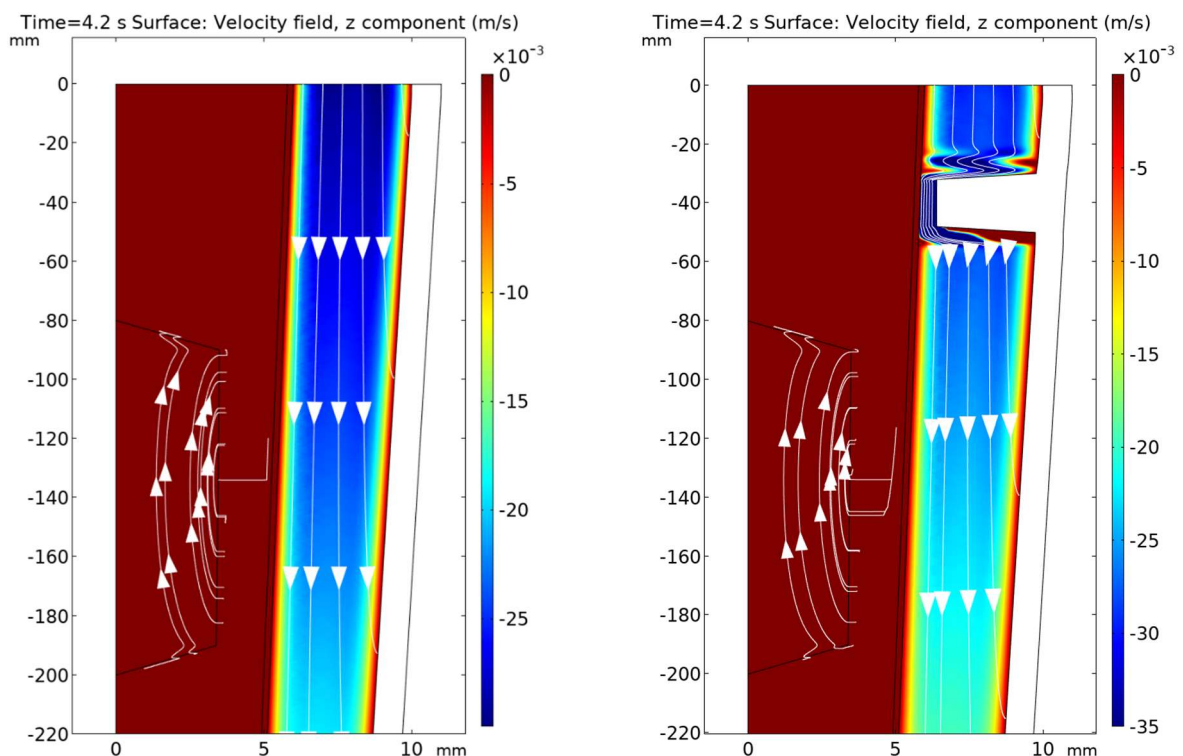


Figure 66: Streamlines comparison between models of setup 3 (model with CM on the right, model without CM on the left) during inflow phase.

### 7.3 Discussion

The different setup used in this second study highlighted many different aspects of the relation between the material properties, the boundary conditions, and the geometry.

Setup 1 shows that the fluid mass forced in and out depends only on the applied boundary condition regardless of the properties of the poroelastic materials. This is clear when looking at Figure 54. The poroelastic compartments are, as expected, the most influenced by the permeability variations. The Spinal cord volume change decreases with smaller permeability values. This can be related to the fact that a smaller value would decrease the amount of fluid entering the material. This is not the case for the syrxn volume, in which oscillations show a nonlinear relation with the permeability. For values smaller than  $1e-13 \text{ m}^2$  the volume changes became constant. This may lead to suppose that at this low permeabilities the influence of fluid moving across the spinal cord is negligible. The volume changes will mainly be due to the deformations imposed by the movement of the surrounding solid tissues. For permeability values greater than  $1e-13 \text{ m}^2$  the amplitude of volumes oscillations appears to increase for  $1e-12 \text{ m}^2$  and then decrease for  $1e-11$  and  $1e-10 \text{ m}^2$ . A clear reason for this behavior has not been found yet and further investigations are needed to clarify this point.

Even though a clear flow can be observed only in models with high permeability (Figure 58), the pressure difference between syrxn and SAS depicted in Figure 57 suggests that a sort of fluid circulation should be always present in this region. The simultaneous inflow and outflow of fluid is not balanced and therefore may play a role in the syrxn volume oscillations.

The models in setup 2 show that the frequency of the inlet wave has a relevant influence on the amount of fluid forced in and out of the model. Higher frequencies, corresponding to the effects of Valsalva's maneuvers or coughing [48], force a higher amount of mass inside the studied domain. This change is also related to the pressure reached inside the SAS. Higher pressures are related to higher mass inflows both in the SAS and in the syrxn.

The last setup was meant to grasp the differences between the condition with and without the Chiari Malformation. The pressures recorded in the syrxn and in the corresponding SAS are quite similar and the maximum difference is in the order of 7 Pa for both the considered geometries. This finding is consistent with the results of Martin et al. [39] experimental study, where the relative pressure difference was considered negligible.

No relevant changes are observed when looking at the syrxn volume oscillations. While a clear change is present in the spinal cord volume oscillations. In the model with CM is possible to observe an increase in the shrinkage and swelling of the top section of the spinal cord itself. In this region, the presence of the CM increases both the mechanical stress and the amount of fluid forced through the pia into the spinal cord causing bigger volume variations throughout a single cycle. This phenomenon leads also to a reduction in the average volume of the spinal cord when the CM is present. To my knowledge, this effect has never been previously highlighted in literature, however, it is probably related to the simplifications considered in this specific study.

As in the previous setups is thought to observe a proper flow between the SAS and the syrxinx. This is the result of the combined effect of time needed for the flow to establish and the continuous change in pressure conditions. Similarly to Bertram et al. [48], only very limited fluid movements can be observed between these two compartments, with small amounts of mass simultaneously entering and exiting the syrxinx. These mass movements may not have exactly zero sum, and therefore play a role in the syrxinx evolution. However, probably the time scale of the models used in this study is too small to capture this effect, as in the clinical cases the reduction or growth of a syrxinx happens in months. To be able to observe this type of evolution it would be necessary to simulate weeks or months of cardiac cycles, as already stated by Bertram et al. [48] for the same problem.

In the model of setup 2 C and in the one without CM in setup 3, a peculiar background low frequency wave is recorded. The wave can be observed in the SAS pressure (Figure 61), in the SAS and Overall volumes (Figure 599, 62), and in the inlet pressure. The wave may be related to the use of a mass flow inlet instead of a pressure one. However, the presence of the CM seems to remove it from the model response. At this point is not clear how this wave is originated (physical or computational origin), or which elements contribute to its presence. Further investigations are needed to fully understand this event.

The results of this study are influenced by the several simplifications done during the buildup of the final model. The used axisymmetric geometry is highly idealized, and all the structures are modeled in isolation from the brain and the skull. The design adopted to model the CM is far from the real situation and cannot consider the movement of the herniated tonsils or the complete obstruction of the fluid passage. The trabeculae, denticulate ligament, and nerves populating the SAS are completely neglected. Moreover, also when modeling a syrxinx, the outer diameter of the spinal cord is kept constant. All the materials are modeled as isotropic for all their properties. Although this is not the case for the spinal cord permeability [59]. Also, all the poroelastic materials are considered to have the same permeability. The periodic CSF impulsion from the cranial subarachnoid space is simplified with a sinusoidal wave with nonzero average.

## 8 Conclusions

In conclusion, this work gave to the reader a deeper look into the poroelasticity both in general and applied to CM-related syringomyelia.

The first part of this study can give a good basis for the understanding of the spinal cord poroelastic behavior. Being the starting point for future works in the same area of computational modeling. The presented relations between permeability, pressure, and swelling can be used to estimate the behavior of more complex poroelastic models. The role of Young's modulus and Poisson's ratio in the material behavior was shown. The influence of the geometrical properties of the studied domain was highlighted. All these findings can help to better understand the poroelastic behavior of the spinal cord. Moreover, the same study setup can be used to evaluate the differences between various physical models (viscoelastic or hyper-elastic materials) to find the most accurate one.

The study conducted about the CM can give an overview of the spinal cord behavior in different situations. The presented volume oscillations show the cyclic nature of all the movements of the spinal cord and SAS. The syrinx volume changes showed a peculiar relation with the permeability which may be further investigated.

Further steps can be taken to prosecute the work presented in this thesis. The modeling of materials can be improved by considering anisotropies, as well as the different values of permeability. These improvements may help to better reproduce the behavior of the spinal cord and surrounding structures. In vivo recorded, data can be used to create and implement more accurate CSF inlet conditions. The geometry can be extended to include the cerebral tonsils and allow the modeling of their movements. This extension may include the modeling of the one-way valve mechanism described in chapter 4 and evaluate its effect on the syrinx. Finally, patient-specific 3D geometries can be used to remove any simplification in the geometry and capture phenomena that cannot be observed in the 2D geometry.



## References

- [1] P. Brodal, *The central nervous system: Structure and function (4th ed.)*. 2010.
- [2] H. J. ten Donkelaar, "Overview of the human brain and spinal cord," in *Clinical Neuroanatomy: Brain Circuitry and Its Disorders*, 2020. doi: 10.1007/978-3-030-41878-6\_1.
- [3] Watson Charles, Kirkcaldie Matthew, and Paxinos George, *The Brain : An Introduction to Functional Neuroanatomy*. Saint Louis, UNITED STATES: Elsevier Science & Technology, 2010.
- [4] Merriam Webster, "Merriam-Webster Unabridged Dictionary," *Merriam Webster*, 2019.
- [5] F. Adam, *Neuroanatomy Draw it to know it*. 2009.
- [6] J. J. Illiff, A. S. Thrane, and M. Nedergaard, "The Glymphatic System and Brain Interstitial Fluid Homeostasis," in *Primer on Cerebrovascular Diseases*, Elsevier, 2017. doi: 10.1016/B978-0-12-803058-5.00003-5.
- [7] M. A. Lam, S. J. Hemley, E. Najafi, N. G. F. Vella, L. E. Bilston, and M. A. Stoodley, "The ultrastructure of spinal cord perivascular spaces: Implications for the circulation of cerebrospinal fluid," *Scientific Reports*, vol. 7, no. 1, 2017, doi: 10.1038/s41598-017-13455-4.
- [8] Conor Mallucci and Spyros Sgouros, *Cerebrospinal Fluid Disorders*, 1st ed. CRC Press, 2010. doi: 10.3109/9781420016284.
- [9] B. L. Sun *et al.*, "Lymphatic drainage system of the brain: A novel target for intervention of neurological diseases," *Progress in Neurobiology*, vol. 163–164. 2018. doi: 10.1016/j.pneurobio.2017.08.007.
- [10] H. M. Tully and W. B. Dobyns, "Infantile hydrocephalus: A review of epidemiology, classification and causes," *European Journal of Medical Genetics*, vol. 57, no. 8, 2014, doi: 10.1016/j.ejmg.2014.06.002.
- [11] J. A. Hidalgo, C. A. Tork, and M. Varacallo, *Arnold Chiari Malformation*. StatPearls Publishing, Treasure Island (FL), 2020. [Online]. Available: <http://europepmc.org/books/NBK431076>
- [12] T. J. Buell, J. D. Heiss, and E. H. Oldfield, "Pathogenesis and Cerebrospinal Fluid Hydrodynamics of the Chiari I Malformation," *Neurosurgery Clinics of North America*, vol. 26, no. 4. 2015. doi: 10.1016/j.nec.2015.06.003.
- [13] R. W. Eldaya, J. M. Strahle, and M. S. Goyal, "Advanced Imaging of Chiari I Malformations," in *The Chiari Malformations*, 2020. doi: 10.1007/978-3-030-44862-2\_28.

- [14] M. M. Shoja, J. Johal, W. J. Oakes, and R. S. Tubbs, "Embryology and pathophysiology of the Chiari I and II malformations: A comprehensive review," *Clinical Anatomy*, vol. 31, no. 2. 2018. doi: 10.1002/ca.22939.
- [15] J. Meadows, M. Kraut, M. Guarnieri, R. I. Haroun, and B. S. Carson, "Asymptomatic Chiari Type I malformations identified on magnetic resonance imaging," *Journal of Neurosurgery*, vol. 92, no. 6, 2000, doi: 10.3171/jns.2000.92.6.0920.
- [16] L. A. Aitken *et al.*, "Chiari Type I Malformation in a Pediatric Population," *Pediatric Neurology*, vol. 40, no. 6, 2009, doi: 10.1016/j.pediatrneurol.2009.01.003.
- [17] J. Strahle, K. M. Muraszko, J. Kapurch, J. R. Bapuraj, H. J. L. Garton, and C. O. Maher, "Chiari malformation Type I and syrinx in children undergoing magnetic resonance imaging: Clinical article," *Journal of Neurosurgery: Pediatrics*, vol. 8, no. 2, 2011, doi: 10.3171/2011.5.PEDS1121.
- [18] T. H. Milhorat *et al.*, "Chiari I malformation redefined: Clinical and radiographic findings for 364 symptomatic patients," *Neurosurgery*, vol. 44, no. 5, 1999, doi: 10.1097/00006123-199905000-00042.
- [19] P. Mastorakos and J. D. Heiss, "Treatment of the Adult Chiari I Malformation," in *The Chiari Malformations*, 2020. doi: 10.1007/978-3-030-44862-2\_38.
- [20] A. A. Fernández *et al.*, "Malformations of the craniocervical junction (chiari type i and syringomyelia: Classification, diagnosis and treatment)," *BMC Musculoskeletal Disorders*, vol. 10, no. SUPPL. 1. 2009. doi: 10.1186/1471-2474-10-S1-S1.
- [21] E. B. Dupépe, K. Zimmerman, and B. G. Rocque, "Syringomyelia and the Chiari Malformations," in *The Chiari Malformations*, Cham: Springer International Publishing, 2020. doi: 10.1007/978-3-030-44862-2\_15.
- [22] J. Guyotat, P. Bret, E. Jouanneau, A. C. Ricci, and C. Lapras, "Syringomyelia associated with type I Chiari malformation. A 21-year retrospective study on 75 cases treated by foramen magnum decompression with a special emphasis on the value of tonsils resection," *Acta Neurochirurgica*, vol. 140, no. 8, 1998, doi: 10.1007/s007010050175.
- [23] F. Shweikeh, D. Sunjaya, M. Nuno, D. Drazin, and M. A. Adamo, "National Trends, Complications, and Hospital Charges in Pediatric Patients with Chiari Malformation Type I Treated with Posterior Fossa Decompression with and without Duraplasty," *Pediatric Neurosurgery*, vol. 50, no. 1, Feb. 2015, doi: 10.1159/000371659.
- [24] S. Butensky, S. Rodgers, S. Baron, S. Schneider, and M. Mittler, "Comparison of surgical outcomes in patients with Chiari Type I malformation receiving posterior fossa decompression with and without duraplasty," *Child's Nervous System*, vol. 36, no. 7, 2020, doi: 10.1007/s00381-020-04667-7.

- [25] N. S. J. Elliott, C. D. Bertram, B. A. Martin, and A. R. Brodbelt, "Syringomyelia: A review of the biomechanics," *Journal of Fluids and Structures*, vol. 40, 2013, doi: 10.1016/j.jfluidstructs.2013.01.010.
- [26] N. Aghakhani *et al.*, "Long-term follow-up of chiari-related syringomyelia in adults: Analysis of 157 surgically treated cases," *Neurosurgery*, vol. 64, no. 2, 2009, doi: 10.1227/01.NEU.0000336768.95044.80.
- [27] K Sivaramakrishna and K Sathyavaraprasad, "Study on Syringomyelia," *International Journal of Contemporary Medical Research*, vol. 4, no. 10, pp. 2211–2214, Oct. 2017.
- [28] A. Kleindienst, F. M. Laut, V. Roেকেlein, M. Buchfelder, and F. Dodoo-Schittko, "Treatment of posttraumatic syringomyelia: evidence from a systematic review," *Acta Neurochirurgica*, vol. 162, no. 10. 2020. doi: 10.1007/s00701-020-04529-w.
- [29] A. R. Brodbelt and M. A. Stoodley, "Post-traumatic syringomyelia: A review," *Journal of Clinical Neuroscience*, vol. 10, no. 4. 2003. doi: 10.1016/S0967-5868(02)00326-0.
- [30] J. Soleman, J. Roth, and S. Constantini, "Syringo-subarachnoid shunt: how I do it," *Acta Neurochirurgica*, vol. 161, no. 2, 2019, doi: 10.1007/s00701-019-03810-x.
- [31] W. J. GARDNER and J. ANGEL, "The cause of syringomyelia and its surgical treatment.," *Cleveland Clinic quarterly*, vol. 25, no. 1, 1958, doi: 10.3949/ccjm.25.1.4.
- [32] J. D. Heiss *et al.*, "Elucidating the pathophysiology of syringomyelia," *Journal of neurosurgery*, vol. 91, no. 4, pp. 553–562, 1999.
- [33] B. Williams, "THE DISTENDING FORCE IN THE PRODUCTION OF " COMMUNICATING SYRINGOMYELIA " ," *The Lancet*, vol. 294, no. 7613, Jul. 1969, doi: 10.1016/S0140-6736(69)91427-5.
- [34] B. Williams, "On the pathogenesis of syringomyelia: a review," *Journal of the Royal Society of Medicine*, vol. 73, no. 11. 1980. doi: 10.1177/014107688007301109.
- [35] E. H. Oldfield, K. Muraszko, T. H. Shawker, and N. J. Patronas, "Pathophysiology of syringomyelia associated with Chiari I malformation of the cerebellar tonsils. Implications for diagnosis and treatment," *Journal of Neurosurgery*, vol. 80, no. 1, 1994, doi: 10.3171/jns.1994.80.1.0003.
- [36] T. H. Milhorat, A. L. Capocelli, R. M. Kotzen, P. Bolognese, I. M. Heger, and J. E. Cottrell, "Intramedullary pressure in syringomyelia: Clinical and pathophysiological correlates of syrinx distension," *Neurosurgery*, vol. 41, no. 5, 1997, doi: 10.1097/00006123-199711000-00014.
- [37] M. Markl, A. Frydrychowicz, S. Kozerke, M. Hope, and O. Wieben, "4D flow MRI," *Journal of Magnetic Resonance Imaging*, vol. 36, no. 5. 2012. doi: 10.1002/jmri.23632.
- [38] B. A. Martin, R. Labuda, T. J. Royston, J. N. Oshinski, B. Iskandar, and F. Loth, "Spinal subarachnoid space pressure measurements in an in vitro spinal stenosis model:

- Implications on syringomyelia theories,” *Journal of Biomechanical Engineering*, vol. 132, no. 11, 2010, doi: 10.1115/1.4000089.
- [39] B. A. Martin and F. Loth, “The influence of coughing on cerebrospinal fluid pressure in an in vitro syringomyelia model with spinal subarachnoid space stenosis,” *Cerebrospinal Fluid Research*, vol. 6, no. 1, 2009, doi: 10.1186/1743-8454-6-17.
- [40] A. Helgeland, K. A. Mardal, V. Haughton, and B. A. P. Reif, “Numerical simulations of the pulsating flow of cerebrospinal fluid flow in the cervical spinal canal of a Chiari patient,” *Journal of Biomechanics*, vol. 47, no. 5, 2014, doi: 10.1016/j.jbiomech.2013.12.023.
- [41] S. Shah, V. Haughton, and A. Muñoz Del Río, “CSF flow through the upper cervical spinal canal in Chiari I malformation,” *American Journal of Neuroradiology*, vol. 32, no. 6, 2011, doi: 10.3174/ajnr.A2460.
- [42] E. C. Clarke, D. F. Fletcher, M. A. Stoodley, and L. E. Bilston, “Computational fluid dynamics modelling of cerebrospinal fluid pressure in Chiari malformation and syringomyelia,” *Journal of Biomechanics*, vol. 46, no. 11, 2013, doi: 10.1016/j.jbiomech.2013.05.013.
- [43] S. H. Pahlavian *et al.*, “The impact of spinal cord nerve roots and denticulate ligaments on cerebrospinal fluid dynamics in the cervical spine,” *PLoS ONE*, vol. 9, no. 4, 2014, doi: 10.1371/journal.pone.0091888.
- [44] K. H. Støverud, M. Alnæs, H. P. Langtangen, V. Haughton, and K.-A. Mardal, “Poroelastic modeling of Syringomyelia – a systematic study of the effects of pia mater, central canal, median fissure, white and gray matter on pressure wave propagation and fluid movement within the cervical spinal cord,” *Computer Methods in Biomechanics and Biomedical Engineering*, vol. 19, no. 6, Apr. 2016, doi: 10.1080/10255842.2015.1058927.
- [45] C. D. Bertram, “Evaluation by fluid/structure-interaction spinal-cord simulation of the effects of subarachnoid-space stenosis on an adjacent syrinx,” *Journal of Biomechanical Engineering*, vol. 132, no. 6, 2010, doi: 10.1115/1.4001165.
- [46] L. E. Bilston and L. E. Thibault, “The mechanical properties of the human cervical spinal cord In Vitro,” *Annals of Biomedical Engineering*, vol. 24, no. S1, Sep. 1995, doi: 10.1007/BF02770996.
- [47] T. K. Hung, H. S. Lin, L. Bunegin, and M. S. Albin, “Mechanical and neurological response of cat spinal cord under static loading,” *Surgical Neurology*, vol. 17, no. 3, 1982, doi: 10.1016/0090-3019(82)90284-1.
- [48] C. D. Bertram and M. Heil, “A Poroelastic Fluid/Structure-Interaction Model of Cerebrospinal Fluid Dynamics in the Cord with Syringomyelia and Adjacent Subarachnoid-Space Stenosis,” *Journal of Biomechanical Engineering*, vol. 139, no. 1, 2017, doi: 10.1115/1.4034657.

- [49] C. D. Bertram, A. R. Brodbelt, and M. A. Stoodley, "The origins of syringomyelia: Numerical models of fluid/structure interactions in the spinal cord," *Journal of Biomechanical Engineering*, vol. 127, no. 7, 2005, doi: 10.1115/1.2073607.
- [50] C. D. Bertram, "A numerical investigation of waves propagating in the spinal cord and subarachnoid space in the presence of a syrinx," *Journal of Fluids and Structures*, vol. 25, no. 7, 2009, doi: 10.1016/j.jfluidstructs.2009.06.008.
- [51] M. Heil and C. D. Bertram, "A poroelastic fluid-structure interaction model of syringomyelia," *J Fluid Mech*, vol. 809, pp. 360–389, 2016.
- [52] M. A. Biot, "General theory of three-dimensional consolidation," *Journal of Applied Physics*, vol. 12, no. 2, 1941, doi: 10.1063/1.1712886.
- [53] M. A. Biot, "Mechanics of Deformation and Acoustic Propagation in Porous Media," *Journal of Applied Physics*, vol. 33, no. 4, Apr. 1962, doi: 10.1063/1.1728759.
- [54] A. R. A. Khaled and K. Vafai, "The role of porous media in modeling flow and heat transfer in biological tissues," *International Journal of Heat and Mass Transfer*, vol. 46, no. 26, 2003. doi: 10.1016/S0017-9310(03)00301-6.
- [55] C. A. Silvera Delgado, "Modelling the lymphatic system: Computational model of lymphatic capillaries-interstitium interaction in normal physiological and pathological conditions.," Torino, 2017.
- [56] "Porous Media Flow Module User's Guide COMSOL 5.6," 2020. <https://doc.comsol.com/5.6/doc/com.comsol.help.porous/PorousMediaFlowModuleUsersGuide.pdf> (accessed Apr. 13, 2021).
- [57] Z. Shi and X. Wang, "Comparison of Darcy's Law, the Brinkman Equation, the Modified N-S Equation and the Pure Diffusion Equation in PEM Fuel Cell Modeling," *COMSOL Conference*, 2007.
- [58] Asawari Pratiksha Kumbhar, "A Computational Biomechanics study of the Spinal Cord in Patients with Chiari Malformation and Syringomyelia," Ghent, 2020.
- [59] C. Rossi *et al.*, "Water diffusion anisotropy in white and gray matter of the human spinal cord," *Journal of Magnetic Resonance Imaging*, vol. 27, no. 3, 2008, doi: 10.1002/jmri.21252.
- [60] W. T. Curry, Z. Ghogawala, S. Gollogly, and D. Brodke, "Postoperative Imaging," in *Spine Surgery*, Elsevier, 2005. doi: 10.1016/B978-0-443-06616-0.50137-1.